Graz University of Technology

Master Thesis

Real-time Multipath-assisted Indoor Tracking and Feature Detection

conducted at the
Signal Processing and Speech Communications Laboratory
Graz University of Technology, Austria

by
Lafer Manuel, BSc

Supervisors:
Dipl.-Ing. Paul Meissner
Dipl.-Ing. Erik Leitinger

Assessors/Examiners:
Assoc.Prof. Dipl.-Ing. Dr. Klaus Witrisal

Graz, February 20, 2014

Abstract

This thesis builds upon the work on Multipath-assisted Indoor Navigation and Tracking (MINT) where the position of a mobile agent is tracked with an extended Kalman filter (EKF) in an indoor environment using ultra-wideband (UWB) signals. It exploits not only the line-of-sight components but also the deterministic reflections of the signals. The floor plan and the anchor positions have to be known to calculate the virtual anchor (VA) positions which serve as additional anchors for the reflections.

In the first part of this thesis, a real-time demonstrator of the MINT system using a M-Sequence correlation channel sounder is presented and its performance is evaluated. In a further step, the variance of the distance measurements to the VAs is estimated online using the signal-to-noise-and-interference-ratio (SINR) to improve the accuracy and robustness of the system. The derivation of the SINR estimator is based on the Cramér-Rao lower bound (CRLB) and uses additional information provided by the variation of the amplitudes of the multipath components (MPCs) in the signals. It is shown that the online estimation of the VA variance improves the robustness of the system.

The second part of the thesis mainly deals with the discovery of VAs in a scenario where only a reduced set of VAs is known initially. This is an approach comparable to simultaneous localization and mapping (SLAM). The goal is to optimize the floor plan and to discover unknown VAs. Additionally, errors in the VA positions due to imprecise floor plans and positioning errors of the anchors can be accounted for by an improved version of the tracker (online re-localization) using the obtained measurements. The simulation results using synthetic signals show that bad tracking of the mobile agent and errors in the range measurements impair the estimation of unknown VAs. Analysis using measurement data shows that diffuse multipath has a lot of influence on the estimation of unknown VAs and leads to erroneously discovered VAs. Due to the online re-localization capability, erroneous discoveries can be corrected and the online variance estimation allows to reduce the influence of unreliable VAs. The results show that using the VA discovery and online variance estimation the tracking performance is improved.

Kurzfassung

Diese Thesis baut auf auf die Arbeit in Multipath-assisted Indoor Navigation and Tracking (MINT) auf. Dort wird die Position eines mobilen Benutzers mittels eines Extended Kalman Filters (EKF) in einem Innenraumszenario mit Hilfe von Messungen von Ultra-Breitband Signalen verfolgt. Es werden nicht nur die Messungen der direkten Sichtverbindung, sondern auch die deterministischen Reflexionen der Signale verwendet. Der Raumplan und die Position der Anker muss bekannt sein um die Positionen der virtuellen Anker (VAs), die als zusätzliche Anker für die Reflexionen dienen, zu berechnen.

Im ersten Teil der Arbeit wird eine Echtzeit- Implementierung des MINT Systems mit einem M-Sequenz Channel Sounder vorgestellt und die Performance evaluiert. In einem weiteren Schritt wird mittels signal-to-noise-and-interference-ratio (SINR) online die Varianz der Distanzmessungen zu den VAs geschätzt um die Genauigkeit und Robustheit des Systems zu erhöhen. Die Herleitung des SINR-Schätzers basiert auf der Cramér-Rao lower bound und verwendet zusätzliche Information aus den Amplituden der Mehrwegekomponenten in den Signalen. Es wird gezeigt, dass die Online-Schätzung der VA Varianz die Robustheit des Systems erhöht.

Der zweite Teil beschäftigt sich mit dem Finden von VAs in einem Szenario, in dem nur eine beschränkte Anzahl von VAs von Beginn an bekannt ist. Dieser Ansatz ist vergleichbar mit dem Simultaneous Localization and Mapping (SLAM) Ansatz. Das Ziel ist, den Raumplan zu optimieren und unbekannte VAs zu finden. Die Positionen der VAs können durch ungenaue Raumpläne oder ungenaue Positionierung der Anker fehlerhaft sein. Durch eine erweiterte Version des Trackers und Verwendung der Messungen können diese Fehler korrigiert werden (Online-Relokalisierung). Simulationsergebnisse mit synthetischen Signalen zeigen, dass eine schlechte Tracking Performance und fehlerhafte Distanzmessungen die Genauigkeit der gefundenen VA Positionen verringert. Analysen mit Messdaten zeigen, dass diffuse Mehrwegeausbreitung sehr viel Einfluss auf das Finden von VAs hat und zu fehlerhaften Ergebnissen führt. Durch die Online-Relokalisierung können die Fehler verringert werden und die Online-Varianzschätzung verringert den Einfluss von unzuverlässigen und fehlerhaften VAs. Die Ergebnisse zeigen, dass durch das Finden unbekannter VAs und die Online-Varianzschätzung die Tracking Performance verbessert wird.

Statutory Declaration

I declare that I have authored this thesis independently, that I have not used other than the declared sources/resources, and that I have explicitly marked all material which has been quoted either literally or by content from the used sources.

date	(signature)

Contents

1 Introduction

Indoor navigation and tracking has become more and more interesting in the recent years because of emerging technologies and applications, e.g. military, logistics and emergency scenarios. It is well known that GPS is not suitable for indoor positioning and navigation. There is a manifold of technologies which are used for indoor positioning [1] like Wifi, Bluetooth, RFID and some more. New systems try to use multiple sensors simultaneously to increase the accuracy and robustness. This is mostly done using smart phones (e.g. [2]) which come with a variety of sensors.

Ultra-wideband (UWB) is also one of the interesting technologies for indoor navigation and tracking [3] and UWB signals are well investigated [4–8]. In the recent years, UWB is especially of interest due to its fine spatial resolution. The usage of UWB for navigation and tracking purposes is investigated in areas such as logistics, military applications, tracking for manufacturing and more [9].

UWB signals are used in the MINT (multipath-assisted indoor navigation and tracking) problem [10], which tries to exploit multipath components (MPCs) for positioning and tracking. In [11], a concept for determining the position of mobile in an indoor environment and tracking it using a single physical anchor and a known floor plan was introduced. It exploits MPCs of measured UWB signals and maps them to so called virtual anchors (VAs). In a successive paper [12], an improved concept is presented. There, a vector network analyzer (VNA) is used for measuring the UWB signals.

A different problem is the simultaneous localization and mapping (SLAM) problem. SLAM investigates, if it is possible to send a mobile robot into an unknown environment and simultaneously build a map of the environment and determine the location of the robot in this environment. In [13], the first part of an introductory paper on SLAM, the basic problem of SLAM is described and how it can be solved using an extended Kalman filter (EKF) or Rao-Blackwellized filter (particle filter, FastSLAM). The second part of the SLAM paper [14] describes, how computational complexity, data association (associate measurements to already observed features and add newly observed features to the map) and environment description can be improved.

Investigations on the SLAM problem have been made with different signals, e.g. laser [15], radar [16] or video [17]. A SLAM approach using UWB is presented in [18, 19]. It uses a bat-type sensor array (one transmitter, one receiver on the left and on the right of it) measuring UWB impulse responses. The algorithm combines data association, particle filter and EKF. All proposed SLAM approaches measure at least range and bearing. There exists a sub- group of SLAM called range-only SLAM where only range measurements are used. A general framework

for the range-only SLAM is presented in [20]. It deals with the problem that multiple range measurements are needed for the initialization of a new feature. In a consecutive paper [21] the problem of joining locally estimated maps to obtain a complete map of the discovered environment is presented. In [22], a system for navigation of an underwater vehicle using a transceiver for measuring acoustic time of flights is presented. UWB transceivers are used in [23]. There a probabilistic approach using Rao-Blackwellized Particle Filters is chosen.

This thesis is divided into two parts. In the first part, a real-time implementation of the previously described MINT problem [12] using a correlative channel sounder is presented and the tracking performance is evaluated. In the second part, a combination of the MINT and SLAM approach is investigated. The task is to start with a reduced set of known VAs and to discover unknown VAs while moving in a room. Furthermore, the positions of the known VAs are assumed not to be perfect and static as in the original MINT problem but they are erroneous due to imprecise room geometry or anchor positioning. The tracker can correct the VA positions using the measurements associated to the respective VA. The question is how well the positions of the unknown VAs can be estimated using range-only measurements, how do poorly estimated VAs influence the tracking and is it possible to correct a bad VA estimation.

In Chapter 2 of this thesis UWB and the channel model used in this work are introduced. The concept of virtual anchors, tracking and results of the tracking are presented in Chapter 3. Furthermore, the estimation of the variance of VAs based on the CRLB [10] is introduced and results of an online estimation are compared to offline results. The main part of this work is Chapter 4 where first a re-localization procedure to correct erroneous VA positions using the measured signals is presented. Then the extension of the re-localization leads to the combination of MINT and SLAM. Results from simulations using synthetic signals and measured signals are analyzed. A Conclusion and some topics for future work are presented in Chapter 5.

2 Ultra-Wideband and Signal Model

In this chapter, basics on Ultra- Wideband (UWB) and the used signal model are presented.

2.1 Ultra-Wideband

Ultra-Wideband (UWB) signals are defined to have either an absolute bandwidth of $> 500\,\mathrm{MHz}$ or a relative bandwidth $> 20\,\%$. An UWB signal can also meet both criteria at the same time. The large bandwidth is necessary for the increasing demand of high data rate applications, e.g. video streaming, but it also comes with other advantages like no significant multi-path fading.

The property of UWB which is exploited most in this work is the high temporal resolution which allows very accurate ranging and consequently positioning. The high temporal resolution stems from the large bandwidth, as they are inversely proportional:

$$\Delta t = \frac{1}{B}. \tag{2.1}$$

As with any radio communication system the used frequency range is controlled by some frequency regulator. In the US, the FCC allows the unlicensed use of UWB under some conditions. For the unlicensed usage of UWB for indoor applications, a power spectral density of $-41.3\,\mathrm{dBm/MHz}$ is allowed in the frequency band between 3.1 and 10.6 GHz (see Fig. 2.1) which will be used in this work.

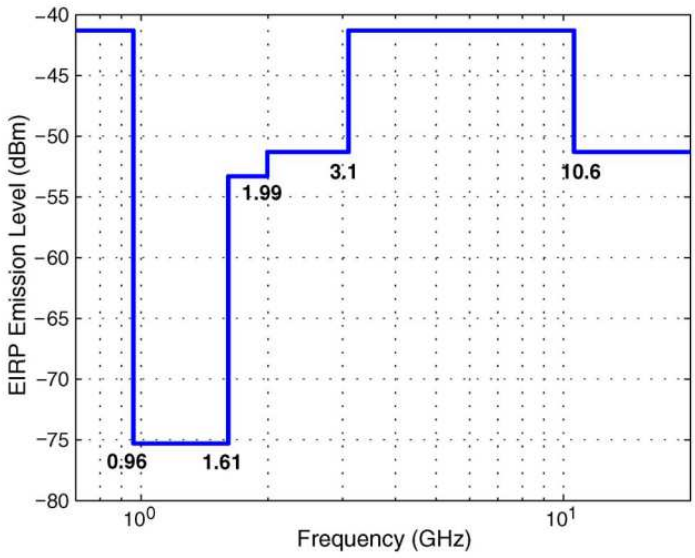

Figure 2.1: UWB frequency regulation mask by FCC [24]

2.1.1 Multipath Channel Model

The fact that a signal can get from TX to RX via different paths is very fundamental to UWB. To easily understand this phenomenon, the electro-magnetic field emitted by the antenna can be thought of as a sum of different components, which are sent in every direction. Each component interacts with the environment, e.g. it is reflected, penetrates some material, is scattered or diffracted. Some interactions can change the direction of the component (e.g. by reflection) and some can split up the component into new components (e.g. by diffraction). As each component travels on a different path until it arrives at the receiver, the path length and therefore the delay is different for most components. There can be multiple components with the same path length in symmetric situations. Each component that arrives at the RX on a different path is called a multipath component (MPC).

Each MPC has a certain path length d_k and therefore a certain delay τ_k, a certain attenuation and direction of arrival. The delay τ_k can be computed using the path length

$$\tau_k = \frac{1}{c} \cdot d_k \tag{2.2}$$

where c is the speed of light. The path length can be expressed as the distance between TX and RX

$$d_k = ||\boldsymbol{p}_{\mathrm{TX}} - \boldsymbol{p}_{\mathrm{RX}}|| \tag{2.3}$$

where $\boldsymbol{p}_{\mathrm{TX}}$ and $\boldsymbol{p}_{\mathrm{RX}}$ are vectors holding the two-dimensional coordinates of TX and RX, respectively.

The signal arriving at the RX is the sum of all MPCs, where each component is a scaled and delayed copy of the transmit signal. The channel impulse response $h(\tau)$ when taking only those

components into account can be modeled using [25]

$$h(\tau) = \sum_{n=1}^{N} \alpha_n \delta(\tau - \tau_n) * \chi_n(\tau) \tag{2.4}$$

where α_n is the complex amplitude and τ_n the delay of the n-th MPC, N being the total number of MPCs including the line-of-sight (LOS) component and $\chi_n(\tau)$ models the distortion of the MPCs due to frequency selectivity. The channel parameters are mostly modeled statically. The system which operates in the channel also has to be taken into account. Every system has a finite bandwidth B. The impulse response is therefore convolved with the system response. A simple model of that would be to think of the time delay axis divided into equally spaced bins with bin width $1/B$. Those bins are called resolvable delay bins. All contributions falling into a bin are added up because they cannot be resolved. The MPCs in one bin can be added up in a constructive or a destructive way, depending on the phase of the components.

2.1.2 Deterministic/Stochastic Channel and Signal Model

The UWB channel impulse response (CIR) introduced in [10] is defined as

$$h(\tau) = \sum_{k=1}^{K} \alpha_k \delta(\tau - \tau_k) + \nu(\tau). \tag{2.5}$$

It consists of K deterministic signal components, each with a complex coefficient α_k and a delay τ_k. Each component stems from well-defined reflections. The signal $\nu(\tau)$ is a stochastic process which models diffuse multipath. This includes scattering at rough surfaces and other propagation influences which can not be captured by any deterministic model. The received signal $r(t)$ at the mobile agent position is described by

$$r(t) = \sum_{k=1}^{K} \alpha_k s(t - \tau_k) + \int_{-\infty}^{+\infty} s(\lambda)\nu(t - \lambda)d\lambda + w(t) \tag{2.6}$$

where $s(t) \in \mathbb{C}$ denotes a UWB base-band pulse and $w(t)$ models Additive White Gaussian Noise (AWGN) with a two-sided power spectral density of $\frac{N_0}{2}$. The distortion of MPCs is neglected in this model.

3 Positioning and Tracking

In this chapter, the concept of virtual anchors (VAs) is introduced. After that the basic tracking procedure is described. It involves tracking the mobile agents position and velocity using the precomputed VA data structure as described in [26]. The goal of this part of the thesis is to determine whether it is possible to implement such a system in real-time using a channel sounder and if so, to evaluate the performance and robustness of the system.

Similar work using UWB signals has been done in [27]. There a simulator has been proposed and a performance comparison between Least Squares, Standard Kalman Filter and Extended Kalman Filter for tracking is presented.

3.1 Floor Plan and Virtual Anchors (VAs)

To determine the position of a mobile agent in a two-dimensional environment, at least three anchors are necessary. For each anchor, the position has to be known. In this work, time-of-arrival range measurements are used, i.e. agent and anchors have to be synchronized. Using range measurements from the agent to each anchor, the agent position can be computed using the circle equation with the anchor positions as the circle center and the range measurement as the circle radius. This principle is called trilateration and is illustrated in Fig. 3.1(a). The figure shows the ideal case where there is exactly one intersection which is the agent position. In real scenarios, measurements are noisy and anchor positions are not known perfectly. There will be three intersections around the agent position. In order to find the best estimate for the intersection, e.g. Least Squares algorithm can be used. This case can be seen in Fig. 3.1(b). The positioning process described here uses only the direct signal paths, i.e. the LOS components. A huge drawback of this method is that for determining the position of an agent in a room, at every point in the the room, at least three anchors have to be visible and in transmission range. That means, for complicated room geometry or large rooms, several anchors are needed and have to be placed to fulfill those requirements.

The concept of VAs is introduced to overcome those drawbacks. The agent transmits a UWB signal which is received by the anchors. This corresponds to the previously described scenario where only the LOS components are used. However, the signal is reflected at the walls and other structure in the environment. The reflected signals arrive delayed at the receiver and can be identified as multipath components (MPCs) in the measured signal. Each of those components has a certain delay corresponding to the signal path length. To each reflection, a virtual anchor

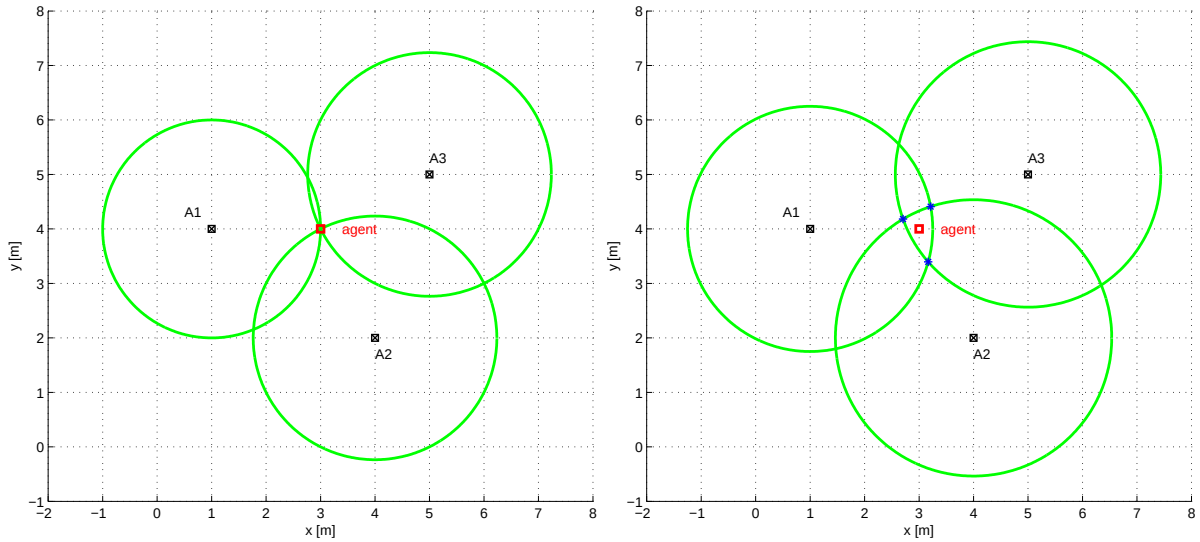

(a) Trilateration principle (ideal case)

(b) Trilateration principle (imperfect case)

Figure 3.1: Trilateration principle

(VA) can be associated. The position of a VA corresponds to the anchor position mirrored with respect to the reflecting surface. Fig. 3.2 shows the described concept. The red solid line indicates the direct signal path from the transmitter to the anchor (A2). The cyan solid line denotes the path of the signal which is reflected at a wall and arrives at the anchor later as it has a longer signal path (a higher delay) as the direct path. The cyan dashed line describes the virtual path to the VA with the same length as the path of the signal from the anchor to the wall. The virtual path length plus the length of the path from the wall to the agent is the same as the total path length of the corresponding deterministic MPC. So, this MPC can be seen as originated from this VA (here VA 1182) which means that the VA's coordinates are the mirrored coordinates of the anchor with respect to the reflective wall. As a consequence, the VA coordinates can be computed using the anchor coordinates and the geometry of the underlying room. The CIR for this situation is shown in Fig. 3.3. The peaks in the measured and pulse shaped signal match the two expected delays.

There exist different types of VAs, depending on how many reflections are involved. In Fig. 3.2 a first order VA is shown because one signal reflection happens. A VA of second order would involve two reflections. To compute VAs which correspond to higher order reflections, VAs with lower order have to be mirrored on corresponding wall segments. The number of order which can be used depends on how large the room is (the larger the room the fewer reflections can be used due to path loss) and how strong the building structure attenuates the signal (strong attenuation means that higher order reflections are unlikely).

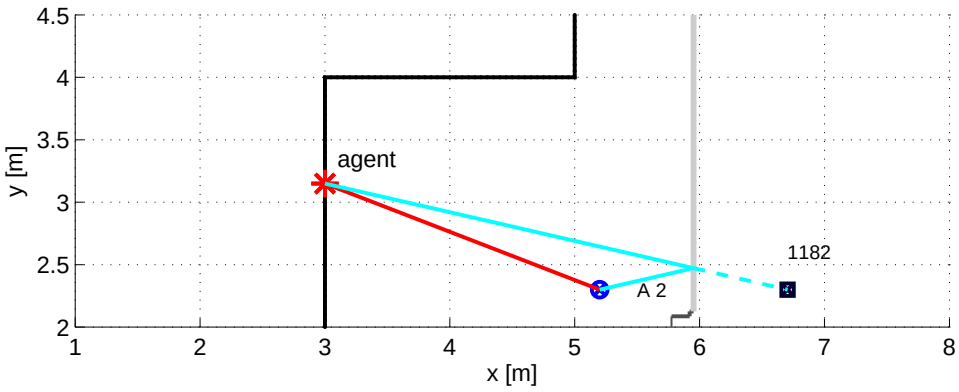

Figure 3.2: Floor plan showing VA concept

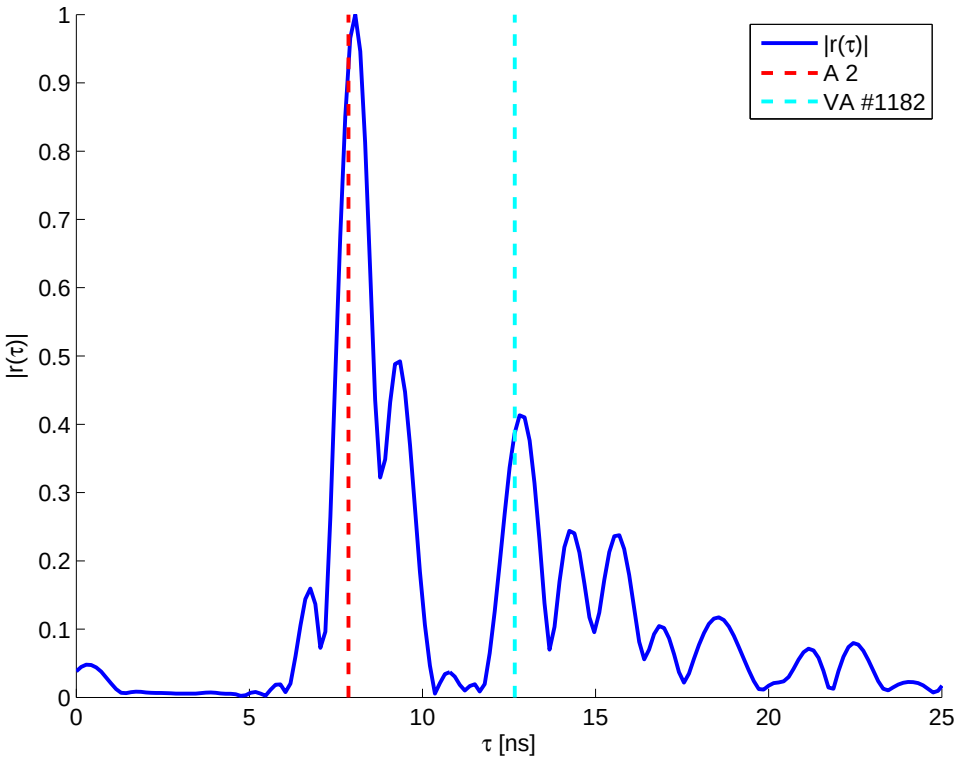

Figure 3.3: CIR and expected delays for situation as shown in Fig. 3.2. Pulse shaping parameters are $f_c = 7\ GHz$, $\beta_R = 0.5$ and $T_p = 1\ ns$

3.2 The Tracking Procedure

The block diagram of the tracking procedure is shown in Fig. 3.4. The goal of tracking is to estimate the mobile agents position $\boldsymbol{p}_\ell$ at every discrete time instance from the previous position $\boldsymbol{p}_{\ell-1}$ using a motion model and the actual measurement set $\mathcal{Z}_\ell$. The index ℓ denotes the position index, no superscript indicates that the value is the *a posteriori* while a $-$ would denote an *a priori* value.

From the signal $r_\ell(\tau)$ measured at $\boldsymbol{p}_\ell$ the MPCs are extracted, the estimated delay expressed as distance of each MPC is used for data association (estimated distances $\mathcal{Z}_\ell$). To convert a delay to a distance $d = \tau \cdot c$ is used, where c is the speed of light. Using the agents position $\boldsymbol{p}_{\ell-1}$ from the previous time step and the motion model, the agents next position $\boldsymbol{p}_\ell^-$ is predicted.

For each VA $\boldsymbol{a}_i$ the visibility at the predicted position $\boldsymbol{p}_\ell^-$ is computed, i.e. $\mathrm{f_{vis}}(\boldsymbol{a}_i, \boldsymbol{p}_\ell^-) = 1$ if the VA is visible for the current position estimate and $\mathrm{f_{vis}}(\boldsymbol{a}_i, \boldsymbol{p}_\ell^-) = 0$ if it is not visible. As it would be too computationally expensive to compute the visibilities online during the execution of the tracking system, a visibility matrix is computed in an offline phase before the tracking. This matrix can be used as lookup-table to determine the visible VAs for the current position. This results in two sets $\mathcal{A}_\ell$ and $\mathcal{D}_\ell$ holding the expected VA positions and distances, respectively.

The task of the data association is to find the best fit of the measured distances to the expected distances, i.e. to find out which measurement corresponds most likely to which VA. The result of this block, the set $\mathcal{C}_\ell$, is used together with $\mathcal{Z}_\ell$ and $\boldsymbol{p}_\ell^-$ in the tracking algorithm to determine the next position of the mobile $\boldsymbol{p}_\ell$. $\mathcal{C}_\ell$ holds correspondence variables indicating which measurement is associated to which VA.

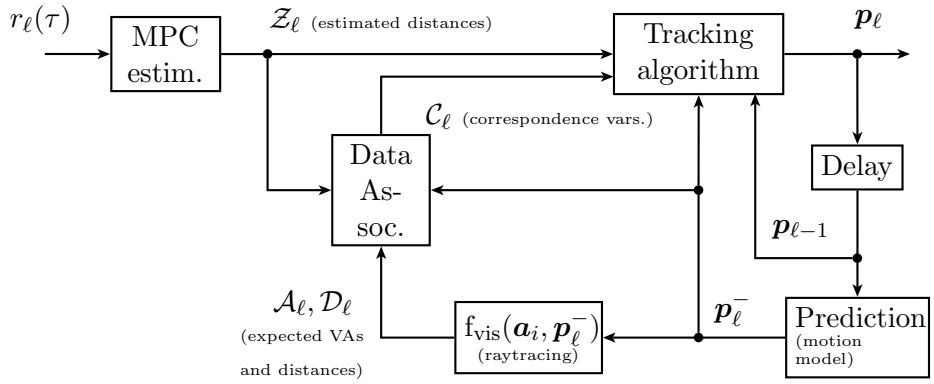

Figure 3.4: Tracking and data association (DA) scheme [12]

3.3 Multipath Component Estimation

For the tracking algorithm and for the data association it is necessary to estimate the delays of the MPCs of the measured signal $r_\ell(\tau)$. This is done using a cancellation algorithm [28]. The estimation of the delays $\hat{\tau}_k$ and complex amplitudes $\hat{\alpha}_k$ of the k-th MPC from the measured signal is done iteratively. The algorithm is working not on the measured signal itself but on an intermediate signal $r_{\ell,k}(\tau)$ from which the estimated MPCs are subtracted one by one. The initial intermediate CIR is the measured CIR itself, i.e. $r_{\ell,0}(\tau) = r_\ell(\tau)$.

The algorithm searches for the maximum in the signal and takes the delay $\hat{\tau}_k$ at which the maximum is located as the estimated delay. The complex amplitude $\hat{\alpha}_k$ of the MPC is estimated by a projection of the intermediate signal onto a template pulse $s(t)$ shifted to the estimated delay $\hat{\tau}_k$

$$\hat{\alpha}_k = \int_0^T r_{\ell,k-1}(t) s^*(t - \hat{\tau}_k) dt \tag{3.1}$$

where T is the maximum delay of $r_{\ell,k}(\tau)$. The template pulse is generated using the pulse shaping parameters of the measured signal. The template pulse scaled by the estimated amplitude $\hat{\alpha}_k$ is shifted to the estimated delay $\hat{\tau}_k$ and subtracted from the previous intermediate signal $r_{\ell,k-1}(\tau)$

resulting in an intermediate CIR $r_{\ell,k}(\tau)$

$$r_{\ell,k}(\tau) = r_{\ell,k-1}(\tau) - \hat{\alpha}_k s(\tau - \hat{\tau}_k) \tag{3.2}$$

The delay estimation and cancellation step is repeated until a predefined number K of MPCs is found or the amplitude of the extracted maximum is below some threshold. The threshold depends on the maximum of the measured signal. Using all the extracted MPCs the signal can be reconstructed

$$r_{\ell,\text{reconst}}(\tau) = \sum_{k=1}^{K} \hat{\alpha}_k s(\tau - \hat{\tau}_k). \tag{3.3}$$

The diffuse multipath plus noise signal $n_\ell(\tau)$ is defined as

$$n_\ell(\tau) = s(\tau) * \nu_\ell(\tau) + w_\ell(\tau) \tag{3.4}$$

and an estimation of it can be obtained by

$$n_\ell(\tau) = r_\ell(\tau) - r_{\ell,\text{reconst}}(\tau). \tag{3.5}$$

Fig. 3.5 shows all the signals. The set of all estimated distances $\mathcal{Z}_\ell = \{z_1, ..., z_K\}$ where $z_k = \hat{\tau}_k c$ is used in the data association and the tracking algorithm (see Fig. 3.4). Typically, $\mathcal{Z}_\ell$ does not only hold distances of deterministic MPCs but also distances due to noise or diffuse multipath.

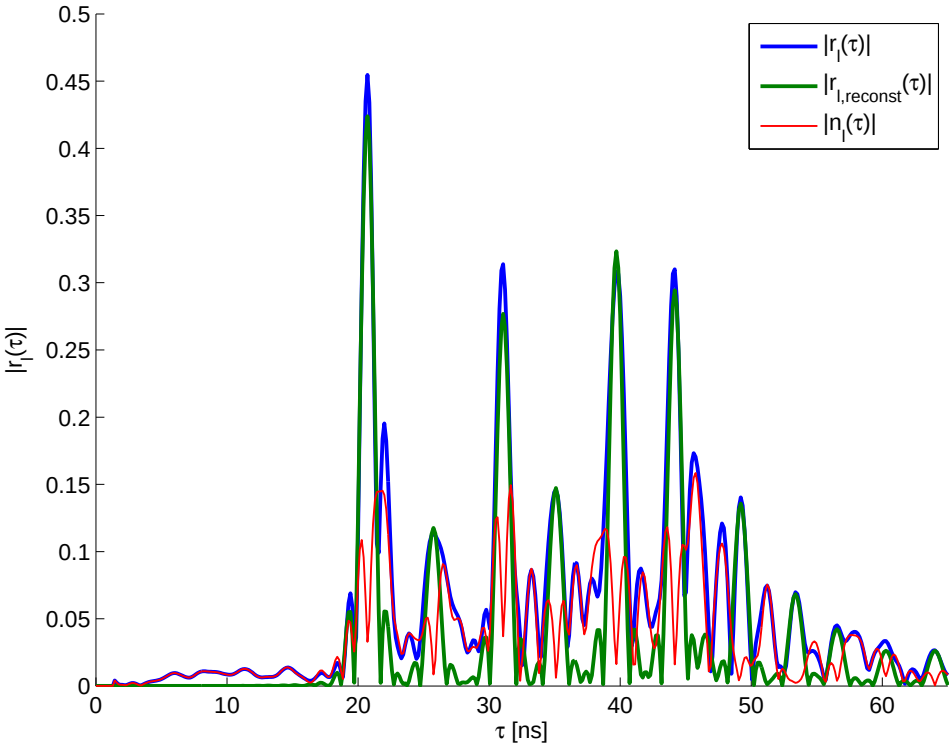

Figure 3.5: Measured signal $r_\ell(\tau)$, reconstructed signal $r_{\ell,\text{reconst}}(\tau)$ and remaining noise plus diffuse multipath signal $n_\ell(\tau)$. Pulse shaping parameters: $f_c = 7\,GHz$, $\beta_R = 0.5$ and $T_p = 1\,ns$

3.4 Data Association

The purpose of the data association is to find out which estimated distance is most likely caused by which VA in the measured signal. The first step is to find out which VAs are visible at the current agent position by using a precomputed lookup-table as described Section 3.2. The expected distance between the *a priori* agent position $\boldsymbol{p}_\ell^-$ and the VA position $\boldsymbol{p}_k \in \mathcal{A}_\ell = \left\{a_j : f_{\text{vis}}(a_j, \boldsymbol{p}_\ell^-) = 1\right\}$ for $j = 1, \ldots, N_{\text{VA}}$ is given by

$$d_k = ||\boldsymbol{p}_\ell^- - \boldsymbol{p}_k||. \tag{3.6}$$

The set of all expected distances is $\mathcal{D}_\ell$. From the MPC estimation a set $\mathcal{Z}_\ell$ containing all estimated distances is obtained. The task of the data association is to find a sub-pattern of $\mathcal{Z}_\ell$ that matches $\mathcal{D}_\ell$ best [26]. For this, a set of correspondence variables $\mathcal{C}_\ell$ is introduced. Its n-th entry c_n holds an association of the n-th entry of $\mathcal{Z}_\ell$ and is

$$c_n = \begin{cases} j, & \text{if } z_n \text{ corresponds to VA } a_j \\ 0, & \text{if } z_n \text{ corresponds to clutter.} \end{cases} \tag{3.7}$$

The cardinality of $\mathcal{D}_\ell$ is K and the cardinality of $\mathcal{Z}_\ell$ is $\hat{K}$. To assure that $\hat{K} \geq K$ as the algorithm requires, $\mathcal{Z}_\ell$ can be filled with clutter data to satisfy the requirement. A distance function $d^{(d_c)}(\cdot,\cdot)$ with the parameter d_c (cut-off distance) which sets the distance d_k between mobile and the k-th VA to d_c if $d_k > d_c$, is used. The goal of the algorithm is to find the vector $\boldsymbol{\pi}_{\text{opt}}$ which holds the permutation of $\mathcal{Z}_\ell$ with the minimum cumulative distance, where the distance is computed using $d^{(d_c)}(\cdot,\cdot)$. It is found by

$$\boldsymbol{\pi}_{\text{opt}} = \arg \min_{\boldsymbol{\pi} \in \Pi_{\hat{K}}} \sum_{i=1}^{K} d^{(d_c)}(d_i, z_{\pi_i}) \tag{3.8}$$

where $\Pi_{\hat{K}}$ is the set of all permutations of positive integers up to $\hat{K}$. The result $\boldsymbol{\pi}_{\text{opt}}$ contains the indices of those measurements in $\mathcal{Z}_\ell$ which have been optimally assigned to $\mathcal{D}_\ell$. All measurements for which $d^{(d_c)}(\cdot,\cdot) = d_c$ are rejected as they have been assigned at a distance greater or equal to the cut-off distance. Finally, the correspondence variables are

$$c_n = \begin{cases} j, & \text{if } \pi_j = n \text{ and } d^{(d_c)}(d_j, z_{\pi_{\text{opt},n}}) < d_c \\ 0, & \text{else} \end{cases} . \tag{3.9}$$

Fig. 3.6 shows a reconstructed received signal $r_{\text{reconst}}(\tau)$, the estimated distances z_k and the expected distances d_k. In Fig. 3.7 the data association result is shown graphically. The blue circles indicate expected distances, the black circles are estimated distances. The set of associated pairs of delays (circles connected by dashed lines) represents the optimal sub-set of VAs which corresponds to the measurement.

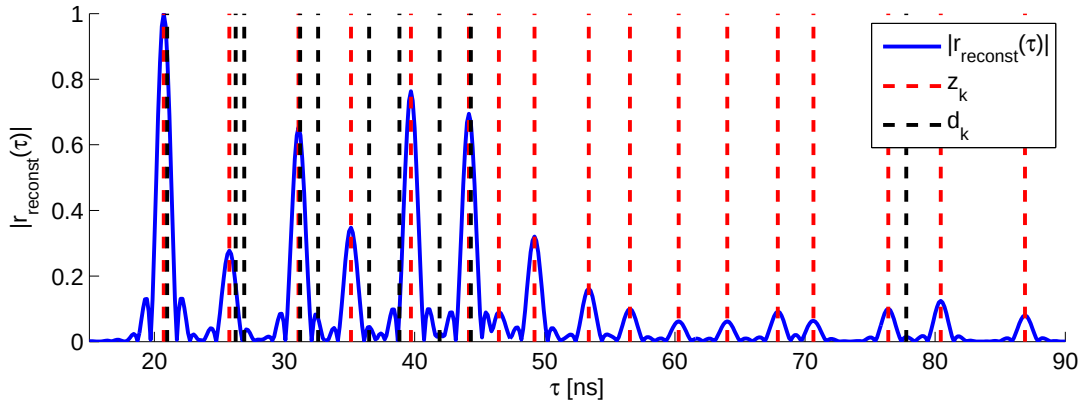

Figure 3.6: Reconstructed signal $r_{\text{reconst}}(\tau)$, estimated delays z_k and expected delays d_k. Pulse shaping parameters: $f_c = 7\ GHz$, $\beta_R = 0.5$ and $T_p = 1\ ns$

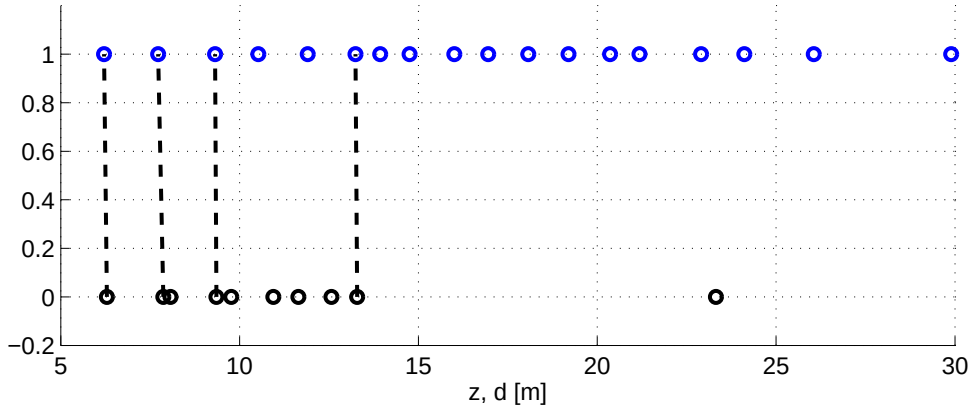

Figure 3.7: Data association principle, the measured distances are plotted on the lower part in black circles, expected distances are the blue circles above. A line connecting two points indicate that a association has been found. Data association parameter cut-off distance $d_c = 0.2\,m$. The correspondence numbers are not plotted.

3.5 Extended Kalman Filter

As tracking algorithm an Extended Kalman Filter (EKF) is used. It is a nonlinear version of the Kalman Filter and is used to track the position and the velocity of a mobile agent. Position and velocity together are called the state of the EKF (see state vector $\boldsymbol{x}$ in Section 3.5.1). The EKF can be seen as a sequential estimator of a signal embedded in noise. Fig. 3.8 shows the basic EKF model which works in two steps. The prediction step uses a motion model to predict the next state and the measurement update step corrects wrong predictions. The data association is done after the prediction step at the prior position $\boldsymbol{p}_\ell^-$ to associate the measurements to the corresponding VAs.

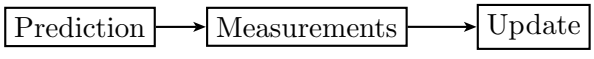

Figure 3.8: EKF sequence

3.5.1 State Vector and Error Covariance

A remark on the notation: The subscript n indicates the discrete time step, i.e. $\boldsymbol{x}_n$ is the current state vector at time step n and $\boldsymbol{x}_{n-1}$ is the state vector of the previous time step $n-1$. Variables with a superscript minus indicate *a priori* values, i.e. predicted values, after the prediction step but before the update step, e.g. $\boldsymbol{x}_n^-$ is the predicted state vector of the current time step. Variables with no superscript are *a posteriori* values, which are variables after the update step, i.e. $\boldsymbol{x}_n$ is the state vector after the update step. The state vector $\boldsymbol{x}_n$ consists of the mobiles position and velocity

$$\boldsymbol{x}_n = \begin{bmatrix} x_{m,n} & y_{m,n} & v_{x,n} & v_{y,n} \end{bmatrix}^T. \tag{3.10}$$

The error covariance matrix $\boldsymbol{P}_n$ contains the covariance of the mobile agents position and velocity and is defined as

$$\boldsymbol{P}_n = \mathrm{E}\big\{(\boldsymbol{x}_n - \hat{\boldsymbol{x}}_n)(\boldsymbol{x}_n - \hat{\boldsymbol{x}}_n)^T\big\} \tag{3.11}$$

where $\boldsymbol{x}_n$ is the true value of the state vector and $\hat{\boldsymbol{x}}_n$ is the estimate.

3.5.2 Motion Model and the Prediction Step

The motion model is the function which predicts the next state using the current state and the control input, given by

$$\boldsymbol{x}_n^- = f(\boldsymbol{x}_{n-1}, \boldsymbol{u}_n) + \boldsymbol{w}_n \tag{3.12}$$

where $\boldsymbol{x}_{n-1}$ is the predicted state vector of the last iteration, $\boldsymbol{u}_n$ is the control input and $\boldsymbol{w}_n$ is the process noise which is a zero mean multivariate Gaussian noise with covariance $\boldsymbol{Q}_n$. A constant velocity motion model is assumed, where the next position of the mobile agent is determined by the last position plus the velocity times the time-step dt between two iterations.

$$\begin{bmatrix} x_{m,n} \\ y_{m,n} \\ v_{x,n} \\ v_{y,n} \end{bmatrix} = \begin{bmatrix} x_{m,n-1} & + & dt \cdot v_{x,n-1} \\ y_{m,n-1} & + & dt \cdot v_{y,n-1} \\ v_{x,n-1} & + & u_{x,n-1} \\ v_{y,n-1} & + & u_{y,n-1} \end{bmatrix}. \tag{3.13}$$

The state transition matrix $\boldsymbol{F}$ is the derivative of $f(\cdot)$ w.r.t. the state vector $\boldsymbol{x}$, evaluated at the state vector and the control input. The *a priori* state vector is written as

$$\boldsymbol{x}_n^- = \boldsymbol{F}\boldsymbol{x}_{n-1} \tag{3.14}$$

and the *a priori* error covariance matrix as

$$\boldsymbol{P}_n^- = \boldsymbol{F}\boldsymbol{P}_{n-1}\boldsymbol{F}^T + \boldsymbol{Q}_n. \tag{3.15}$$

Here, the state transition matrix $\boldsymbol{F}$ is a constant matrix

$$\boldsymbol{F} = \begin{bmatrix} 1 & 0 & dt & 0 \\ 0 & 1 & 0 & dt \\ 0 & 0 & 1 & 0 \\ 0 & 0 & 0 & 1 \end{bmatrix}. \tag{3.16}$$

3.5.3 Observation Model and the Update Step

The observation model function uses the predicted state $\boldsymbol{x}_n^-$ to compute the expected measurement result $\boldsymbol{d}_n$ given by

$$\boldsymbol{d}_n = h(\boldsymbol{x}_n) + \boldsymbol{v}_n \tag{3.17}$$

where $\boldsymbol{v}_n$ is the observation noise which is zero mean multivariate Gaussian with covariance $\boldsymbol{R}_n$. For each measurement which has been associated with a VA, an expected measurement is computed. For the i-th measurement, (3.17) is the circle equation

$$d_{n,i} = \sqrt{(x_{m,n}^- - x_{\mathrm{VA}_i})^2 + (y_{m,n}^- - y_{\mathrm{VA}_i})^2} \tag{3.18}$$

using the predicted agent position and the coordinates of the according VA. For each measurement, the agent position is a point on a circle with the VA as the center. The observation matrix $\boldsymbol{H}$ is the derivative of the observation function $h(\cdot)$ w.r.t. the state vector $\boldsymbol{x}$, evaluated at the predicted state vector

$$\boldsymbol{H}_n = \begin{bmatrix} \frac{x_{m,n}^- - x_{\mathrm{VA}_1}}{\sqrt{(x_{m,n}^- - x_{\mathrm{VA}_1})^2 + (y_{m,n}^- - y_{\mathrm{VA}_1})^2}} & \frac{y_{m,n}^- - y_{\mathrm{VA}_1}}{\sqrt{(x_{m,n}^- - x_{\mathrm{VA}_1})^2 + (y_{m,n}^- - y_{\mathrm{VA}_1})^2}} & 0 & 0 \\ \vdots & & & \vdots \\ \frac{x_{m,n}^- - x_{\mathrm{VA}_N}}{\sqrt{(x_{m,n}^- - x_{\mathrm{VA}_N})^2 + (y_{m,n}^- - y_{\mathrm{VA}_N})^2}} & \frac{y_{m,n}^- - y_{\mathrm{VA}_N}}{\sqrt{(x_{m,n}^- - x_{\mathrm{VA}_N})^2 + (y_{m,n}^- - y_{\mathrm{VA}_N})^2}} & 0 & 0 \end{bmatrix} \tag{3.19}$$

where the number of rows of $\boldsymbol{H}_n$ is the number of measurements N which have been associated with VAs.

The innovation or measurement residual $\boldsymbol{y}_n$ is computed using

$$\boldsymbol{y}_n = \boldsymbol{z}_n - h(\boldsymbol{x}_n^-) \tag{3.20}$$

where $\boldsymbol{z}_n$ are the measured distances and $h(\boldsymbol{x}_n^-)$ are the expected distances. The innovation describes the deviation of the measured distances from the expected distances and it is used to correct wrong predictions. The innovation (or residual) covariance is computed using

$$\boldsymbol{S}_n = \boldsymbol{H}_n \boldsymbol{P}_n^- \boldsymbol{H}_n^T + \boldsymbol{R}_n \tag{3.21}$$

where $\boldsymbol{R}_n$ is the covariance of the observation noise. The updated state estimate $\boldsymbol{x}_n$ is computed using

$$\boldsymbol{x}_n = \boldsymbol{x}_n^- + \boldsymbol{K}_n \boldsymbol{y}_n \tag{3.22}$$

where $\boldsymbol{K}_n$ is the Kalman gain

$$\boldsymbol{K}_n = \boldsymbol{P}_n^- \boldsymbol{H}_n^T \boldsymbol{S}_n^{-1}. \tag{3.23}$$

The updated covariance estimate is computed using

$$\boldsymbol{P}_n = (\boldsymbol{I} - \boldsymbol{K}_n \boldsymbol{H}_n)\boldsymbol{P}_n^-. \tag{3.24}$$

3.6 VA Variance Estimation

To increase the robustness and accuracy of the system, more information can be extracted from the measured signals.

In [29], the idea is to do channel characterization measurements on a few known trajectory points in the room before the actual tracking to determine the reliability of the information of each VA. As reliability metric, the SINR (signal-to-inference-plus-noise ratio) is chosen. The SINR for the k-th VA at the ℓ-th position results from the CRLB [10] and is defined as

$$\mathrm{SINR}_{k,\ell} = \frac{|\alpha_{k,\ell}|^2}{N_0 + T_s S_\nu(\tau_{k,\ell})} \tag{3.25}$$

where $\alpha_{k,\ell}$ is the complex amplitude and $\tau_{k,\ell}$ the delay of the k-th MPC at the ℓ-th position, $\frac{N_0}{2}$ is the two-sided power spectral density of the AWGN, T_s is the effective pulse duration and $S_\nu(\tau)$ is the power delay profile of the diffuse multipath. (3.25) is only valid if no path overlap between signals from different VAs occurs. In order to estimate $S_\nu(\tau)$ reliably, the measurement points (the agent positions) have to be close to each other. This is not guaranteed in a tracking scenario. Therefore, only the average SINR can be computed by

$$\mathrm{SINR}_k \approx \frac{1}{\frac{m_{1,Y}}{\sqrt{m_{1,Y}^2 - m_{2,Y}}} - 1} \tag{3.26}$$

where $m_{1,Y}$ and $m_{2,Y}$ are the estimates of the first and second moment of the random variable Y which is

$$Y = |\hat{\alpha}_{k,\ell}|^2. \tag{3.27}$$

The variance of the position of the k-th VA $\mathrm{var}\{d_k\}$ is estimated using

$$\mathrm{var}\{d_k\} = \frac{c^2}{8\pi^2\beta^2}\mathrm{SINR}_k^{-1} \tag{3.28}$$

where c is the speed of light and β is the effective bandwidth of the the transmit pulse [30]

$$\beta = \sqrt{\frac{\int_{-\infty}^{+\infty} f^2 |S(f)|^2 df}{\int_{-\infty}^{+\infty} |S(f)|^2 df}}. \tag{3.29}$$

where $S(f)$ is the frequency domain representation of the transmit pulse and f is the according frequency vector. (3.28) is the CRLB for $\text{var}\{d_k\}$ and equality holds only for efficient estimators of d_k. The variances for each VA are used in the update step in the measurement noise covariance matrix $\boldsymbol{R}$ instead of the constant variances which assume that each VA has the same contribution to the tracking.

A real-time demonstrator implementation using the described estimation is presented in [31]. There, the SINRs were estimated using (3.26) beforehand in an offline phase.

The approach taken here attempts to estimate the SINRs online while the mobile agent is moving and use the estimated variances of the VAs to increase the accuracy and robustness of the tracking. Of course only measurements which have been associated to VAs can be used to extract amplitude information and therefore estimate the variance. Furthermore, measurements where path overlap is present cannot be used and have to discarded. To estimate the average SINRs online, (3.26) is used and the amplitudes of the MPCs are estimated over a short part of the trajectory over which the mobile agent moved. The set of used trajectory points consists of the agent positions from the current time step $\boldsymbol{p}_n$ to the position $\boldsymbol{p}_{n-N}$ at time step $n-N$ where

$$d_{\min} \leq ||(\boldsymbol{p}_{n-N} - \boldsymbol{p}_n)|| \leq d_{\max} \tag{3.30}$$

and $||(\boldsymbol{p}_{n-N} - \boldsymbol{p}_n)||$ is the distance between the first and the last point. The distance between $\boldsymbol{p}_n$ and $\boldsymbol{p}_{n-N}$ should not go below $d_{\min}$ in order to avoid correlated measurements and not exceed $d_{\max}$ to maintain spatial stationarity of the channel. For the estimation a certain number $N_{\min}$ of complex amplitudes has to be available for the determined part of the trajectory between $\boldsymbol{p}_{n-N}$ and $\boldsymbol{p}_n$, otherwise no estimation is done.

The initial variance of the VAs σ^2_{VA} has some default value. After some time steps (at least $N_{\min}$) for some VAs the SINRs can be estimated and using (3.28) the variance of the VA can be computed. In case the estimated SINR becomes 0 (leading to infinite variance) or is complex, the variance is set to some predefined value $\sigma^2_{\text{VA,max}}$ which has to be higher than the default variance to indicate that the VA is not reliable, e.g. $\sigma^2_{\text{VA,max}} = 10\sigma^2_{\text{VA}}$. If the VA has not been associated in the current time step or not enough amplitude estimates are available, the variance is set to the average of all previous variance values.

3.7 Tracking Results

To evaluate the performance of the tracking algorithm, labeled CIR measurements with known positions were taken along two trajectories using the M-Sequence channel sounder. The measurement setup in the seminar room of the SPSC Lab is shown in Fig. 3.9. It shows the two anchors A1 and A2, two trajectories (In black trajectory 1 and in blue trajectory 2) and the direction in which the mobile agent moves. The agent transmits an UWB signal which is received by the two anchors. Two wall segments are highlighted, segment 1 is a blackboard and segment 2 is a window. Those segments are marked as they are the reflectors of the VAs analyzed in Section 3.7.2. There, the influence of the variance estimation is shown. The room is basically rectangular but has many details along its walls, which results in a large number of VAs.

The measurement data used for the analysis were also acquired on a 5×5 grid with 1 cm spacing. A detail plot of the beginning of the first trajectory showing those dense points can be seen in Fig. 3.10. Using each grid point for a different trajectory results in 25 similar trajectories, each with their own measurements.

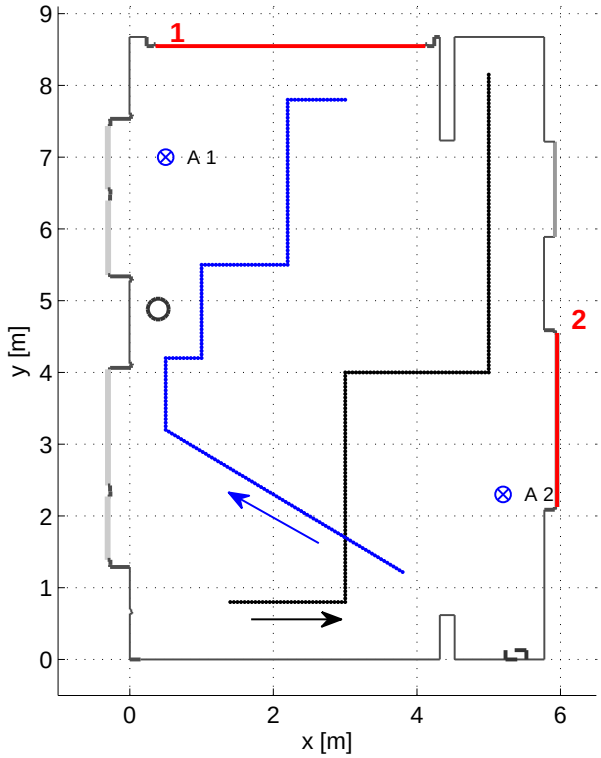

Figure 3.9: Measurement setup seminar room with the two anchors and the two used trajectories, trajectory 1 (black) and trajectory 2 (blue). The wall segments highlighted in red are a blackboard (segment 1) and a window (segment 2).

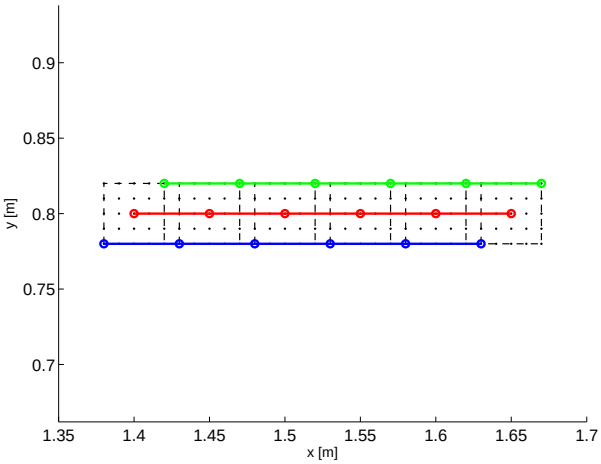

Figure 3.10: Plot showing how the dense grid around the trajectory points is used. The red point marks the main trajectory point. Each point of a sub-grid is used for a trajectory, resulting in 25 trajectories.

3.7.1 Tracking without Variance Estimation

The chosen pulse shaping and tracking parameters are shown in Tab. 3.1. The tracking is evaluated at each of the 25 trajectories using the sub-grid points. The tracking plots show only the tracking along the main trajectory point in the middle of the sub-grid (shown in red in Fig. 3.10). The CDFs show the results of all 25 runs and the average CDF. The results along the first trajectory in Fig. 3.11(a) show that the tracking works and only at the end the

Parameter	Value trajectory 1	Value trajectory 2
Discrete time step Δt	0.1 s	0.1 s
Maximum velocity $v_{\max}$	0.5 m/s	0.5 m/s
Measurement noise variance σ_z^2	0.0049 m^2	0.0049 m^2
Cut-off distance d_c	0.15 m	0.15 m
Initial mobile position variance σ_i^2	0.01 m^2	0.01 m^2
Highest VA Order	2	2
Center frequency f_c	7 GHz	7 GHz
Roll-off factor β_R	0.5	0.5
Pulse duration T_p	0.5 ns	0.5 ns
Maximum number of extracted MPCs K	20	20

Table 3.1: Pulse shaping and tracking parameters

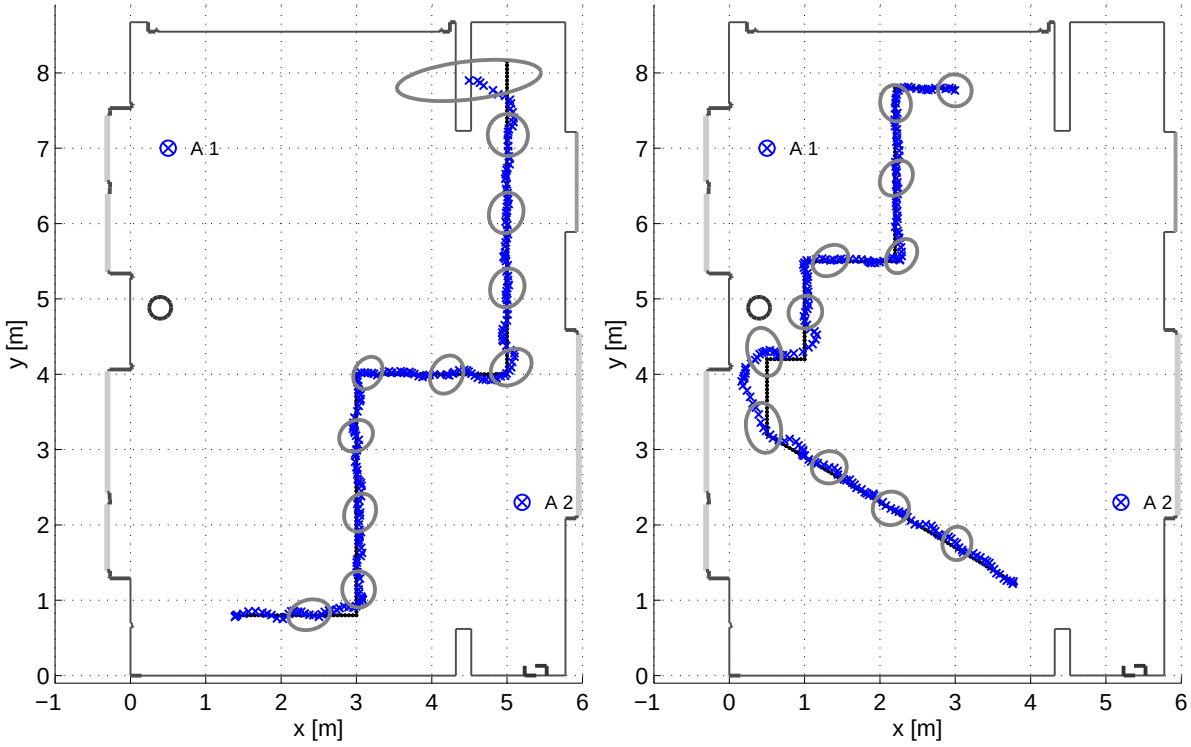

(a) Tracking result of trajectory 1

(b) Tracking result of trajectory 2

Figure 3.11: Tracking results for both trajectories. The error ellipses are plotted for every 20-th time step and enlarged by a factor of 10. Pulse shaping parameters: $f_c = 7$ GHz, $\beta_R = 0.5$ and $T_p = 0.5$ ns

estimator gets off the track and runs into the wall. There is a difficult geometric region where only the LOS component of A2 is available. Also, just a few VAs are visible and the MPCs of the reflections are very close to each other which makes it hard to extract and associate the delays correctly. Also the error ellipse, which is plotted enlarged by a factor of 10, shows that there is comparably more uncertainty than before and its minor axis is directed towards A2 as most information comes from it. Along the rest of the trajectory the error ellipses are nearly circular shaped which indicates that there is information coming from all directions. The hardest part

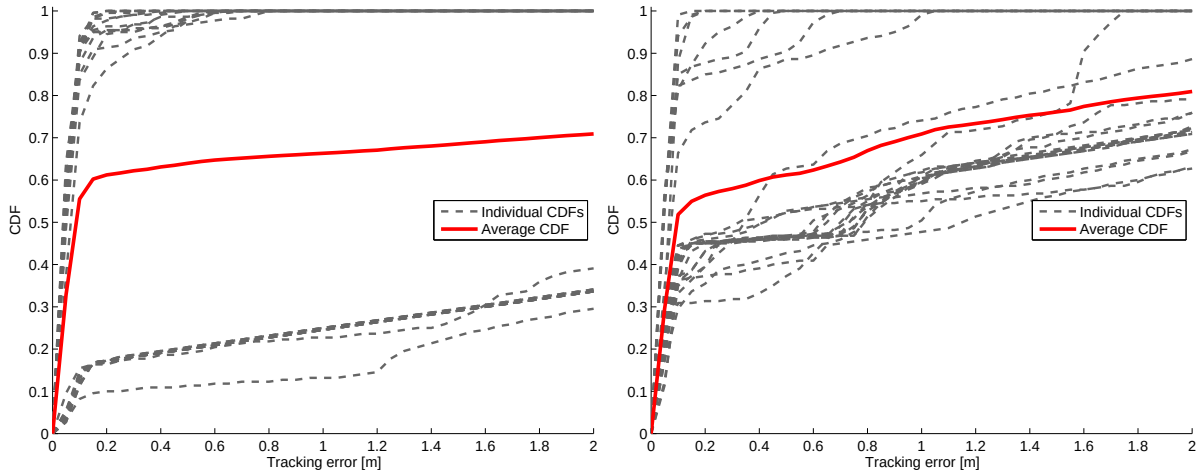

(a) CDF of tracking result in Fig. 3.11(a) of trajectory 1

(b) CDF of tracking result in Fig. 3.11(b) of trajectory 2

Figure 3.12: CDFs of tracking results in Fig. 3.11 over all 25 trajectories and the total CDF of all errors.

for the tracker on this trajectory is the last corner before the long straight part where at the end the difficult geometric region is entered. Here, in some of the 25 runs the tracker is not able to get around the corner and runs into the wall and cannot recover, therefore the CDFs show high tracking errors in some cases (Fig. 3.12(a)).

The tracking of the second trajectory is shown in (Fig. 3.11(b)). Here, the hardest part for the tracker is after the diagonal part of the trajectory because of the pillar in the room (the circle in the floor plan). Here, A1 is blocked resulting in a non-line-of-sight (NLOS) situation and also it is a difficult trajectory with two corners in it. The tracker has some problems but is able to recover to the path. The error ellipse again shows that behind the pillar most information comes from A2 and reflections of A1 from the wall on the right-hand-side as the direct path to A1 is blocked. On some of the 25 trajectories the tracker has problems here, some go around the pillar on the left side and can recover, some run into the wall on the left side and are not able to recover, therefore there are some CDFs in Fig. 3.12(b) with a large tracking error.

3.7.2 Tracking using the Variance Estimation

Parameter	Value
Minimum trajectory length $d_{\min}$	0.9 m
Maximum trajectory length $d_{\max}$	1 m
Minimum # amplitude estimates $N_{\min}$	15
Default variance σ^2_{VA}	$0.07\,\mathrm{m}^2$
Variance for unreliable VAs $\sigma^2_{\mathrm{VA,max}}$	$10\sigma^2_{\mathrm{VA}}$

Table 3.2: Additional parameters for the variance estimation

The same scenarios as in the previous section were evaluated using the online estimation of the VA variance as described in Section 3.6. The additional parameters are shown in Tab. 3.2 and are equal for both trajectories. When comparing the tracking result without the variance estimation (Fig. 3.11) with the results using the estimation in Fig. 3.13, it can be seen that

the robustness is increased for both trajectories which is also indicated by the smaller error ellipses, which are now enlarged by a factor of 20 . Inspecting the CDF for the first trajectory in Fig. 3.14(a) shows that on average the tracking error is approximately below 12 cm in 90% of the cases but there is still one run which was not able to make it around the last corner. For the second trajectory, the CDF in Fig. 3.14(b) shows that all runs were good and the average tracking error is below 10 cm in 90% of the cases.

The tracking results in Fig. 3.13 suggest that the tracker has some bias, i.e. the track has a constant offset from the trajectory. This was not observable in Fig. 3.11 because there the tracking was less stable. The bias might stem from an erroneous floor plan or erroneous anchor positions. Those influences is accounted for in Section 4.4.1.

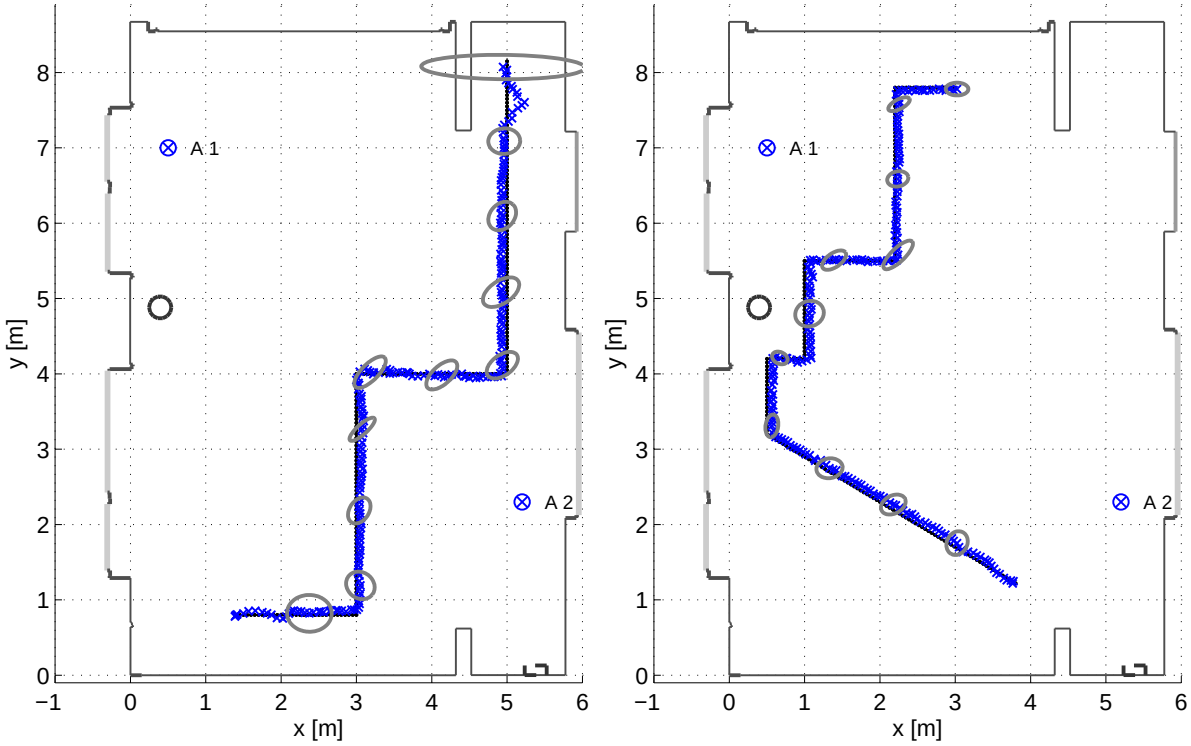

(a) Tracking result of trajectory 1

(b) Tracking result of trajectory 2

Figure 3.13: Tracking results for both trajectories using the online variance estimation. The error ellipses are plotted for every 20-th time step and enlarged by a factor of 20. Pulse shaping parameters: $f_c = 7\,GHz$, $\beta_R = 0.5$ and $T_p = 0.5\,ns$

Fig. 3.15 and Fig. 3.16 show the evolution of the estimated standard deviation of the range estimates for both trajectories. The plots show the two anchors and the most often associated VAs of each anchor. VA 19 models the reflection at the blackboard at the top of the floor plan with respect to A1, VA 1192 models the reflection from the window on the right-hand-side of the room with respect to A2. The default standard deviation σ_{VA}=0.07 m is chosen because it delivered a good tracking performance. The plots also show the values of the offline estimation for comparison. As the offline estimation delivers only a single value for each VA, it is plotted as horizontal line in the comparison plots with the matching color to the online result, but only for those time steps in which the VA is visible.

For the first trajectory, the results of the offline estimation match the online results well (Fig. 3.15). The result of VA 19 is also quite similar except for the peak at time step 190. This occurs before the tracker enters the difficult geometric region. The reflection from the blackboard becomes weaker and at some point is not available any more. This can also be seen

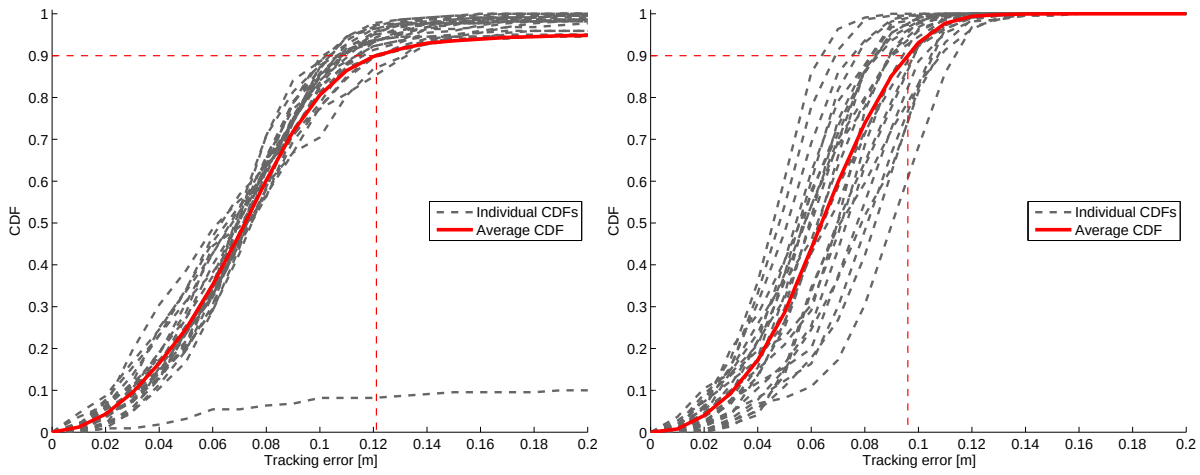

(a) CDF of tracking result in Fig. 3.13(a) trajectory 1 (b) CDF of tracking in Fig. 3.13(b) trajectory 2

Figure 3.14: CDFs for tracking results in Fig. 3.13 with online variance estimation, for all 25 trajectories and the mean over all.

in the offline comparison value, which shows that after time step 190 the VA is not visible any more. Therefore, there is one unreliable estimation leading to the peak and then there is no association any more and the standard deviation is averaged as described in Section 3.6. The results of the anchors A1 and A2 are very similar to the offline results.

The evolution for the second trajectory in Fig. 3.16 shows comparable results for A2 and VA 1192. A1 and VA 19 are also approximately on the same level as the offline results except between time steps 90 and 110. During these time steps the tracker is behind the pillar and the anchor A1 and also the reflection with the blackboard are blocked, resulting in a higher variance.

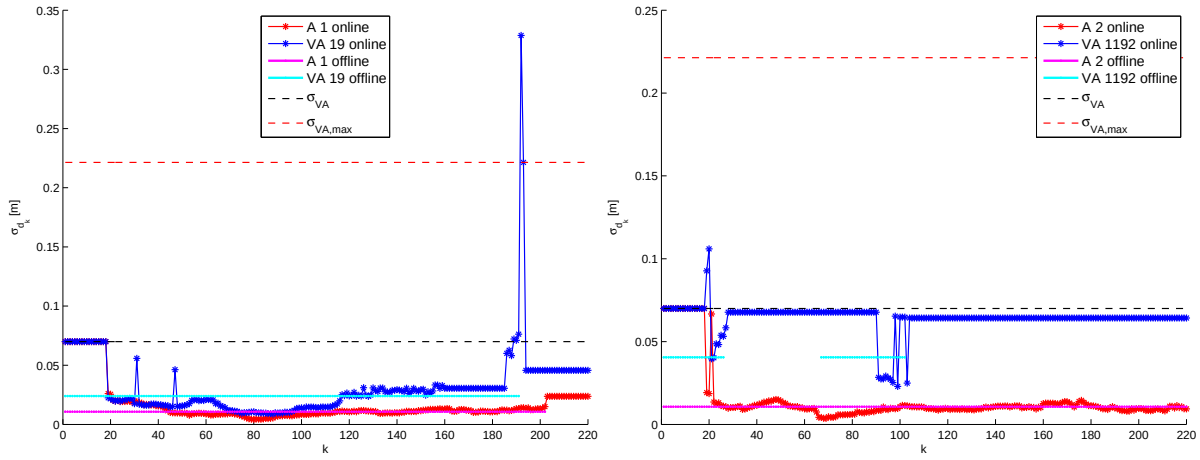

(a) Results of A1 (b) Results of A2

Figure 3.15: Evolution of the online estimation of the standard deviation of the VA position for the tracking of trajectory 1 in Fig. 3.13(a), compared to the offline results plotted as horizontal lines. The offline results are plotted for the time steps in which the VA is visible.

For a comparison, the same analysis was also done with a bandwidth of 1 GHz. The tracking results for both trajectories are shown in Fig. 3.17, the respective CDFs in Fig. 3.18. They show that due to the smaller bandwidth the tracking does not work that well and is not very suitable

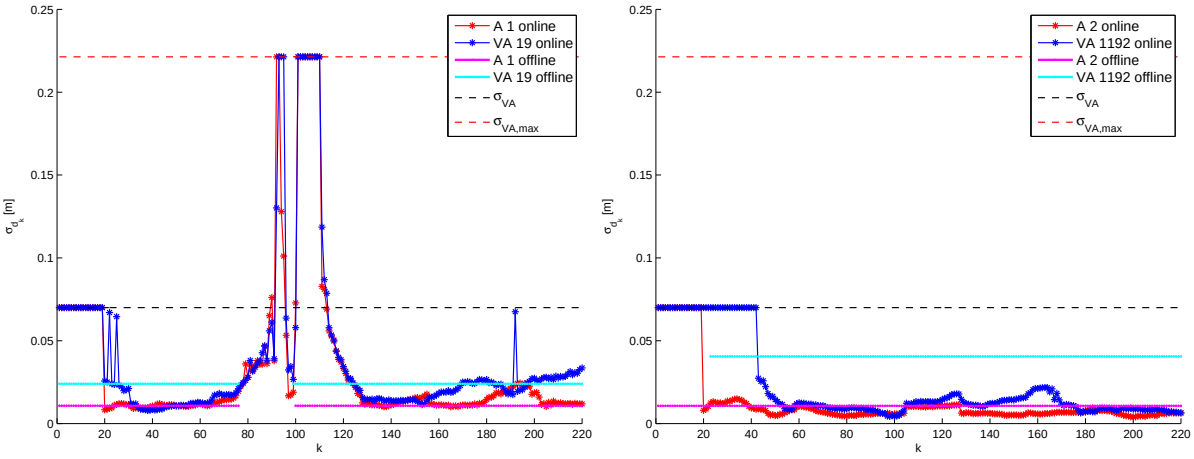

(a) Results of A1

(b) Results of A2

Figure 3.16: Evolution of the online estimation of the standard deviation of the VA position for the tracking of trajectory 2 in Fig. 3.13(b), compared to the offline results plotted as horizontal lines. The offline results are plotted for the time steps in which the VA is visible.

for this room.

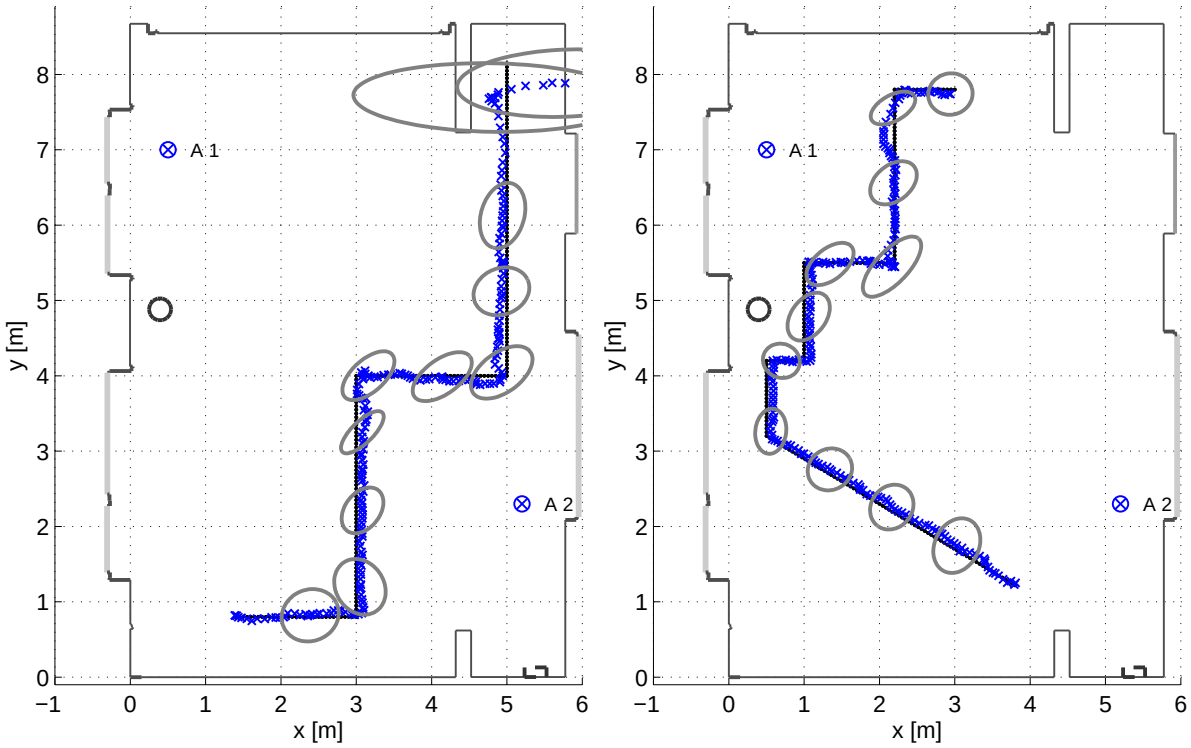

(a) Tracking result of trajectory 1

(b) Tracking result of trajectory 2

Figure 3.17: Tracking results for both trajectories using the online variance estimation. The error ellipses are plotted for every 20-th time step and enlarged by a factor of 20. Pulse shaping parameters: $f_c = 7\ GHz$, $\beta_R = 0.5$ and $T_p = 1\ ns$

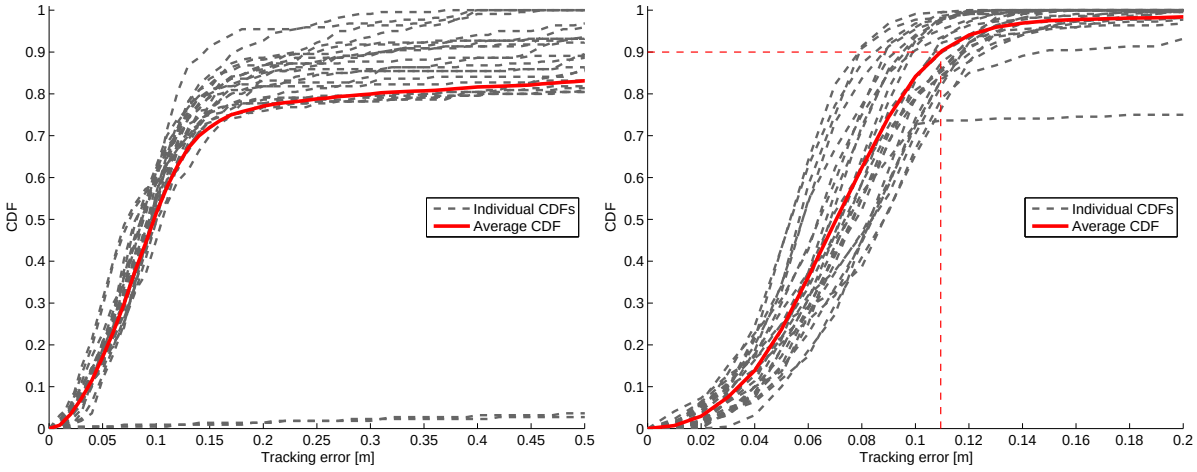

(a) CDF of tracking result in Fig. 3.17(a) trajectory 1

(b) CDF of tracking in Fig. 3.17(b) trajectory 2

Figure 3.18: CDFs for tracking results in Fig. 3.13 with online variance estimation, for all 25 trajectories and the mean over all.

4

VA Discovery and Tracking: A SLAM Approach

The traditional SLAM problem is well investigated. As described in [13], it is possible for a mobile to build a map of an unknown environment and concurrently estimate its own position within this environment. When using a Bayes-filter for tracking, the standard approach is to extend the state vector to hold not only information on the mobile but also on features which have been discovered while the mobile is moving. Features can be different types of geometric forms, e.g. points, lines (walls), etc. This means that the state vector increases in size with every new discovered feature.

Traditional SLAM approaches often use range and bearing measurements to identify features. In [16], a millimeter wave radar (MMWR) is mounted onto a car which measures range and bearing. This allows estimating a point type feature in a single time step. Combining multiple measurements by some object recognition algorithms allows to estimate more complex features, e.g. a wall or a pillar.

In this work, the features are unknown VAs which should be discovered and added to the state vector. VAs are point type features. Using UWB measurements, only range measurements are available, which makes it impossible to estimate the position of a VA in a single time step.

Section 4.1 describes how the EKF is extended to track not only the mobile agent but also the VA positions. The methodology of discovering VAs and adding them to the state vector is described in Section 4.2. Simulation results in a hypothetical room are shown in Section 4.3 and results in a real room using both synthetic and measurement data are shown in Section 4.4.

4.1 Adapting the EKF for VA Tracking and VA Discovery

In a first step towards SLAM, the four dimensional EKF state vector is expanded by the VA positions of the initially known VAs. This allows for VA tracking to compensate for errors in their positions using the measurements. The VA positions might be erroneous due to imprecise measurements of the room geometry and inaccurate positioning of the anchors. The corrections are done in the EKF update step, there is no motion model behind the VAs as their position is still assumed to be constant.

The correction of VA positions is referred to as re-localization. It can also be done offline in a calibration phase together with the previously introduced offline variance estimation as in [29]. The re-localization here is done online in each time step. Results for the offline re-localization in the seminar room are available and will be compared with the online results in Section 4.4.

The state vector at time step n is expanded by the x and y coordinates of the VAs

$$\boldsymbol{x}_n = \begin{bmatrix} x_{m,n} & y_{m,n} & v_{x,n} & v_{y,n} & x_{\mathrm{VA}_1,n} & y_{\mathrm{VA}_1,n} & \dots & x_{\mathrm{VA}_M,n} & y_{\mathrm{VA}_M,n} \end{bmatrix}^T \tag{4.1}$$

where M is the number of initially known VAs. Therefore, the size of the state vector increases by $2M$. Consequently, also the covariance matrix $\boldsymbol{P}_n$ has to be adapted

$$\boldsymbol{P}_n = \begin{bmatrix} \boldsymbol{P}_{m,m,n} & \boldsymbol{P}_{m,\mathrm{VA},n} \\ \boldsymbol{P}_{\mathrm{VA},m,n} & \boldsymbol{P}_{\mathrm{VA},\mathrm{VA},n} \end{bmatrix} \tag{4.2}$$

where $\boldsymbol{P}_{m,m,n}$ is the original 4×4 covariance matrix of the tracking EKF, $\boldsymbol{P}_{m,\mathrm{VA},n}$ is the covariance between the state of the mobile agent and the VAs and $\boldsymbol{P}_{\mathrm{VA},\mathrm{VA},n}$ is the covariance between the VAs. As the VA positions are assumed to be constant, the state transmission matrix $\boldsymbol{F}$ is expanded with an identity matrix for the VAs and zeros outside

$$\boldsymbol{F} = \begin{bmatrix} \boldsymbol{F} & \boldsymbol{0}_{4\times 2M} \\ \boldsymbol{0}_{2M\times 4} & \boldsymbol{I}_{2M\times 2M} \end{bmatrix}. \tag{4.3}$$

As the predicted covariance matrix $\boldsymbol{P}_n^-$ is computed using (3.11), the covariance matrix $\boldsymbol{Q}_n$ of the process noise has to expanded by zeros

$$\tilde{\boldsymbol{Q}}_n = \begin{bmatrix} \boldsymbol{Q}_n & \boldsymbol{0}_{4\times 2M} \\ \boldsymbol{0}_{2M\times 4} & \boldsymbol{0}_{2M\times 2M} \end{bmatrix}. \tag{4.4}$$

The observation matrix $\boldsymbol{H}_n$ has to be expanded by $2M$ columns

$$\boldsymbol{H}_n = \begin{bmatrix} \left.\frac{\partial d_{n,1}}{\partial x_m}\right|_{\boldsymbol{x}_{\mathrm{VA}_1,n}} & \left.\frac{\partial d_{n,1}}{\partial y_m}\right|_{\boldsymbol{x}_{\mathrm{VA}_1,n}} & 0 & 0 & \cdots \\ \vdots & & & & \ddots \\ \left.\frac{\partial d_{n,M}}{\partial x_m}\right|_{\boldsymbol{x}_{\mathrm{VA}_M,n}} & \left.\frac{\partial d_{n,M}}{\partial y_m}\right|_{\boldsymbol{x}_{\mathrm{VA}_M,n}} & 0 & 0 & \cdots \end{bmatrix} \\ \begin{bmatrix} \cdots & \left.\frac{\partial d_{n,1}}{\partial x_{\mathrm{VA}}}\right|_{\boldsymbol{x}_{\mathrm{VA}_1,n}} & \left.\frac{\partial d_{n,1}}{\partial y_{\mathrm{VA}}}\right|_{\boldsymbol{x}_{\mathrm{VA}_1,n}} & \cdots & 0 & 0 \\ \ddots & & & & & \vdots \\ \cdots & 0 & 0 & \cdots & \left.\frac{\partial d_{n,M}}{\partial x_{\mathrm{VA}}}\right|_{\boldsymbol{x}_{\mathrm{VA}_M,n}} & \left.\frac{\partial d_{n,M}}{\partial y_{\mathrm{VA}}}\right|_{\boldsymbol{x}_{\mathrm{VA}_M,n}} \end{bmatrix} \tag{4.5}$$

where $d_{n,m}$ is the circle equation (3.18) and all derivatives are evaluated at the specified VA position $\boldsymbol{x}_{\mathrm{VA}_m,n}$ and the predicted state vector $\boldsymbol{x}_n^-$ which is not shown in the equation due to reasons of space.

The coordinates of a discovered VA are added to the state vector $\boldsymbol{x}_n$

$$\begin{aligned} \boldsymbol{x}_n = \begin{bmatrix} x_{m,n} & y_{m,n} & v_{x,n} & v_{y,n} & x_{\mathrm{VA}_1,n} & y_{\mathrm{VA}_1,n} & \cdots \\ \cdots & x_{\mathrm{VA}_M,n} & y_{\mathrm{VA}_M,n} & x_{\mathrm{VA}_{M+1},n} & y_{\mathrm{VA}_{M+1},n} \end{bmatrix}^T \end{aligned} \tag{4.6}$$

where $x_{\mathrm{VA}_{M+1},n}$ and $y_{\mathrm{VA}_{M+1},n}$ are the coordinates of the new VA. The associated covariance $\boldsymbol{P}_n$ is expanded with the covariance between agent and the new VA $\boldsymbol{P}_{m,\mathrm{VA}_{M+1},n}$, the covariance between existing VAs and the new VA $\boldsymbol{P}_{\mathrm{VA},\mathrm{VA}_{M+1},n}$ and the error in the new VA position $\boldsymbol{P}_{\mathrm{VA}_{M+1},\mathrm{VA}_{M+1},n}$ resulting in $\boldsymbol{P}_{n+1}$ [32, 33]

$$\boldsymbol{P}_{n+1} = \begin{bmatrix} \boldsymbol{P}_{m,m,n} & \boldsymbol{P}_{m,\mathrm{VA},n} & \boldsymbol{P}_{m,\mathrm{VA}_{M+1},n} \\ \boldsymbol{P}_{\mathrm{VA},m,n} & \boldsymbol{P}_{\mathrm{VA},\mathrm{VA},n} & \boldsymbol{P}_{\mathrm{VA},\mathrm{VA}_{M+1},n} \\ \boldsymbol{P}_{\mathrm{VA}_{M+1},m,n} & \boldsymbol{P}_{\mathrm{VA}_{M+1},\mathrm{VA},n} & \boldsymbol{P}_{\mathrm{VA}_{M+1},\mathrm{VA}_{M+1},n} \end{bmatrix} \tag{4.7}$$

where

$$\begin{bmatrix} \boldsymbol{P}_{\mathrm{VA}_{M+1},m,n} & \boldsymbol{P}_{\mathrm{VA}_{M+1},\mathrm{VA},n} \end{bmatrix} = \boldsymbol{G}_x \boldsymbol{P}_n \tag{4.8}$$

and

$$\boldsymbol{P}_{\mathrm{VA}_{M+1},\mathrm{VA}_{M+1},n} = \boldsymbol{G}_x \boldsymbol{P}_n \boldsymbol{G}_x^T + \boldsymbol{G}_z \boldsymbol{R}_n \boldsymbol{G}_z^T. \tag{4.9}$$

In (4.8) and (4.9), the covariance $\boldsymbol{P}_n$ is the covariance matrix of the time step in which the new VA is added and $\boldsymbol{R}_n$ is the measurement noise covariance. The matrices $\boldsymbol{G}_x$ (4.21) and $\boldsymbol{G}_z$ (4.26) are the Jacobians of the feature initialization function $g(\cdot)$ and are introduced in Section 4.2.2.

As already described, when adding a VA to the state vector also the covariance matrix of the process noise $\boldsymbol{Q}_n$ has to increase in size by adding zeros and the state transition matrix $\boldsymbol{F}$ is increased by adding a 2×2 identity matrix in the diagonal and zeros outside.

4.2 Identifying a new VA

VAs can be considered as point features which could be estimated in a single time step if range and bearing measurements were available. However, in this work only unassociated range measurements are used, which requires more measurements for the estimation of a features. With a single range measurement d_n at time n the VA can be anywhere on a circle with the agent position $\begin{bmatrix} x_{m,n}, y_{m,n} \end{bmatrix}^T$ in the center and the associated range measurement d_n being the radius

$$d_n = \sqrt{(x_{m,n} - x_{\mathrm{VA}_i})^2 + (y_{m,n} - y_{\mathrm{VA}_i})^2} \tag{4.10}$$

where x_{VA_i} and y_{VA_i} are the coordinates of the unknown VA. With two range measurements it is possible to reduce the possible solutions to two points (Fig. 4.1(a)). Having measured the range at three different points, which must not be collinear, allows to determine the position of the VA in a noiseless situation (Fig. 4.1(b)), in practice a point with some uncertainty is the result. However, typically the agent positions are close to each other as for the real-time application it is necessary to have multiple measurements per second. Therefore, a small number of mobile positions as in Fig. 4.1(b) will result in almost collinear points where the ambiguity cannot be resolved and the estimation of the VA position is ill-posed.

Furthermore, the typical movement of persons and robots will tend to be along a straight line. This leads to situations where none of the two possible solutions disappears and there would still be an ambiguity (Fig. 4.2(a)). With range-only measurements it is not possible to determine

which of the solutions is the correct one until the mobile changes its direction and moves away from the straight line (Fig. 4.2(b)).

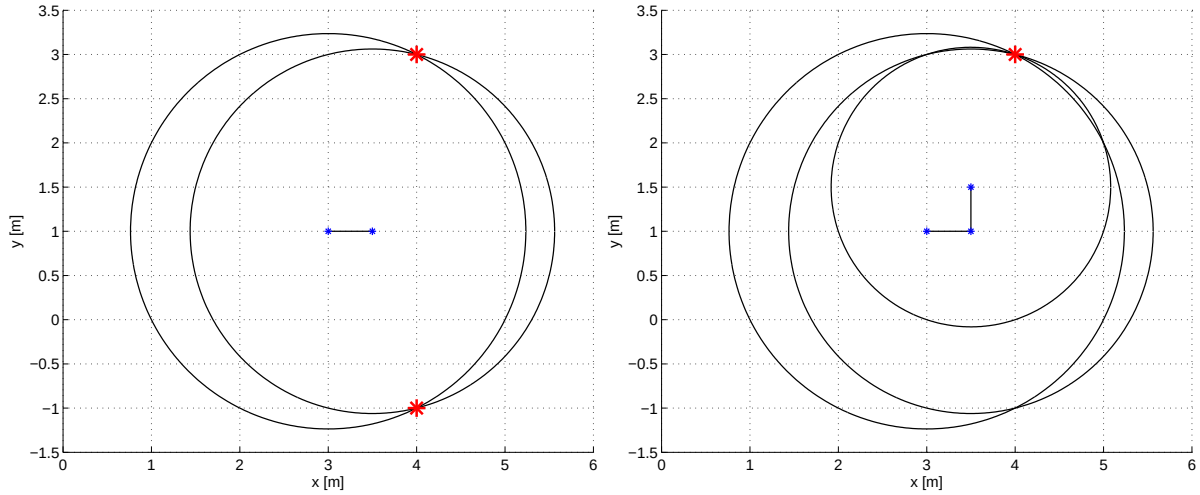

(a) Two range measurements result in two possible VA positions

(b) Three range measurements on noncollinear points result in a single VA

Figure 4.1: Identifying a VA from range-only measurements

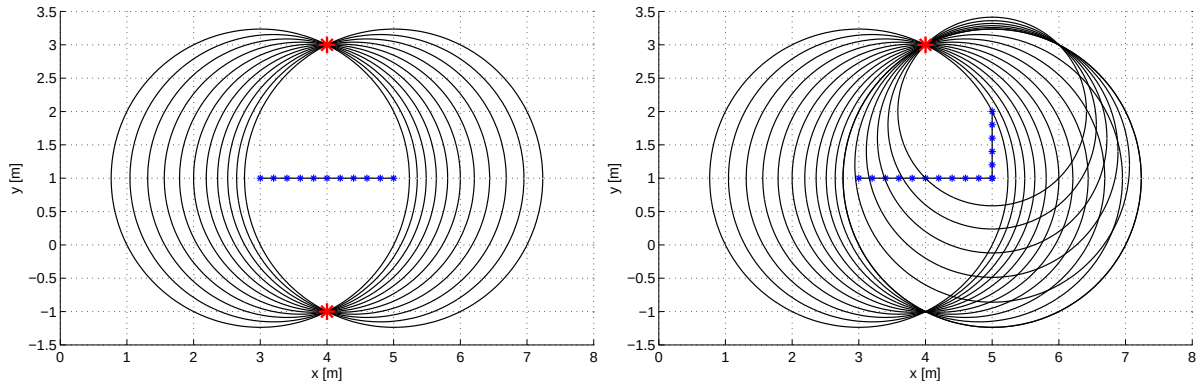

(a) Range measurements along a straight line (collinear mobile positions) cannot resolve the ambiguity

(b) Here the ambiguity can be resolved as the mobile moves away from the straight line

Figure 4.2: Identifying a VA from range-only measurements

Due to the mentioned limitation, it is necessary to store the agent positions and range measurements until the agent moves far enough away from a straight line and the ambiguity can be resolved. The block diagram in Fig. 4.3 shows how identifying VAs is done and how it is incorporated into the tracking scheme.

All range measurements which have not been associated to any known VA are used for VA discovery. The discovery is split into two stages. In the first stage, similar distances which come from time steps close to each other are grouped together. If the group has enough measurements (at least two) a Range-Bancroft Least Squares algorithm [34] estimates the two possible VA positions. The agent positions are typically close to each other which makes them effectively collinear and therefore the ambiguity cannot be resolved. The result of this stage is a VA candidate pair consisting of the two possible VA positions which are used in the second stage. There, a recursive least squares (RLS) as described in the next section is used to track the each

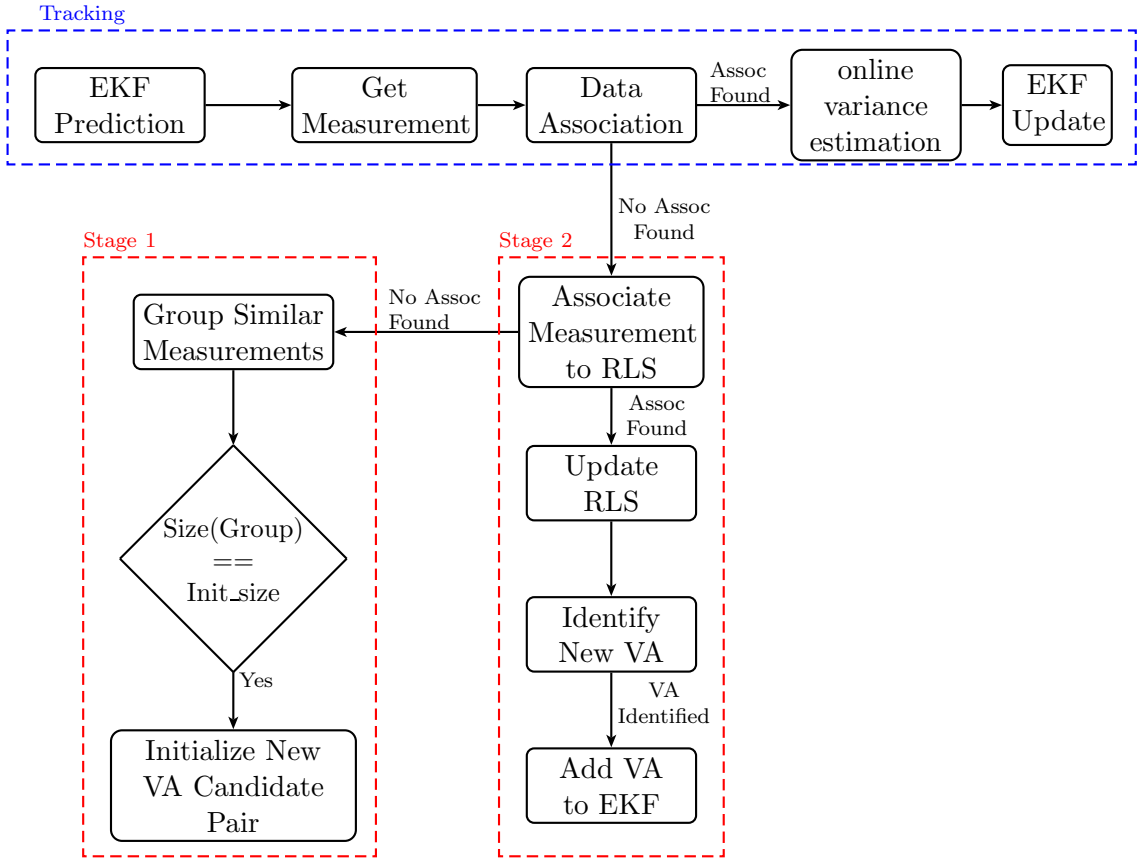

Figure 4.3: Block diagram showing how the two stages of the VA discovery are incorporated into the tracking system

VA candidate.

In the second stage, the unassociated ranges are associated to the VA candidate pairs using the same data association function as for the known VAs (see Section 3.4). Measurements which cannot be associated to any VA candidate are handed over to the first stage for finding new candidates. If a range measurement was associated in the second stage it is used for the update of the RLS. Typically, both VAs of a pair will be associated as long as the agent moves along a straight line. In this case the remaining candidate will be added as a new VA to the EKF state vector, and the other one will be dismissed and not be considered any more.

4.2.1 Recursive Least Squares (RLS)

RLS [35] was chosen ahead of a least squares algorithm to estimate the new VA $\boldsymbol{x}_{\mathrm{VA}_{M+1}}$ as it reduces the computational effort. With a standard Least squares algorithm the estimate $\hat{\boldsymbol{x}}_{M+1}$ is computed using the pseudoinverse of a $2 \times m$ matrix where m is the number of measurements. With every new measurement, the pseudoinverse has to be evaluated again for a matrix with increasing size. RLS on the other hand estimates $\hat{\boldsymbol{x}}_{M+1,n}$ using the estimate of the previous time step $\hat{\boldsymbol{x}}_{M+1,n-1}$ and the new measurement at time step n which drastically reduces the computational effort if a lot of measurements are obtained.

In this section, the new VA will be denoted $\boldsymbol{x}_{M+1}$, its estimate is $\hat{\boldsymbol{x}}_{M+1}$ and its coordinates will be x_{M+1} and y_{M+1}. Furthermore, the position of the agent at time step n is referred to as $\boldsymbol{x}_{m,n}$ with its coordinates $\left[\ x_m, y_m\ \right]^T$. As the RLS uses multiple measurements for tracking,

$\hat{\boldsymbol{x}}_{M+1,n}$ is the estimate of the new VA at time step n. The time step of the last measurement resolving the ambiguity and resulting into a VA estimate will be denoted as N_{rls}.

RLS starts with an initial guess $\hat{\boldsymbol{x}}_{M+1,0}$ which in this case is the result of the estimation using Range-Bancroft Least Squares and a constant estimation-error covariance $\boldsymbol{P}_0$ which has a chosen initial variance σ^2_{init} on its diagonal and is zero outside the diagonal. In subsequent steps, the estimated VA position and its estimation-error covariance are updated using the acquired range measurements. For the update, the estimator gain matrix $\boldsymbol{K}_n$ is computed using

$$\boldsymbol{K}_n = \boldsymbol{P}_{n-1}\boldsymbol{H}_n^T(\boldsymbol{H}_n\boldsymbol{P}_{n-1}\boldsymbol{H}_n^T + \boldsymbol{R}_n)^{-1}. \tag{4.11}$$

where $\boldsymbol{H}_n$ is an observation matrix . However, in this case it is a row vector containing the first order derivatives of the measurement function d (3.18) evaluated at the current agent position $\boldsymbol{x}_{m,n}$ and the current VA estimate

$$\boldsymbol{h}_n = \begin{bmatrix} \frac{\partial d_{n,M+1}}{\partial x_{\text{VA}}}\Big|_{\boldsymbol{x}_{m,n},\hat{\boldsymbol{x}}_{M+1,n-1}} & \frac{\partial d_{n,M+1}}{\partial y_{\text{VA}}}\Big|_{\boldsymbol{x}_{m,n},\hat{\boldsymbol{x}}_{M+1,n-1}} \end{bmatrix} \tag{4.12}$$

and R_n is the measurement noise covariance which is a scalar as only a single range measurement is acquired. Consequently, the estimator gain is a column vector denoted as $\boldsymbol{k}_n$.

The new estimated VA position $\hat{\boldsymbol{x}}_{M+1,n}$ is obtained using

$$\hat{\boldsymbol{x}}_{M+1,n} = \hat{\boldsymbol{x}}_{M+1,n-1} + \boldsymbol{k}_n(z_{n,M+1} - d_{n,M+1}). \tag{4.13}$$

Here, the difference between measured distance $z_{n,M+1}$ and expected distance $d_{n,M+1}$ is used to correct the estimate of the VA. The expected distance $d_{n,M+1}$ is computed using the circle equation (3.18) evaluated at the current agent position and the current VA estimate.

The error covariance is computed using

$$\boldsymbol{P}_n = (\boldsymbol{I}_{2\times 2} - \boldsymbol{k}_n\boldsymbol{h}_n)\boldsymbol{P}_{n-1}(\boldsymbol{I}_{2\times 2} - \boldsymbol{k}_n\boldsymbol{h}_n)^T + \boldsymbol{k}_n R_n \boldsymbol{k}_n^T. \tag{4.14}$$

4.2.2 The Feature Initialization Function

Section 4.1 describes how a discovered VA is added to the EKF. There, the Jacobians $\boldsymbol{G}_x$ and $\boldsymbol{G}_z$ of the feature initialization function $g(\cdot,\cdot)$ are needed in order to compute the covariance (4.7) for the new VA. In the general SLAM approach, the feature initialization function uses the state vector $\boldsymbol{x}_n$ (typically only the agent position) and the measurements $\boldsymbol{z}_n$ which have not been associated to any existing features to initialize a new feature $\hat{\boldsymbol{x}}_{M+1}$

$$\hat{\boldsymbol{x}}_{M+1} = g(\boldsymbol{x}_n, \boldsymbol{z}_n) \tag{4.15}$$

where $\boldsymbol{z}_n$ can be for example range and bearing measurements in order to be able to initialize a feature in a single time step n.

The derivatives are computed and evaluated at the respective mobile position and the initial-

ized feature position

$$\boldsymbol{G}_x = \left.\frac{\partial g}{\partial \boldsymbol{x}}\right|_{\boldsymbol{x}_n, \hat{\boldsymbol{x}}_{M+1}} \tag{4.16}$$

and

$$\boldsymbol{G}_z = \left.\frac{\partial g}{\partial \boldsymbol{z}}\right|_{\boldsymbol{x}_n, \hat{\boldsymbol{x}}_{M+1}}. \tag{4.17}$$

As explained previously, a single measurement is not enough to initialize a new VA using range-only measurements therefore the RLS is used to estimate the VA position using multiple measurements. The feature initialization function g is the least squares update function

$$g(\boldsymbol{x}_m, \boldsymbol{z}) = \boldsymbol{H}^\dagger(\boldsymbol{z} - \boldsymbol{d}(\boldsymbol{x}, \hat{\boldsymbol{x}}_{M+1})) \tag{4.18}$$

where $\boldsymbol{z}$ is a vector with all N_{rls} obtained range measurements. The i-th expected distance d_i in $\boldsymbol{d}(\boldsymbol{x}, \hat{\boldsymbol{x}}_{M+1})$ is computed by evaluating the circle equation at the agent position of the i-th measurement and the estimated VA at position $\left[\ \hat{x}_{M+1}, \hat{y}_{M+1}\ \right]^T$

$$d_i = \sqrt{(x_{m,i} - \hat{x}_{M+1})^2 + (y_{m,i} - \hat{y}_{M+1})^2}. \tag{4.19}$$

$\boldsymbol{H}$ is a $N_{\text{rls}} \times 2$ matrix stacking each $\boldsymbol{H}_n$ from (4.12) and $\boldsymbol{H}^\dagger$ is its pseudo-inverse.

$\boldsymbol{G}_x$ is the derivative of the feature initialization function w.r.t. to the state vector $\boldsymbol{x}$

$$\boldsymbol{G}_x = \frac{\partial g}{\partial \boldsymbol{x}} = \frac{\partial}{\partial \boldsymbol{x}}\left(\boldsymbol{H}^\dagger(\boldsymbol{z} - \boldsymbol{d}(\boldsymbol{x}, \hat{\boldsymbol{x}}_{M+1}))\right). \tag{4.20}$$

As the notation in the formula suggests, $\boldsymbol{z}$ does not depend on the state vector $\boldsymbol{x}$ so its derivative w.r.t. to $\boldsymbol{x}$ is zero. For simplicity, also $\boldsymbol{H}$ is assumed to be constant and not be a function of $\boldsymbol{x}$. The remaining task is to derive the expected distances w.r.t. to $\boldsymbol{x}$ and multiply those with $\boldsymbol{H}^\dagger$

$$\boldsymbol{G}_x = -\boldsymbol{H}^\dagger \frac{\partial}{\partial \boldsymbol{x}}\left(\boldsymbol{d}(\boldsymbol{x}, \boldsymbol{x}_{M+1})\right)\Big|_{\boldsymbol{x}, \boldsymbol{x}_{M+1}}. \tag{4.21}$$

As $\boldsymbol{x}$ is the state vector before the new VA is added, the derivative of $\boldsymbol{d}(\boldsymbol{x}, \hat{\boldsymbol{x}}_{M+1})$ is a matrix with all zeros except for the first two columns because $\boldsymbol{d}(\boldsymbol{x}, \hat{\boldsymbol{x}}_{M+1})$ only depends on the agent position in this case

$$\frac{\partial}{\partial \boldsymbol{x}}\left(\boldsymbol{d}(\boldsymbol{x}, \boldsymbol{x}_{M+1})\right) = \begin{bmatrix} \frac{\partial d_1}{\partial x_m} & \frac{\partial d_1}{\partial y_m} & \cdots & 0 \\ \vdots & & \ddots & \vdots \\ \frac{\partial d_{N_{\text{rls}}}}{\partial x_m} & \frac{\partial d_{N_{\text{rls}}}}{\partial y_m} & \cdots & 0 \end{bmatrix}. \tag{4.22}$$

Using this, $\boldsymbol{G}_x$ can be computed. If the assumption that $\boldsymbol{H}$ is constant is not taken, the chain rule for derivation would have to be applied and the derivative of the pseudo-inverse would be necessary [36].

To obtain $\boldsymbol{G}_z$, the feature initialization function is derived w.r.t. to the measurements $\boldsymbol{z}$

$$\boldsymbol{G}_z = \frac{\partial g}{\partial \boldsymbol{z}} = \frac{\partial}{\partial \begin{bmatrix} z_1 & \cdots & z_{N_{rls}} \end{bmatrix}^T} \left(\boldsymbol{H}^\dagger (\boldsymbol{z} - \boldsymbol{d}(\boldsymbol{x}, \hat{\boldsymbol{x}}_{M+1})) \right) \tag{4.23}$$

As both $\boldsymbol{H}^\dagger$ and $\boldsymbol{d}(\boldsymbol{x}, \hat{\boldsymbol{x}}_{M+1})$ do not depend on the measurements they can be considered constant and become zero for the derivative which reduces the function to

$$\boldsymbol{G}_z = \frac{\partial}{\partial \begin{bmatrix} z_1 & \cdots & z_{N_{rls}} \end{bmatrix}^T} \left(\boldsymbol{H}^\dagger \boldsymbol{z} \right). \tag{4.24}$$

The multiplication of $\boldsymbol{H}^\dagger$ with $\boldsymbol{z}$ can be written as

$$\boldsymbol{H}^\dagger \boldsymbol{z} = \begin{bmatrix} H_{11} & \cdots & H_{1N_{rls}} \\ H_{21} & \cdots & H_{2N_{rls}} \end{bmatrix} \begin{bmatrix} z_1 \\ \vdots \\ z_{N_{rls}} \end{bmatrix} = \begin{bmatrix} H_{11} z_1 + \cdots + H_{1N_{rls}} z_{N_{rls}} \\ H_{21} z_1 + \cdots + H_{2N_{rls}} z_{N_{rls}} \end{bmatrix}. \tag{4.25}$$

Taking the derivative w.r.t. to each measurement results in

$$\boldsymbol{G}_z = \frac{\partial}{\partial \begin{bmatrix} z_1 & \cdots & z_{N_{rls}} \end{bmatrix}^T} \left(\begin{bmatrix} H_{11} z_1 + \cdots + H_{1N_{rls}} z_{N_{rls}} \\ H_{21} z_1 + \cdots + H_{2N_{rls}} z_{N_{rls}} \end{bmatrix} \right) = \begin{bmatrix} H_{11} & \cdots & H_{1N_{rls}} \\ H_{21} & \cdots & H_{2N_{rls}} \end{bmatrix} = H^\dagger \tag{4.26}$$

which is a matrix that has already been evaluated and no further computations are necessary.

4.3 Simulation Results in an Artificial Environment

In this section, simulation results in the so-called L room (due to its L shape) are presented and analyzed. The purpose of the simulation in this room is to show the behavior of the algorithm in a controlled environment and also the results can be presented graphically as the room is geometrically not complicated and thus has only a relatively small VA set. Fig. 4.4 shows the floor plan of the L room with its two anchors.

For all the trajectories in this room, synthetic signals were generated which include the deterministic MPCs and additive white Gaussian noise (AWGN) (Fig. 4.5(a)). The delays of all MPCs were computed according to geometry but as the delay vector has a limited precision the pulses in the synthetic signals are not shifted by the exact delay but have a small error. This can be seen in Fig. 4.5(b) where the peak of the pulse is a little before the expected delay which is denoted by the dashed vertical line. The error can be considered as measurement noise which occurs in measured signals too. The maximum error is determined by the resolution of the delay vector which is 0.133 ns here which results in a maximum range error of

$$e_{\max} = \frac{1}{2} \Delta\tau \cdot c = \frac{1}{2} \cdot 0.133 \cdot 10^{-9} \cdot 3 \cdot 10^8 \approx 0.02\,\text{m}. \tag{4.27}$$

In the following plots different markers are used for different types of VAs, shown in Fig. 4.6. Green markers are used for anchor 1, magenta colored markers for anchor 2. Initially known

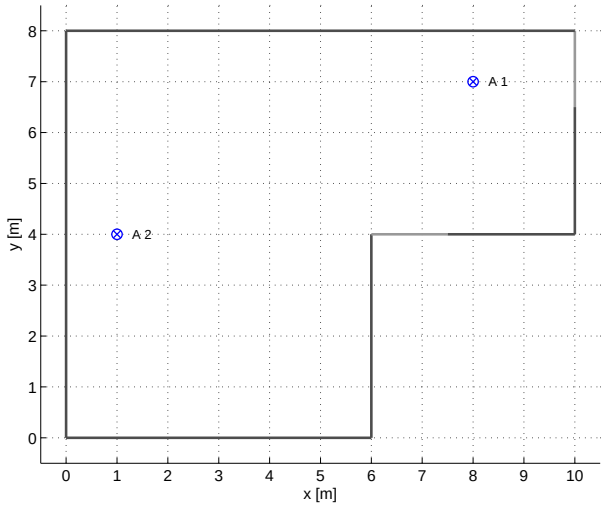

Figure 4.4: Floor plan of the L room, showing the two anchors

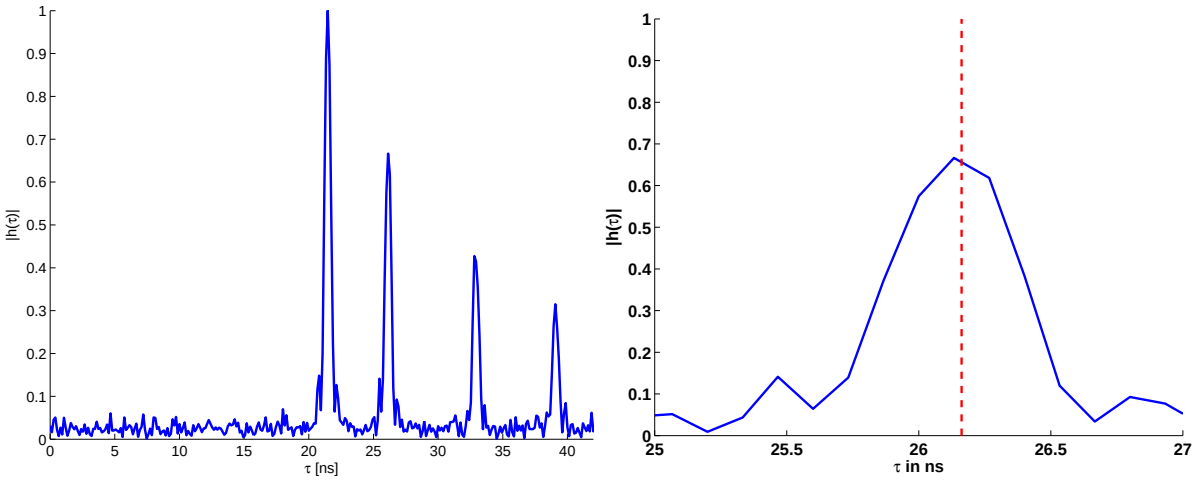

(a) Synthetic signal

(b) Synthetic signals zoomed with expected delay

Figure 4.5: Synthetic signal in L room, pulse shaping parameters f_c =7 GHz, $\beta_R = 0.5$ and T_p =0.5 ns

VAs are shown as square markers. VAs which are not known by the tracking system (unknown VAs) are shown using stars (order 1) and circles (order 2). The position of the VAs which are discovered by the algorithm are marked using crosses. Correction movements due to the VA tracking are plotted using blue stars for both channels as the association to the anchor should be clear by the discovered VA marker. The final position of the VA is highlighted using a red star and is the position of the VA in the last time step it was associated to a measured delay or the position in which the VA was when the simulation stopped when the end of the trajectory is reached.

In the discussion, the phrase ideal VA is used to refer to a VA from the precomputed VA set which best describes the discovered VA.

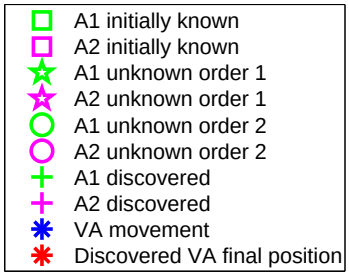

Figure 4.6: Legend used in the tracking plots for different types of VAs, A denotes an anchor.

Parameter	Value
Discrete time step Δt	0.3 s
Maximum velocity v_{max}	0.9 m/s
Measurement noise variance σ_z^2	0.0025 m^2
cut-off distance d_c	0.1 m
Initial mobile position variance σ_i^2	0.05 m^2
Highest VA Order of known VAs	1
Number of measurement to create a VA candidate pair	3
Minimum number of measurements to initialize a new VA	10
RLS initial error variance	10
RLS measurement variance R_z	0.04 m^2
Center frequency f_c	7 GHz
Roll-off factor β_R	0.5
Pulse duration T_p	0.5 ns
Maximum number of extracted MPCs K	15

Table 4.1: Parameters of the simulations in the L room

The following simulations all use the same initial conditions: All but four first order VAs are known initially and two first order VAs from each anchor are not known. The chosen parameters can be found in Tab. 4.1.

Fig. 4.7 shows a first example of the tracking and VA discovery. Here, a trajectory with one corner was chosen and the synthetic signals contained only MPCs of first order. Three of the four unknown VAs were found, VAs 13 and 14 were initialized well, VA 15 is approximately 2 m away from its ideal position but it can be seen that the erroneous initialization is corrected and the VA moves towards its ideal position. As the end of the trajectory is reached, the estimated VA cannot get close to the ideal position. The erroneous initialization is due to the fact that most of the measurements for this VA stem from the horizontal part of the trajectory where the tracking is poor, the CDF is shown in (Fig. 4.9(a)).

The fourth VA cannot be initialized because its MPCs can only be extracted from the signals along the vertical part of the trajectory and as all the points are approximately on a straight line, the ambiguity cannot be resolved. This is one of the drawbacks of a range-only system, a VA could be found and estimated very well but it will never be useful if all the measured ranges stem from agent positions on a straight line. For robots, movement along a straight line could be realistic. Humans tend to walk on paths parallel to walls. This changes if a mobile device is used during walking which distracts the user. In this case, there will be small direction changes along the path. This is a realistic scenario for a tracking and navigation software.

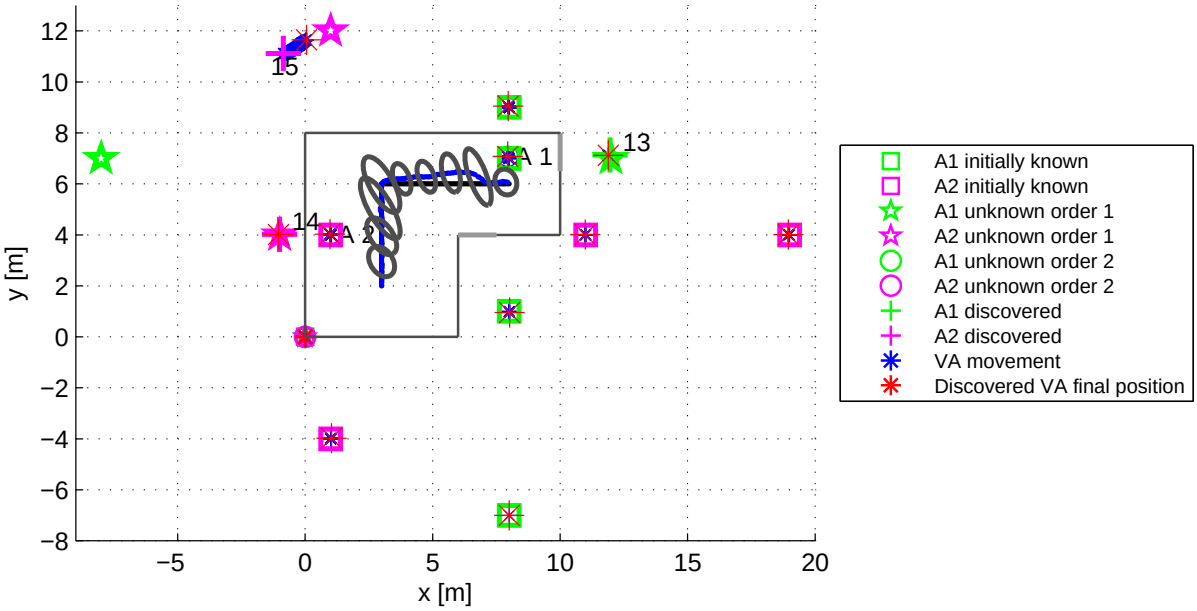

Figure 4.7: Tracking and VA discovery along a trajectory in the L room using synthetic signals containing only first order MPCs. The error ellipses are enlarged by a factor of 3, signal parameters: $f_c = 7\,GHz$, $\beta_R = 0.5$ and $T_p = 0.5\,ns$

The next scenario in Fig. 4.8 is basically the same trajectory as before but with some minor direction changes which could be the movement of a human looking on his mobile phone as mentioned before. Here, the tracking is better overall (Fig. 4.9(b)) than in the previous scenario, also all four VAs were found. This is possible due to the direction changes in the trajectory which allows to resolve the ambiguities. The initialization of the VAs is not as good as before, but the correction of the position allows them to get close to their ideal positions. This is not true for VA 15, which after some time steps has no associations anymore because the signal does not contain any significant MPCs.

The next scenario in Fig. 4.10 extends the previous one by using synthetic signals containing also MPCs of second order reflections. The set of initially known VAs is the same as before, i.e. contains only some of the first order VAs. All discovered VAs are corrected towards an ideal VA and also the tracking works well (Fig. 4.11). Not all unknown VAs are initialized as they are either not visible along the trajectory, they have no significant MPCs or the ambiguity of the VA candidates could not be resolved.

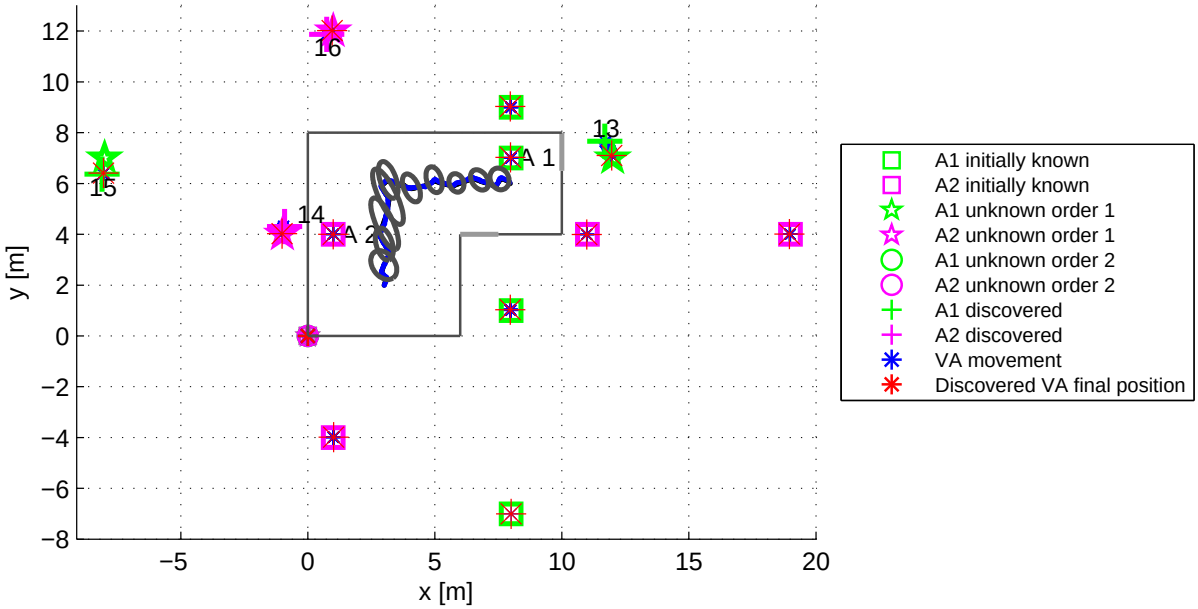

Figure 4.8: Tracking and VA discovery along a trajectory with direction changes in the L room using synthetic signals containing only first order MPCs. The error ellipses are enlarged by a factor of 3, signal parameters: $f_c = 7\ GHz$, $\beta_R = 0.5$ and $T_p = 0.5\ ns$

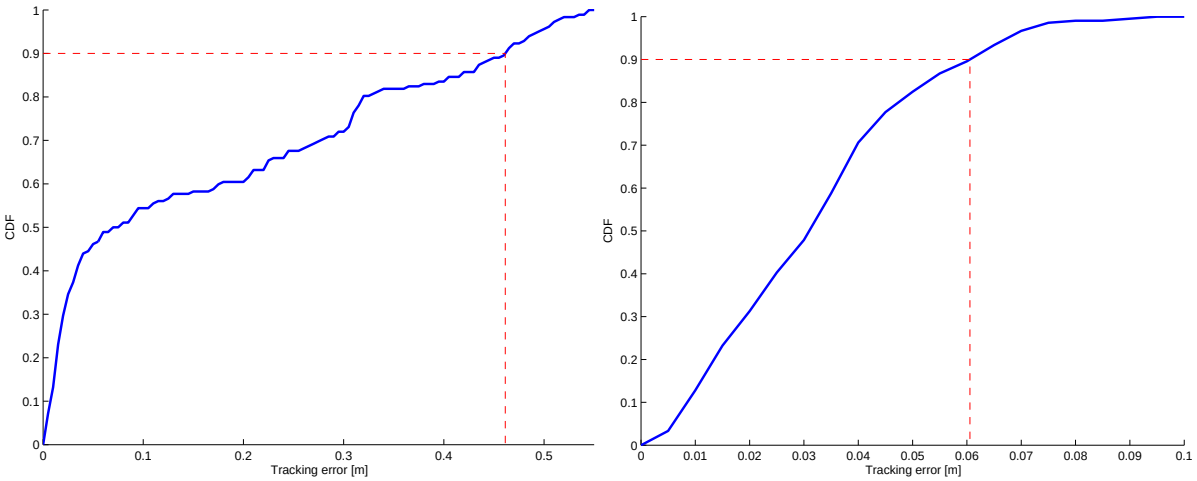

(a) CDF of the tracking in Fig. 4.7

(b) CDF of the tracking in Fig. 4.8

Figure 4.9: CDFs for tracking scenarios

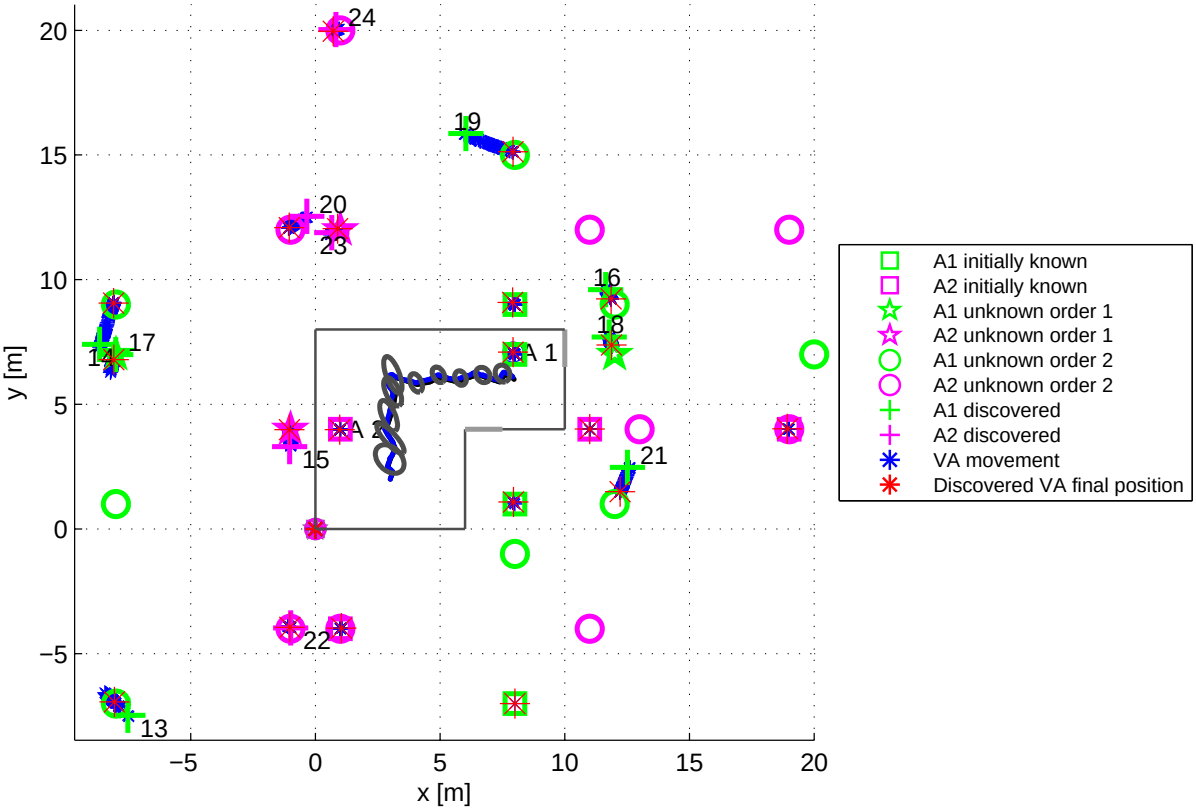

Figure 4.10: Tracking and VA discovery along a trajectory with direction changes in the L room using synthetic signals containing first and second order MPCs. The error ellipse is enlarged by a factor of 3, signal parameters: $f_c = 7\,GHz$, $\beta_R = 0.5$ and $T_p = 0.5\,ns$

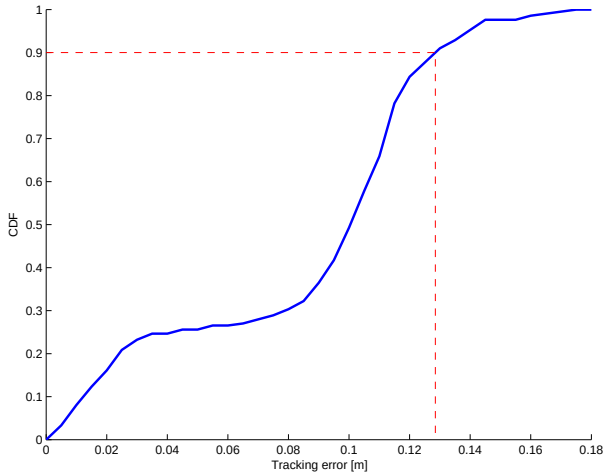

Figure 4.11: CDF of the tracking in Fig. 4.10

4.3.1 VA Discovery Issues

Fig. 4.12(a) shows an example of an initialized VA which is approximately 31 cm away from the ideal VA position. Although the ranges are accurate the estimated VA is not that accurate because of the imprecisely estimated agent positions. This can be seen in Fig. 4.12(b) where the estimated positions of the EKF (blue crosses) are connected to their ideal position on the trajectory (black dots). Although the tracking error here is below 10 cm for all points, the estimation error of the VA is large.

To show the influence of the tracking on the VA estimation, the estimation was done using the ideal position of the trajectory (Fig. 4.13(b)). In this case (Fig. 4.13(a)), the estimated VA is more accurate (4 cm) because of the correct agent positions. Still, there is an error due to the range error. From these results it is obvious that accurate tracking is necessary to ensure good estimation of the VAs.

As it was shown in the tracking plots, the system can cope with erroneous initialization by tracking the VA with the EKF and correct the position. This is shown in detail in Fig. 4.14 where the tracking is able to reduce the error of the VA to a few centimeters. However, it takes many time steps to reduce the error of the VA. The reason for this is the very long but narrow error surface of the measurement circles. Those circles plotted in grey can be seen in Fig. 4.12(a), Fig. 4.13(a) and Fig. 4.14. Fig. 4.14 shows that the VA moves along those circles and it takes many time steps (measurements) to reduce the estimation error due to the small gradient which allows the VA to make only small steps.

The evolution of the error of four selected VAs from the tracking shown in Fig. 4.10 is shown in Fig. 4.15. The error is here expressed as distance from the ideal VA position. All VAs except VA 13 show the same behavior of a decreasing error. Even VA 19 decreases the position error to below 15 cm although its initial error was over 2 m. VA 13 is corrected towards the ideal position but it shows non-monotonous behavior.

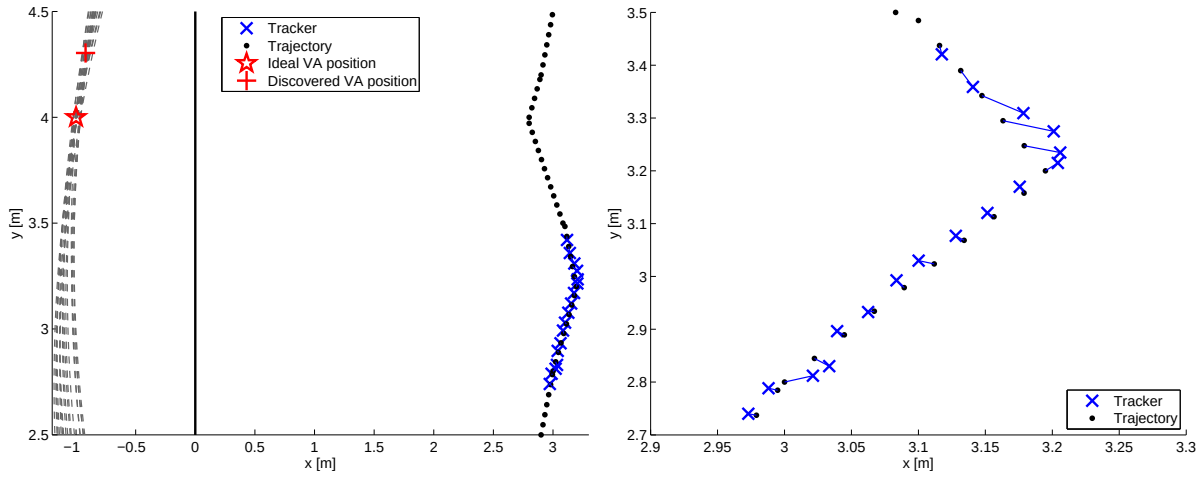

(a) VA initialization using tracked positions

(b) Zoom to the tracked positions

Figure 4.12: VA initialization using the tracked positions, showing the circles of the measured distances

The tracking cannot cope with all estimation errors. Fig. 4.16 shows an example where the tracking does not work or rather takes too long to bring the VA to the ideal position. In Fig. 4.16(a) the initialization of the VA is done using the positions tracked by the EKF. The initialized VA (green star) is far away from the ideal VA (green circle on the grey range circles). The range circles are very close to each other and therefore the gradient of the error is small. Due to this, it would need a lot of measurements to reach the ideal VA which is not the case here.

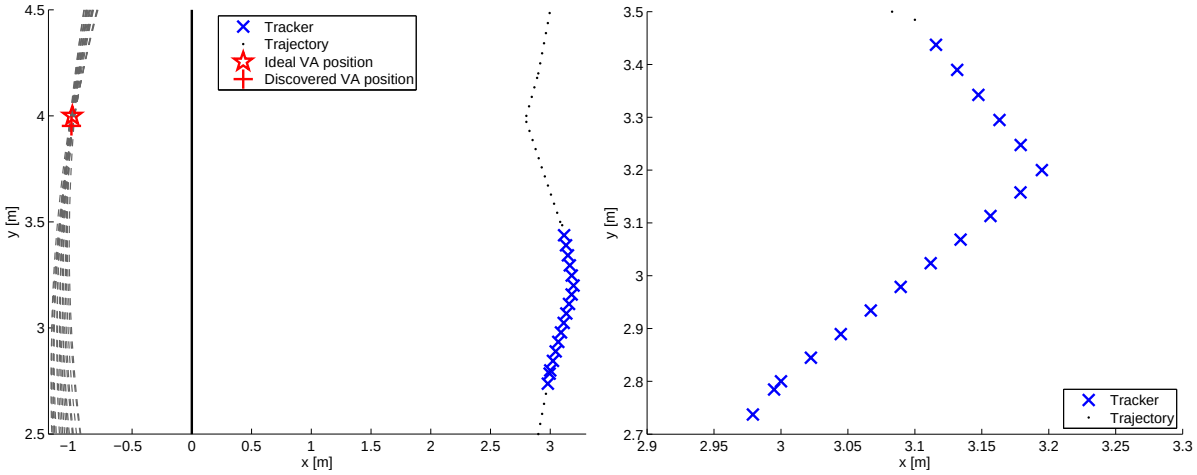

(a) VA initialization using ideal positions

(b) Zoom to the ideal positions

Figure 4.13: VA initialization using the ideal positions, showing the circles of the measured distances

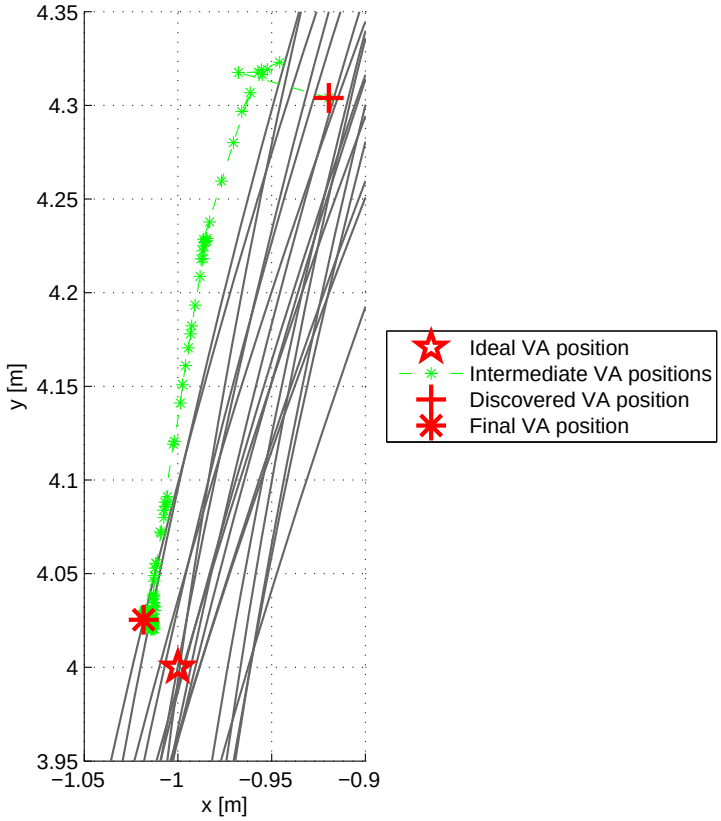

Figure 4.14: Detail view of tracking of an erroneously estimated VA

The final position of the VA (red star) is reached after 316 measurements and is still far away from the ideal position. With a better initialization using the perfect positions of the trajectory as shown in Fig. 4.16(b) the VA is estimated much better and is more likely to converge towards its ideal position. This again shows that a good tracking is crucial for the VA discovery.

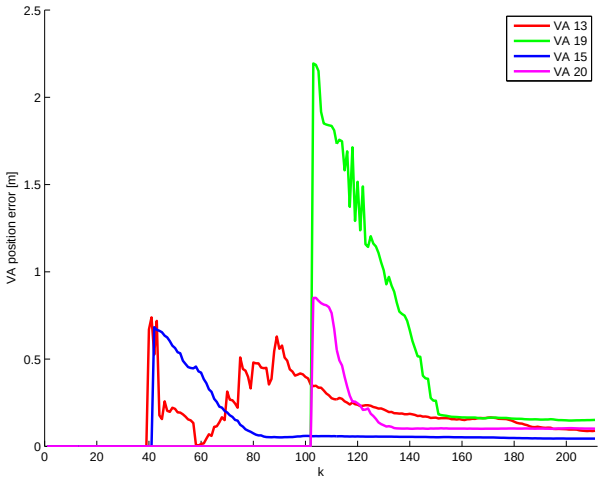

Figure 4.15: Error evolution of 4 selected VAs from the tracking in Fig. 4.10

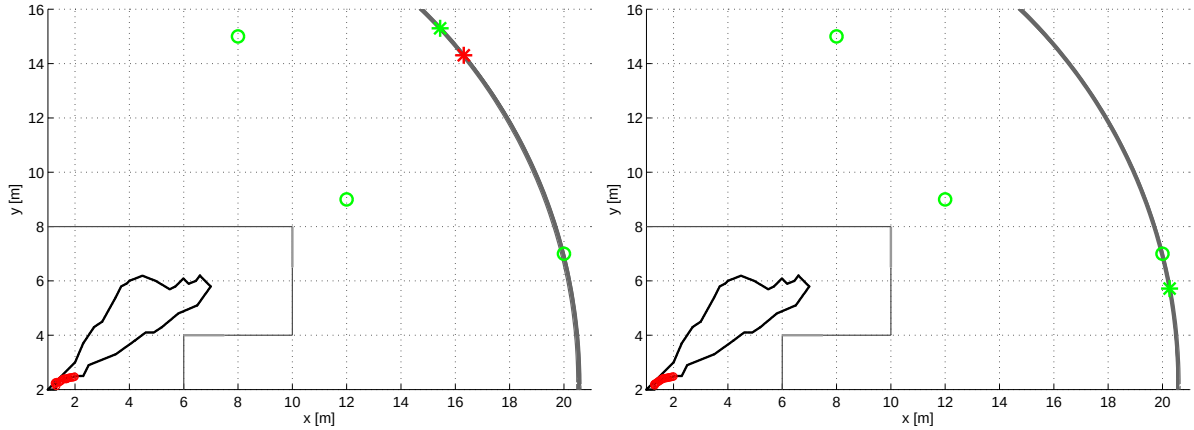

(a) VA initialization (green star) using EKF positions, after 316 time steps the VA (red star) still has a large error.

(b) VA initialization (green star) using ideal positions.

Figure 4.16: Comparison of VA initialization using EKF and ideal positions

4.3.2 The Data Association Problem of Discovered VAs

There is another problem which has not been addressed yet because it has not influenced the scenarios shown until now significantly. The problem is the visibility of the discovered VAs. For all initially known VAs, a lookup in the precomputed visibility table is done to determine which VA should be visible at the current position of the agent, and only those VAs are considered for the data association. However, for discovered VAs no such entry in the lookup table exists.

To determine the visibility of a VA its order and the associated wall segments have to be known to perform ray-tracing [28]. Fig. 4.17 shows an example in the L room. It should be tested whether VA 15 (a second order VA) is visible from the position $\boldsymbol{p}$ or not. The position of VA 15 can be determined by first mirroring A1 at the wall 7 to get VA 6 (first order) and then mirroring VA 6 w.r.t. to wall 3 to get VA 15. A situation in which the VA is not visible is shown in Fig. 4.17(a). There is no intersection with the associated wall segment 3 when launching a ray from the mobile $\boldsymbol{p}$ to VA 15.

In Fig. 4.17(b) the VA is visible as an intersection of the connection line from $\boldsymbol{p}$ to VA 15 with wall segment 3 is present. Furthermore, there is also a reflection of the signal reflected at

wall segment 3 with the upper wall segment 7 ending in A1. The solid lines denote the actual signal path, the dashed lines are the virtual paths to the VAs. In case there is an obstruction between the mobile agent and a wall segment, the VA would not be visible. This is an additional constraint to be checked.

To create a new lookup table entry for a VA, ray-tracing for every point on a grid inside the room would have to be done to determine from which position in the room the VA is visible. This is computationally very expensive and not feasible within the real-time constraint of this system. Furthermore, the main problem here is that determining the VA order and its associated wall segments it a hard task and also the scenario could be that not all walls are known which would make it impossible to determine the associated wall segment.

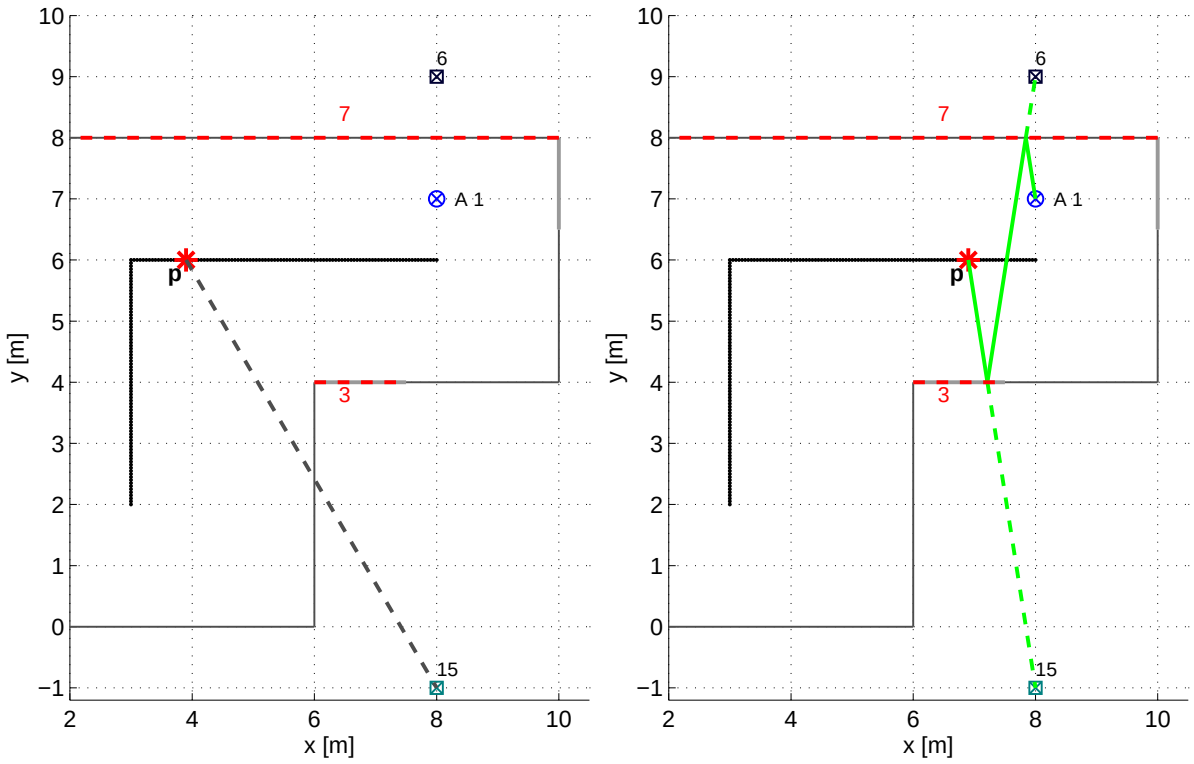

(a) VA 15 is not visible from $\boldsymbol{p}$

(b) VA 15 is visible from $\boldsymbol{p}$

Figure 4.17: Floor plan showing the VA visibility testing via ray-tracing for the second order VA 15. The red wall segments 3 and 7 are the segments associated to the VA.

In order to use a discovered VA for the tracking, only the distance between mobile agent and the respective VA can be used for data association. This situation is shown in Fig. 4.18, where all ideal positions of all second order VAs of A1 in the L room are shown. From the agent position $\boldsymbol{p}$, VA 8 and VA 9 have a similar distance. In the plotted situation, VA 9 is visible while VA 8 is not. In case both VAs have been discovered in previous time steps, on position $\boldsymbol{p}$ the data association using the range only and neglecting the visibility could associate both VAs to the same measurement and take the one with the smaller deviation. If the wrong VA is associated this could degrade the performance of the tracking. The more VAs are discovered, the more likely it will be that a wrong VA will be associated.

In order to deal with this problem, variance estimation is used which is a kind of reliability measure of a VA. If a VA is wrongly associated because it is geometrically not visible, the amplitudes of the extracted MPCs will vary strongly and cause the variance to increase. Due to the higher variance, the information of this VA has not much influence on the tracking, the

remaining problem is that due to the wrong association some good information of a VA might not be obtained, but as the variance of the wrongly associated VA increases, it at least does not harm the tracking performance.

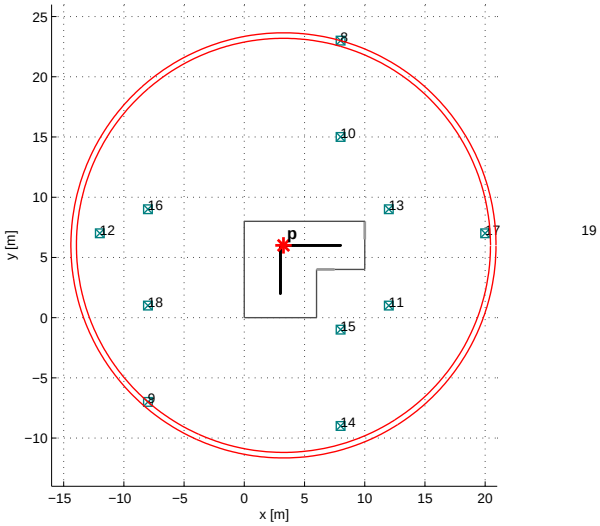

Figure 4.18: Floor plan showing the problem of data association for discovered VAs, where no visibility lookup table is available. The circles describe the ranges from the agent at position $\mathbf{p}$ *to the VAs 8 and 9.*

4.4 Simulation and Measurement Results in a Real Scenario

The seminar room has already been presented (see Fig. 3.9 for the floor plan), the analyses here use the same anchor positions and trajectories.

4.4.1 Online VA Re-localization using Measured Signals

The analysis here is done with the adapted EKF which has all the VAs of up to second order in its state vector and without the discovery. Running the tracking system this way allows to correct the precomputed VA positions using the measurements. The VA positions might be erroneous due to an imprecise floor plan or errors in the position of the anchors. The results are then compared to the results of the offline re-localization which was done together with the offline variance estimation.

Fig. 4.19 shows the results of the comparison for both trajectories for some selected VAs. It shows the difference of the re-localized VA position to the ideal VA position in the x and y direction for both the online (Δx_{on} and Δy_{on}) and offline (Δx_{off} and Δy_{off}) method. In most cases the results are comparable but for example A1 and VA 19 of trajectory 2 differ a lot from the offline results. In these plots, the value of the online position error is computed using the re-localized VA position at the last trajectory point. As the plots in Fig. 4.20 and Fig. 4.21 show, the position error changes over time especially at the beginning of the tracking. Except for Δx_{on} of A1 on trajectory 2, all errors seem to become stable towards the end of the tracking.

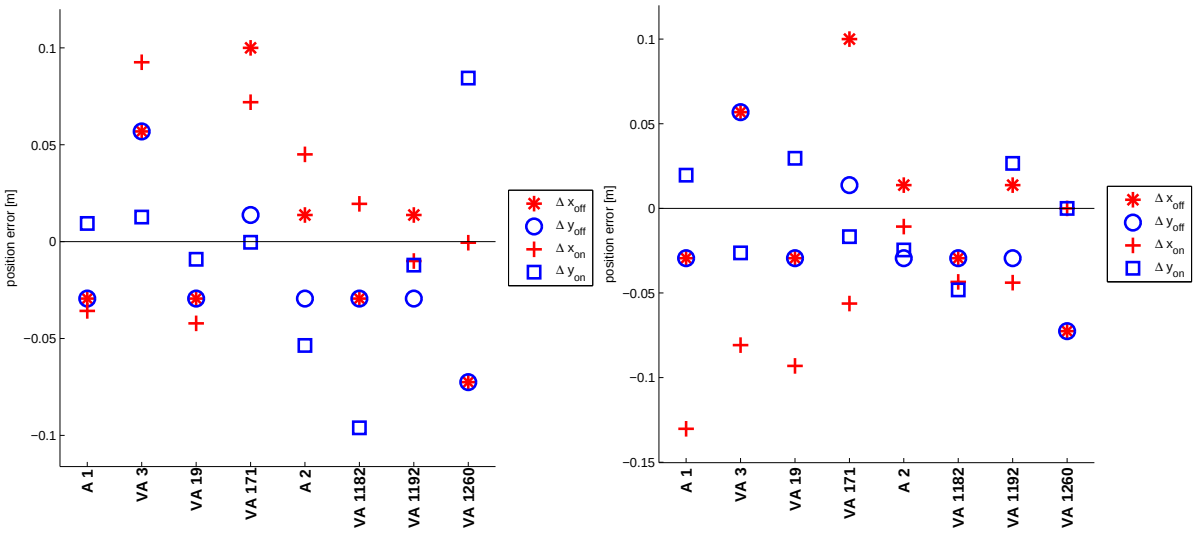

(a) Position error trajectory 1 (b) Position error trajectory 2

Figure 4.19: Comparison of the re-localization between offline (Δx_{off} and Δy_{off}) and online (Δx_{on} and Δy_{on}) method for both trajectories in the seminar room. Pulse shaping parameters are $f_c = 7\,GHz$, $\beta_R = 0.5$ and $T_p = 0.5\,ns$

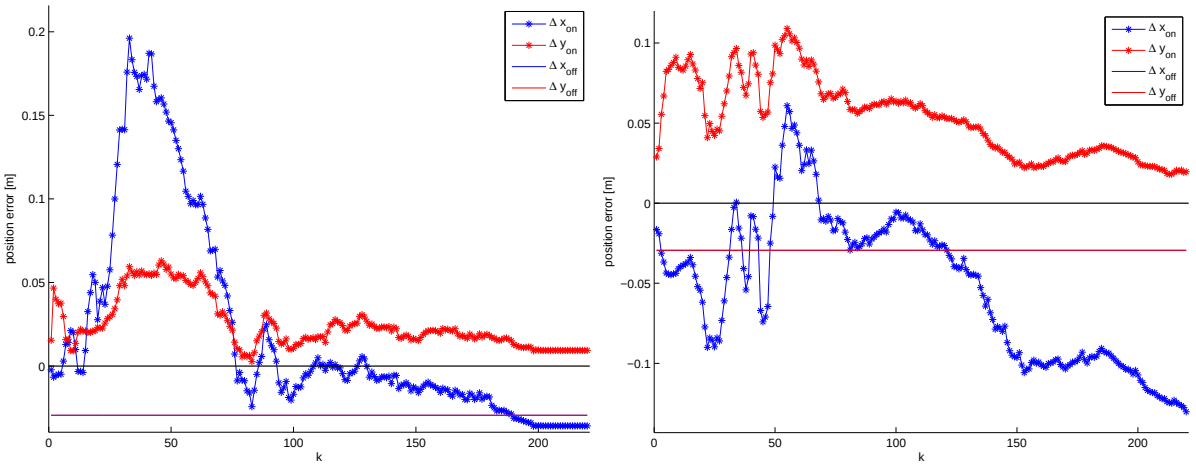

(a) Position error trajectory 1 (b) Position error trajectory 2

Figure 4.20: Evolution of the position error of A1 (Δx_{off} is not visible because it is hidden by Δy_{off} as they have similar values)

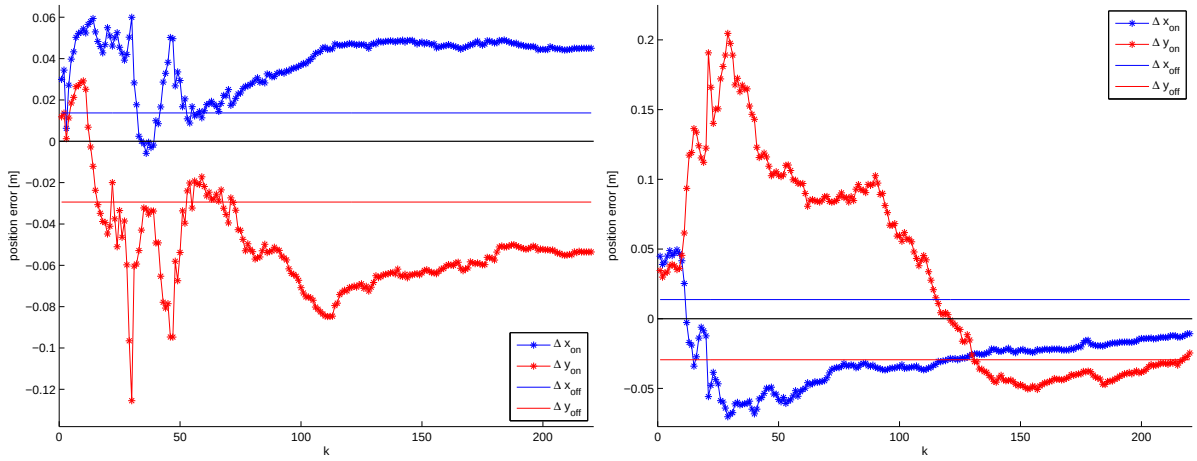

(a) Position error trajectory 1

(b) Position error trajectory 2

Figure 4.21: Evolution of the position error of A2

4.4.2 Simulation Results using Synthetic Signals

For the simulations in this section, the parameters as presented in Tab. 4.2 are used. Only first order VAs are initially known. The VAs associated to the wall segments which are highlighted in red in the tracking plots were assumed to be unknown. In the tracking plots, only the initially unknown VAs are shown as the plot would be congested if all VAs were plotted.

Parameter	Value
Discrete time step Δt	0.3 s
Maximum velocity v_{max}	0.9 m/s
Measurement noise variance σ_z^2	0.02 m^2
cut-off distance d_c	0.2 m
Initial mobile position variance σ_i^2	0.01 m^2
Highest VA Order of known VAs	1
Number of measurement to create a VA candidate pair	3
Minimum number of measurements to initialize a new VA	10
RLS initial error variance	10
RLS measurement variance R_z	0.04
Center frequency f_c	7 GHz
Roll-off factor β_R	0.5
Pulse duration T_p	0.5 ns
Maximum number of extracted MPCs K	20

Table 4.2: Parameters of the simulations in the seminar room

Fig. 4.22 shows the first simulation. Here, only first order deterministic MPCs were considered for the synthetic signals. The error ellipses are enlarged by a factor of 3 and shown for every 20-th time step. The minor axis of it is in most cases directed towards the anchors which means that more information comes from their direction and less from the direction of the major axis. The tracking CDF can be seen in Fig. 4.23(a).

There were two VAs discovered, one for each anchor. VA 2396 for A2 was very accurate while VA 2395 for A1 is 0.5 m away from its ideal position. It can be seen in the detail view of the VA in Fig. 4.23(b) that the tracker corrects the VA towards the unknown VA 7 but the tracker is not able to reduce the error of this VA due to two reasons. Firstly, the VA is not visible long enough because of the many small wall segments in this room. As the results in the L room showed, many time step are necessary to correct large initialization errors. Secondly, it can be seen that the final position of VA 2395 is approximately 0.5 m below its initial position and that between those two a large jump happens as there are no blue markers indicating the movement of the VA. Here the problem of the wrong data association due to the lack of the visibility lookup for discovered VAs becomes obvious. The VA has not been associated for some time steps and at some point a range measurement comes in which is just in the cut-off distance although the VA is not visible from the agents current position. Due to the wrong association and the quite large error of the range measurement the next position correction according to the tracker lets the VA jump to the position as shown in the plot.

For the next simulation, the same set of known VAs but a different trajectory and synthetic signals containing up to second order MPCs were used. The simulation result of the tracking is shown in Fig. 4.24. Unknown VAs of second order are plotted only in the vicinity of discovered VAs otherwise the plot would be cluttered as there are 331 second order VAs in this room. All discovered VAs except for VA 2395 have multiple VAs in their vicinity. To analyze which VA

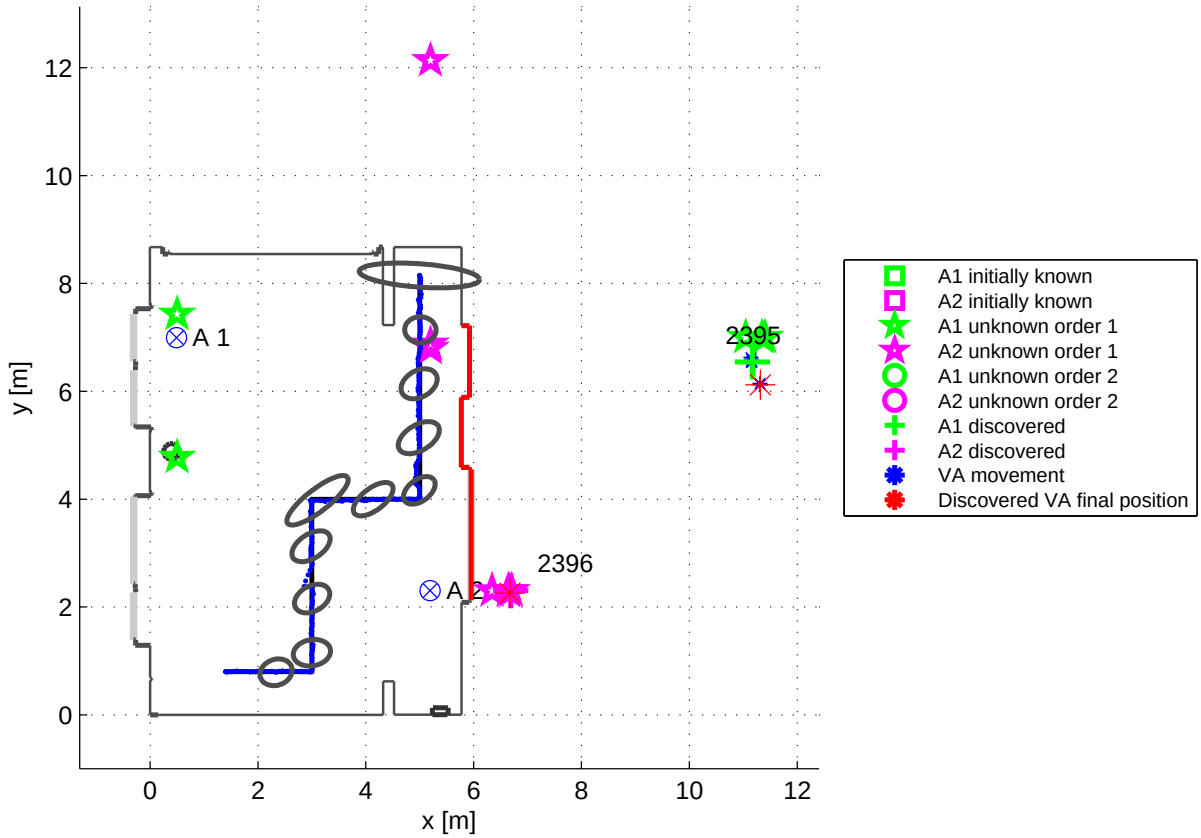

Figure 4.22: Tracking and VA discovery in seminar room using the first trajectory with synthetic signals of order one, all first order VAs except those associated to the red wall segments are initially known. The error ellipses are plotted for every 20-th time step and enlarged by a factor of 3. Pulse shaping parameters: $f_c = 7\,GHz$, $\beta_R = 0.5$ and $T_p = 0.5\,ns$

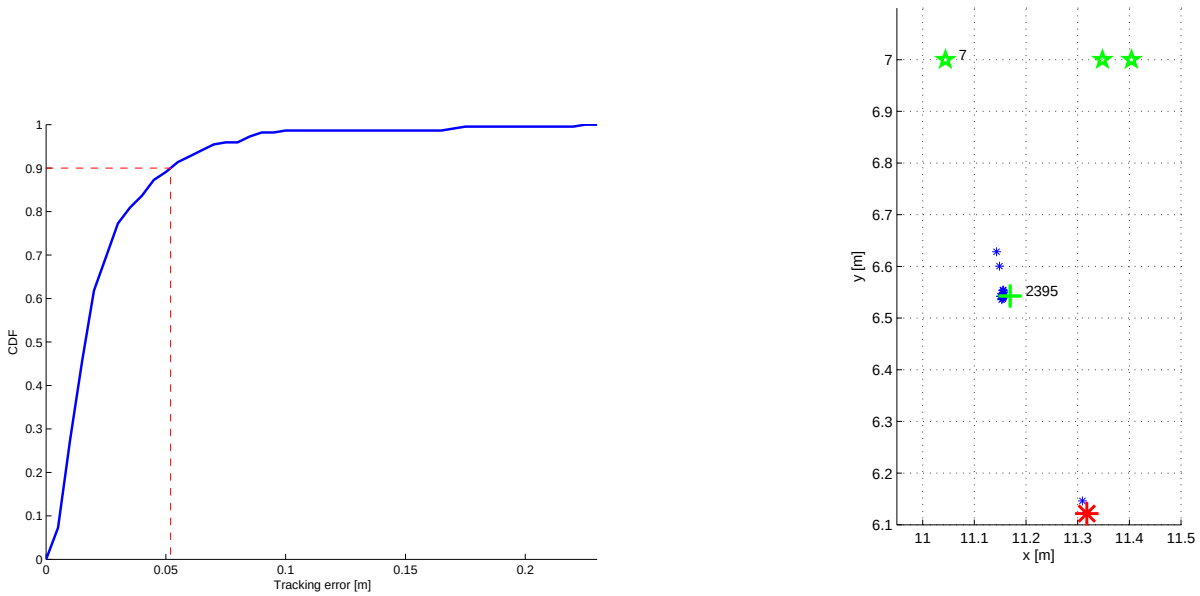

(a) CDF of the tracking

(b) Detail view of discovered VA 2395

Figure 4.23: CDF and detail view of VA 2395 of tracking in Fig. 4.22

for example the discovered VA 2396 describes, the visibility regions of four VAs towards which the discovered VA corrects its position are examined. All four target ideal VAs are within 2 cm. Due to the visibility regions, only a single VA can be identified (see Fig. 4.25(a)) to be the target VA as two VAs are not visible along the trajectory and one only on a quite short, straight part of it which makes it impossible for it to be identified (Fig. 4.25(b)).

VA 2395 was discovered away from its ideal position because the agent position for the initialization of the VA candidate pair was poorly tracked and therefore both candidates are far away from their ideal position and none of them is able to correct this error. Furthermore, the wrong VA candidate was chosen due to the poor initialization and it moves away from its ideal position.

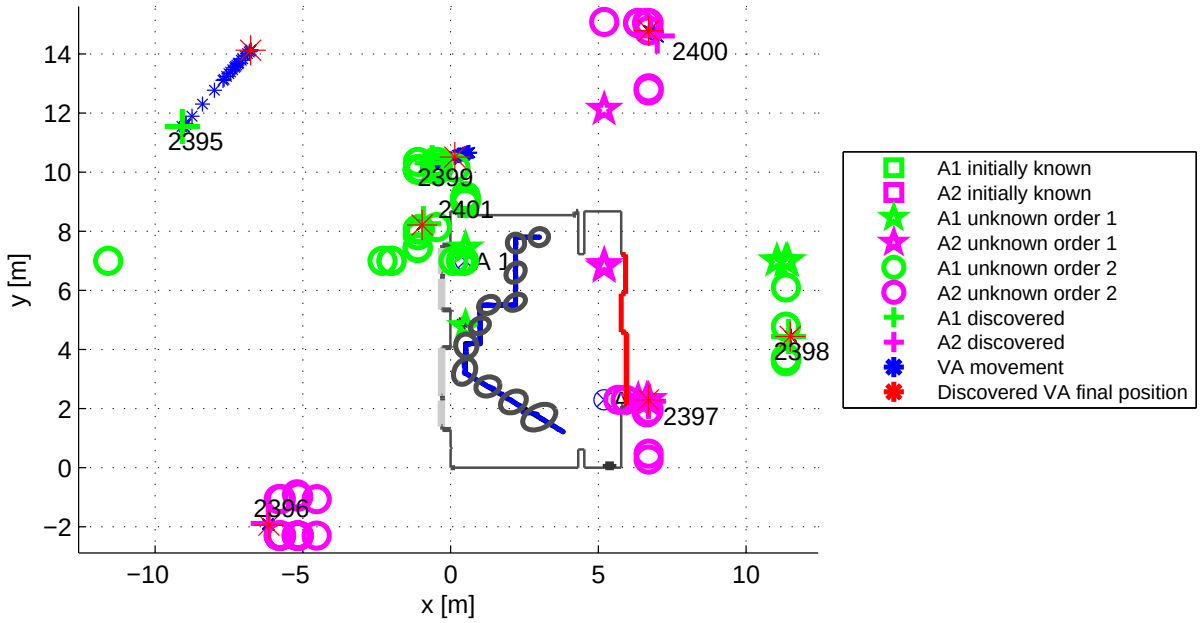

Figure 4.24: Tracking and VA discovery in seminar room using the second trajectory with synthetic signals with MPCs of up to order two, all first order VAs except those associated to the red wall segments are initially known. The error ellipses are plotted for every 20-th time step and enlarged by a factor of 3. Pulse shaping parameters: $f_c = 7\,GHz$, $\beta_R = 0.5$ and $T_p = 0.5\,ns$

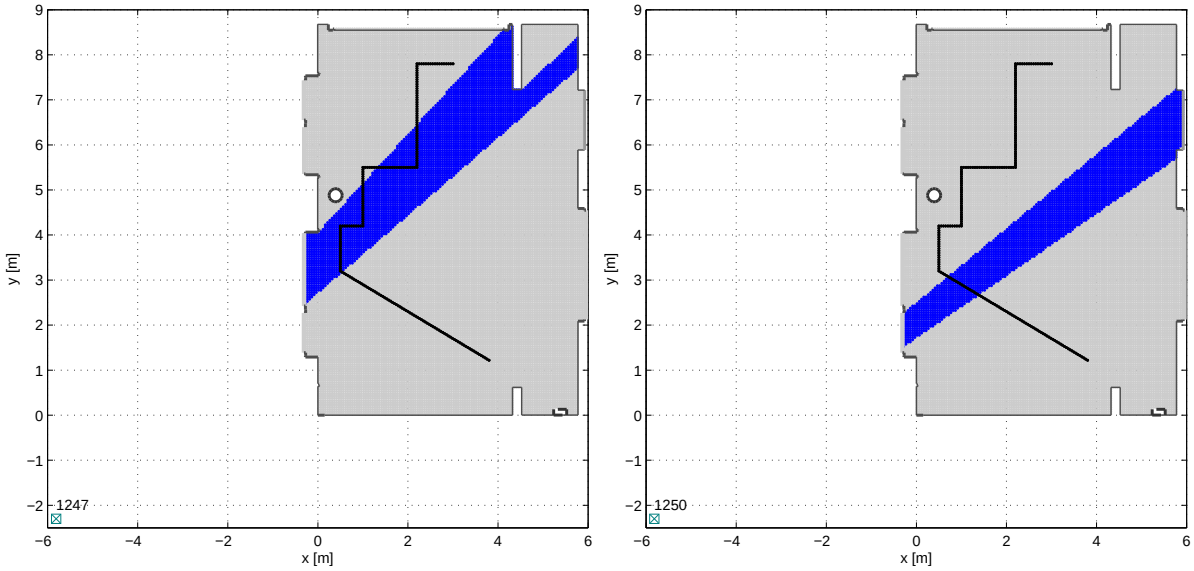

(a) Visibility region of VA 1247

(b) Visibility region of VA 1250

Figure 4.25: Visibility regions of possible target VAs for discovered VA 2396

4.4.3 Tracking Results using Measured Signals

For the analysis in this section, signals measured with the M-Sequence channel sounder along the main points of the trajectories are used. As the simulation results in Section 3.7 showed, the tracking without the variance estimation is not very robust, therefore the simulations in this section are all done using online variance estimation for the VAs. Furthermore, the variance estimation is necessary to reduce the influence of erroneously discovered VAs. As the results will show, they are influenced by diffuse multipath and will have strongly varying amplitudes. Therefore, the estimated variance will be higher compared to initially known or correctly discovered VAs and not influence the tracking too much.

As the measured signal contains more MPCs than the used synthetic signals in the previous section, the number of discovered VAs will be higher. Therefore, only some VAs are plotted otherwise the result plots would be too congested. Also, the plots will not contain any initially known VAs for the same reason. In the following analysis, the performance of the tracker with and without VA discovery is evaluated to see the influence of the additionally available VAs. The parameters of the simulation are the same as in Tab. 3.1 and Tab. 3.2.

All VAs of First Order Initially Known

Initially, all VAs of first order are known, Tab. 4.3 shows how many VAs are initially known and how many were discovered along the two trajectories.

Fig. 4.26 shows the tracking and VA discovery along trajectory 1. The tracking works fine, there is a situation at the end of the trajectory in the geometrically difficult region where the tracker moves through a wall. Actually, movement through a wall is detected by checking whether the tracker is still in the room or not, but this simple check fails as the tracker jumps through the wall and is back in the room again. As a more sophisticated check is not implemented, this situation could not be handled, but it does not affect the tracking and VA discovery much as it happens at the very end of the trajectory. The discovery found 27 VAs for anchor 1 and 31 for anchor 2.

	Anchor 1	Anchor 2
Initially known	43	50
Discovered Trajectory 1	27	31
Discovered Trajectory 2	31	30

Table 4.3: Number of initially known VAs and discovered VAs for the different trajectories for the tracking in Fig. 4.26 (trajectory 1) and Fig. 4.30 (trajectory 2)

The CDFs in Fig. 4.27 show a comparison between the tracking performance with and without the VA discovery. It can be seen that the performance with VA discovery is slightly better because more VAs are available. The two things that could degrade the tracking performance are poorly discovered VAs and the association of measurements with VAs although they are not visible from the current mobile position as described. As the CDF shows, those problems are not severe because for each VA the variance is estimated using the SINR. If one of the previous mentioned situations comes up, the variance will be high as estimated amplitudes will vary strongly and therefore the VA will not influence the tracking significantly.

This can be see in Fig. 4.28 and Fig. 4.29 which show the evolution of the standard deviation for different VAs over the discrete time steps. Those plots also show the standard deviation of the anchor and one reliable VA for comparison. A standard deviation of 0 indicates that the VA was not known in the respective time steps, i.e. if it was discovered, the standard deviation jumps from 0 to the computed value. By visual observation of the discovered VAs of anchor 1 in Fig. 4.26, VA 2434, 2423 and 2429 are supposed to be well discovered and will increase the tracking accuracy while VA 2414 will not have a large influence. As the evolution of the standard deviation in Fig. 4.28 shows, it is true that VA 2423 and VA 2434 have a comparably small standard deviation. VA 2429 has a high standard deviation which means that it is near some ideal VAs by coincidence. As expected, VA 2414 has a high standard deviation.

Similar results can be seen in Fig. 4.29 for the second anchor. For example, VA 2435 is discovered very well within some centimeters of its ideal position but the VA tracking corrects it away from its ideal position. This can also be seen in the standard deviation as it is low after initialization but increases afterwards.

The same analysis was done using trajectory 2. The tracking is shown in Fig. 4.30, the CDFs with and without VA discovery in Fig. 4.31 and the evolution of the standard deviation for anchor 1 and 2 in Fig. 4.32 and Fig. 4.33, respectively. There were 31 VAs discovered for anchor 1 and 30 for anchor 2.

The CDFs show that the tracking performance does not change significantly and the evolution of the standard deviation leads to the same results as in the previous case using trajectory 1. The result can be compared with the tracking results in Fig. 3.13 and the CDFs in Fig. 3.14 where the VAs have not been tracked.

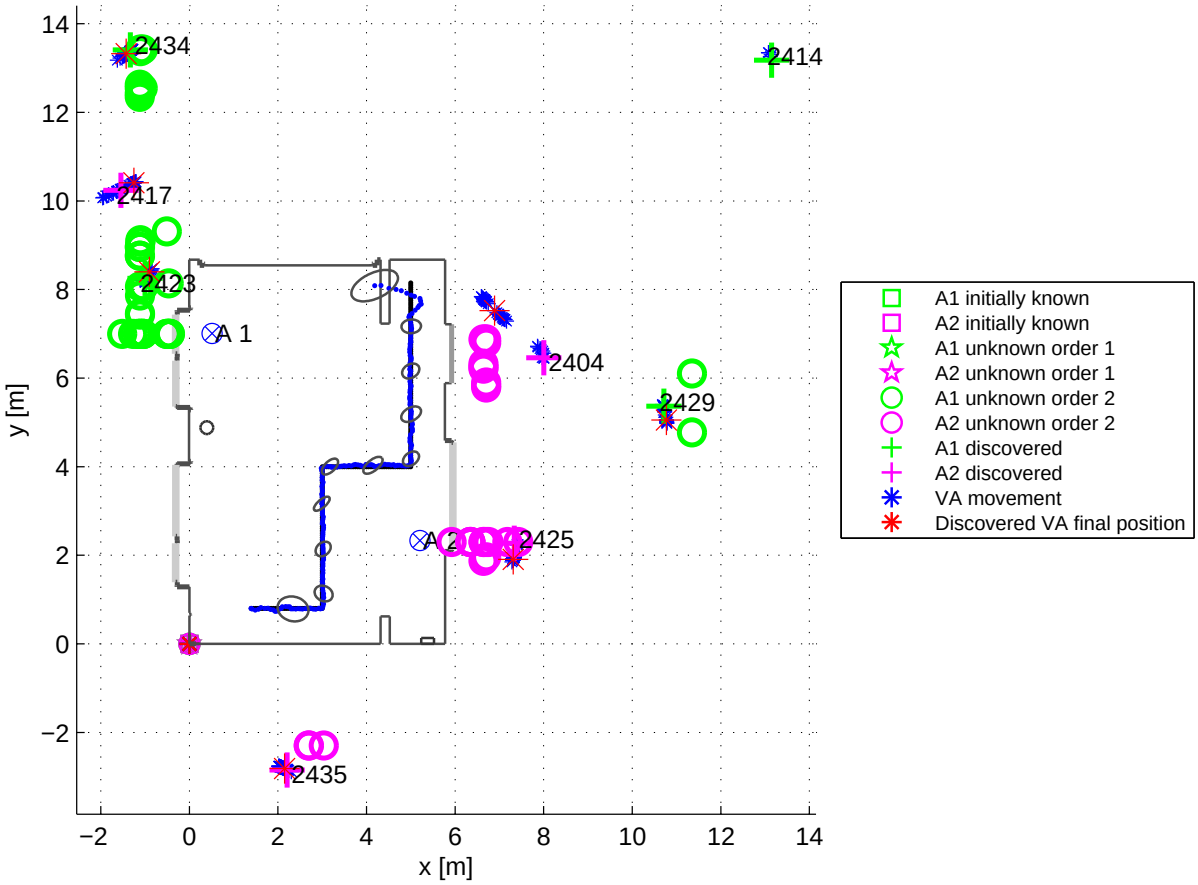

Figure 4.26: Tracking and VA discovery in seminar room using the first trajectory with measured signals, all first order VAs are initially known. The error ellipses are plotted for every 20-th time step and enlarged by a factor of 20. Pulse shaping parameters: $f_c = 7\,GHz$, $\beta_R = 0.5$ and $T_p = 0.5\,ns$

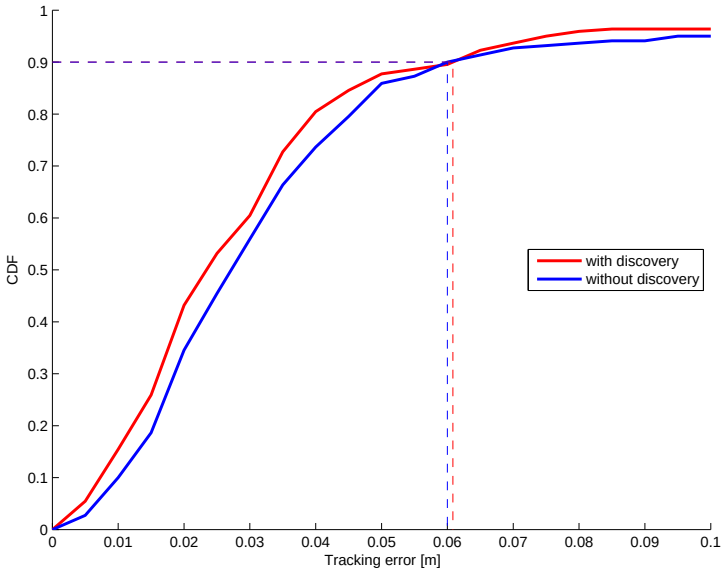

Figure 4.27: CDF of tracking without VA discovery and with VA discovery as shown in Fig. 4.26 averaged over 25 runs

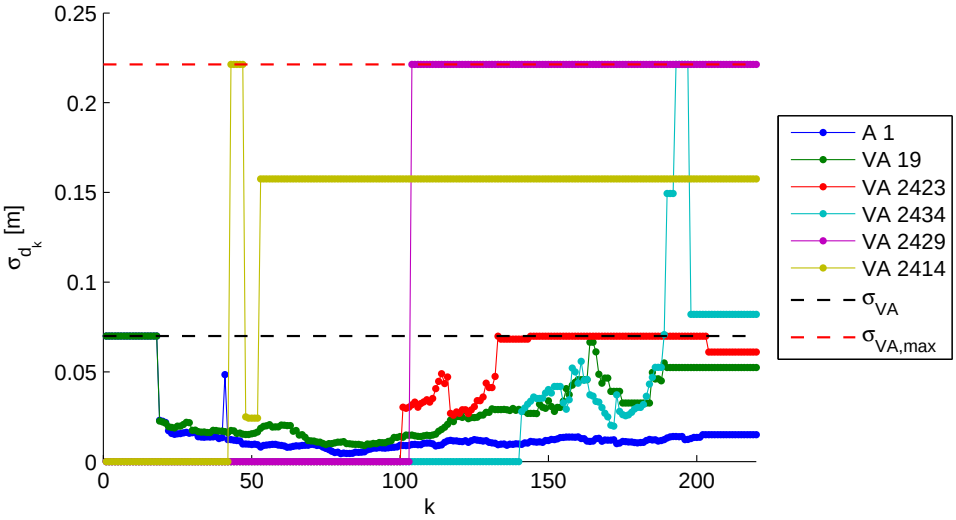

Figure 4.28: Evolution of the estimated standard deviation of the VA positions of anchor 1 for trajectory 1 (Fig. 4.26) over discrete time steps k. For comparison with the discovered VAs, the anchor (A1) the initially known VA 19 are plotted as well. Default standard deviation $\sigma_{\mathrm{VA}} = 0.07\,m$, standard deviation if SINR is zero or complex $\sigma_{\mathrm{VA,max}} = 0.22\,m$

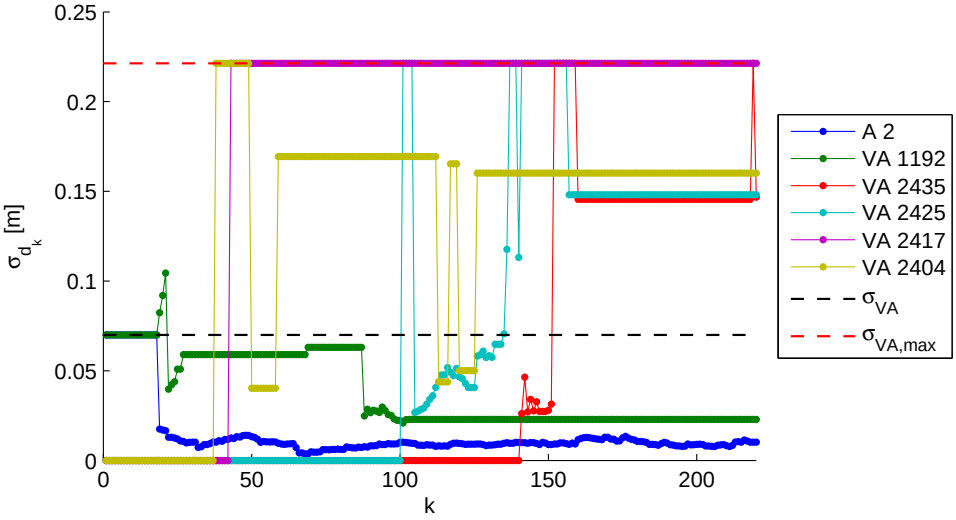

Figure 4.29: Evolution of the estimated standard deviation of the VA positions of anchor 2 for trajectory 1 (Fig. 4.26) over discrete time steps k. For comparison with the discovered VAs, the anchor (A2) the initially known VA 1192 are plotted as well. Default standard deviation $\sigma_{\mathrm{VA}} = 0.07\,m$, standard deviation if SINR is zero or complex is $\sigma_{\mathrm{VA,max}} = 0.22\,m$

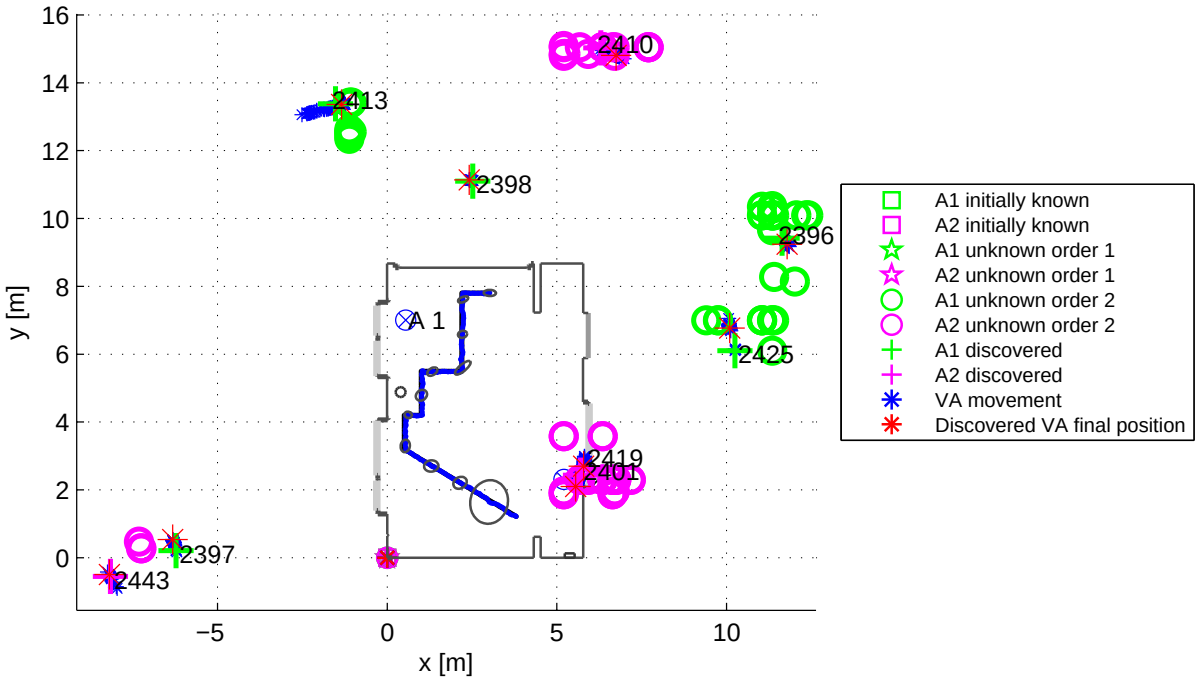

Figure 4.30: Tracking and VA discovery in seminar room using the second trajectory with measured signals, all first order VAs are initially known. The error ellipses are plotted for every 20-th time step and enlarged by a factor of 20. Pulse shaping parameters: $f_c = 7\,GHz$, $\beta_R = 0.5$ and $T_p = 0.5\,ns$

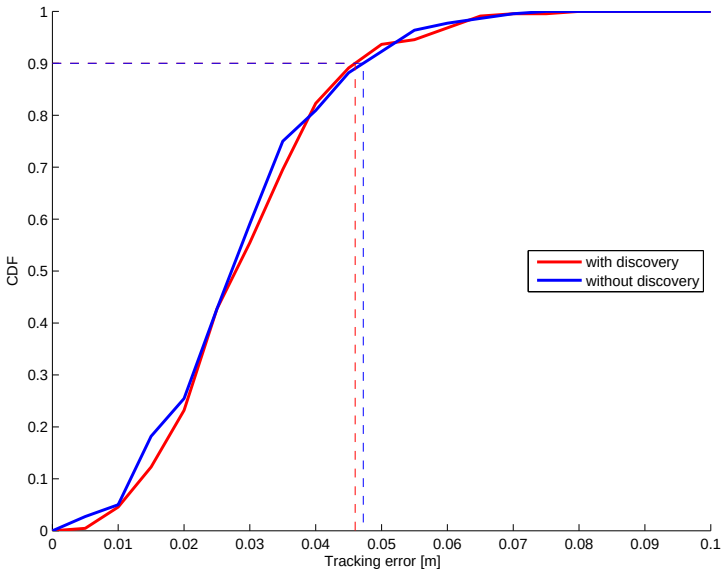

Figure 4.31: CDF of tracking without VA discovery and with VA discovery as shown in Fig. 4.30 averaged over 25 runs

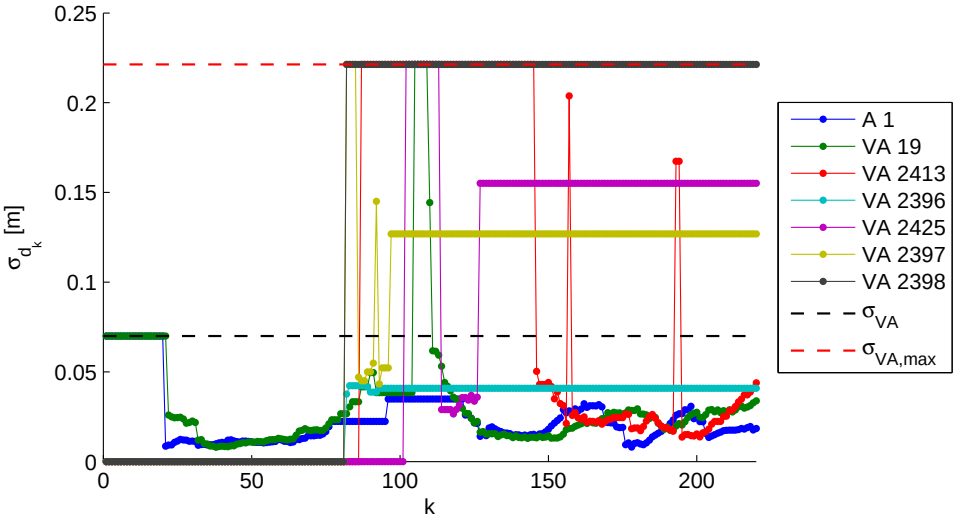

Figure 4.32: Evolution of the estimated standard deviation of the VA positions of anchor 1 for trajectory 2 (Fig. 4.30) over discrete time steps k. For comparison with the discovered VAs, the anchor A1 and the initially known VA 19 are plotted as well. Default standard deviation $\sigma_{\mathrm{VA}} = 0.07\,m$, standard deviation if SINR is zero or complex $\sigma_{\mathrm{VA,max}} = 0.22\,m$

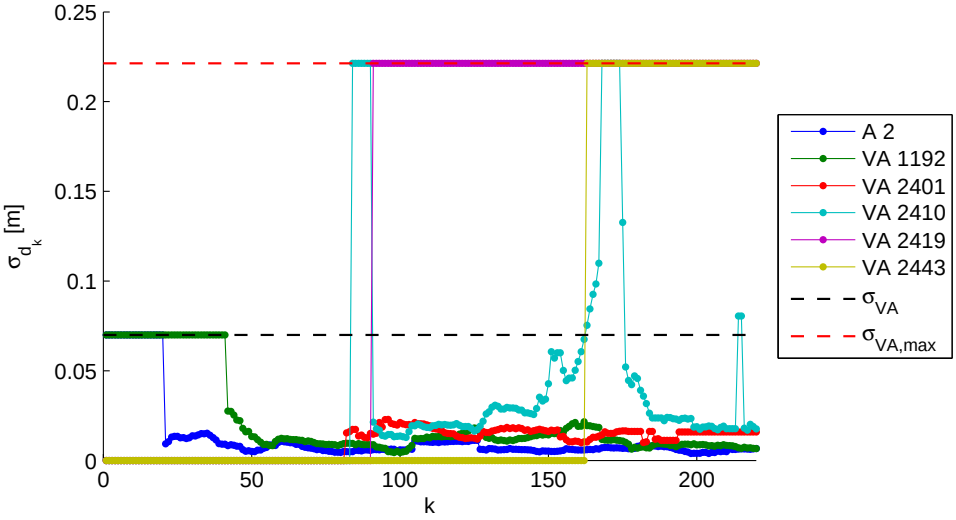

Figure 4.33: Evolution of the estimated standard deviation of the VA positions of anchor 2 for trajectory 2 (Fig. 4.30) over discrete time steps k. For comparison with the discovered VAs, the anchor A2 and the initially known VA 1192 are plotted as well. Default standard deviation $\sigma_{\mathrm{VA}} = 0.07\,m$, standard deviation if SINR is zero or complex is $\sigma_{\mathrm{VA,max}} = 0.22\,m$

Reduced Set of Initially Known VAs

To further show the capability of the system, the same simulations were done using only a small set of known wall segments as shown in Fig. 4.34. All initially known VAs are shown in Tab. 4.4, those are all first order VAs associated to the known wall segments. Those wall segments were chosen as they have a large visibility region and would be comparably easy to measure if the floor plan has to be created from scratch.

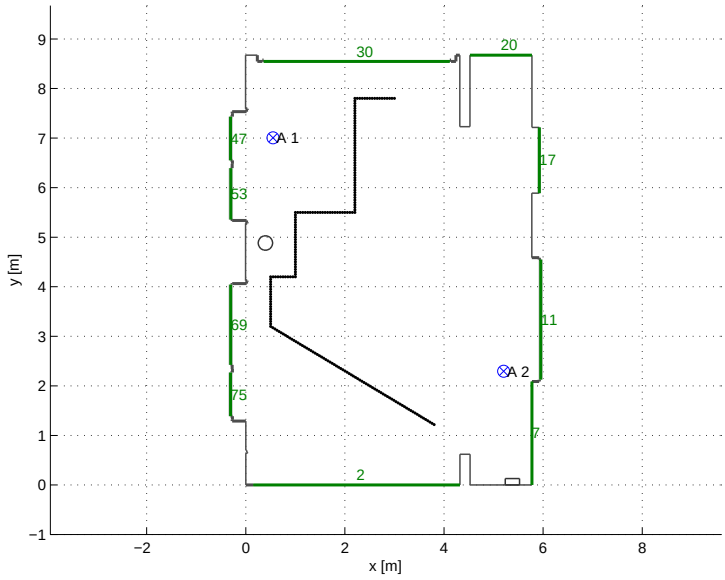

Figure 4.34: Floor plan showing with known wall segments highlighted in green

Wall #	Anchor 1		Anchor 2	
	VA #	Position	VA #	Position
2	3	(0.500/-7.000)	1174	(5.200/-2.300)
7	7	(11.050/7.000)	1178	(6.350/2.300)
11	11	(11.404/7.000)	1182	(6.704/2.300)
17	14	(11.348/7.000)	1186	(6.648/2.300)
20			1189	(5.200/15.048)
30	19	(0.500/10.094)	1192	(5.200/14.794)
47	32	(-1.116/7.000)	1203	(-5.816/2.300)
53	34	(-1.106/7.000)	1205	(-5.806/2.300)
69			1214	(-5.810/2.300)
75	42	(-1.118/7.000)	1216	(-5.818/2.300)

Table 4.4: Used wall segments and the resulting first order VAs for each anchor.

The following plots show the same analysis as before. For both trajectories the tracking performance is increased because of the increased number of VAs available for tracking. This is shown by the CDFs in Fig. 4.36 and Fig. 4.40. Tab. 4.5 shows how many VAs were discovered for each trajectory. It shows that about three times as many VAs were discovered as were initially known. Although many of them are at a wrong position due to the influence of the diffuse multipath, it does not degrade the tracking performance as only reliable VAs with a low variance add information. Furthermore, it shows that the problem of the missing VA visibilities

for discovered VAs is not problematic, again due to the variance estimation.

	Anchor 1	Anchor 2
Initially known	9	11
Discovered Trajectory 1	25	35
Discovered Trajectory 2	32	29

Table 4.5: Number of initially known VAs and discovered VAs for the different trajectories for the tracking in Fig. 4.35 (trajectory 1) and Fig. 4.39 (trajectory 2)

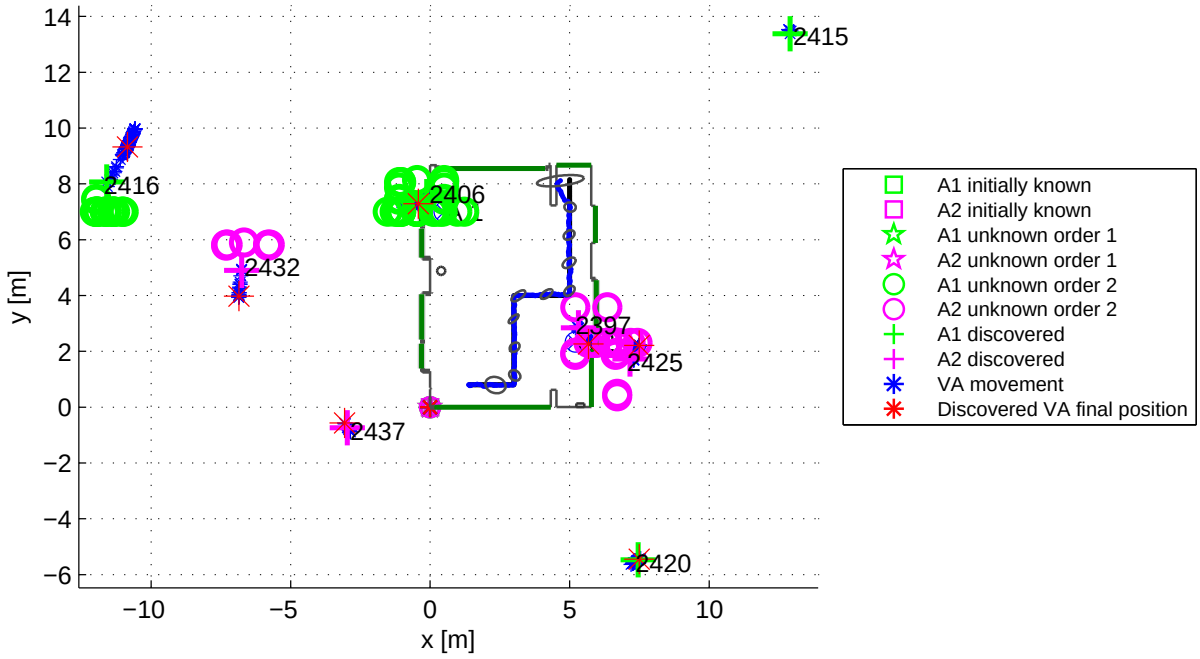

Figure 4.35: Tracking and VA discovery in seminar room using the first trajectory with measured signals, all first order VAs associated to the green walls (see Tab. 4.4) are initially known. The error ellipses are plotted for every 20-th time step and enlarged by a factor of 20. Pulse shaping parameters: $f_c = 7\ GHz$, $\beta_R = 0.5$ and $T_p = 0.5\ ns$

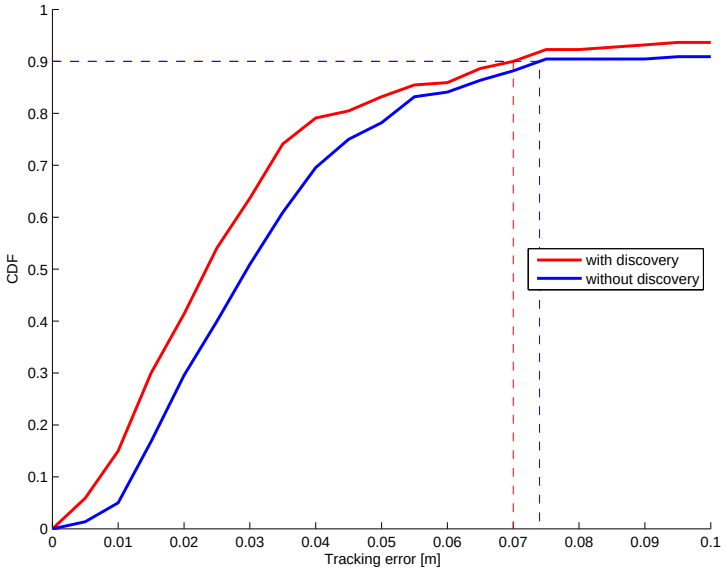

Figure 4.36: CDF of tracking without VA discovery and with VA discovery as shown in Fig. 4.35 averaged over 25 runs

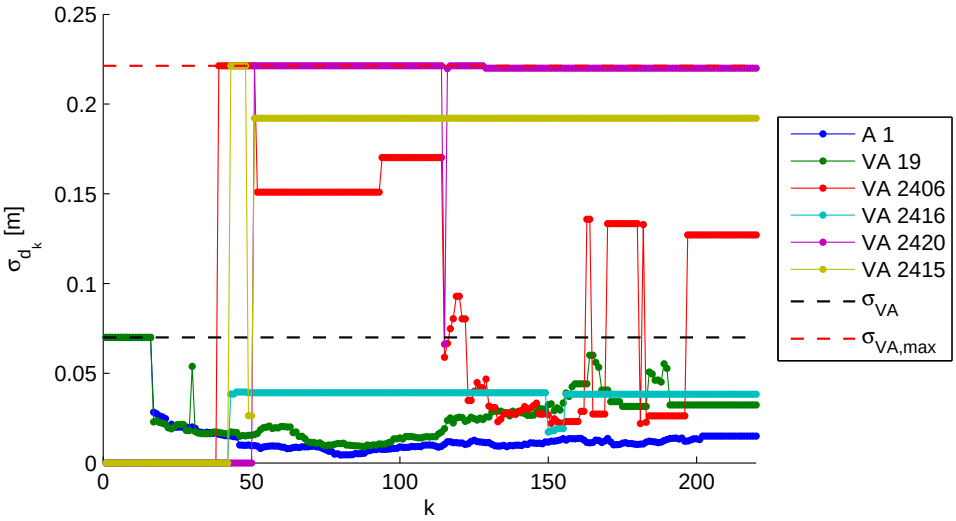

Figure 4.37: Evolution of the estimated standard deviation of the VA positions of anchor 1 for trajectory 1 (Fig. 4.35) over discrete time steps k. For comparison with the discovered VAs, the anchor A1 and the initially known VA 19 are plotted as well. Default standard deviation $\sigma_{\mathrm{VA}} = 0.07\,m$, standard deviation if SINR is zero or complex $\sigma_{\mathrm{VA,max}} = 0.22\,m$

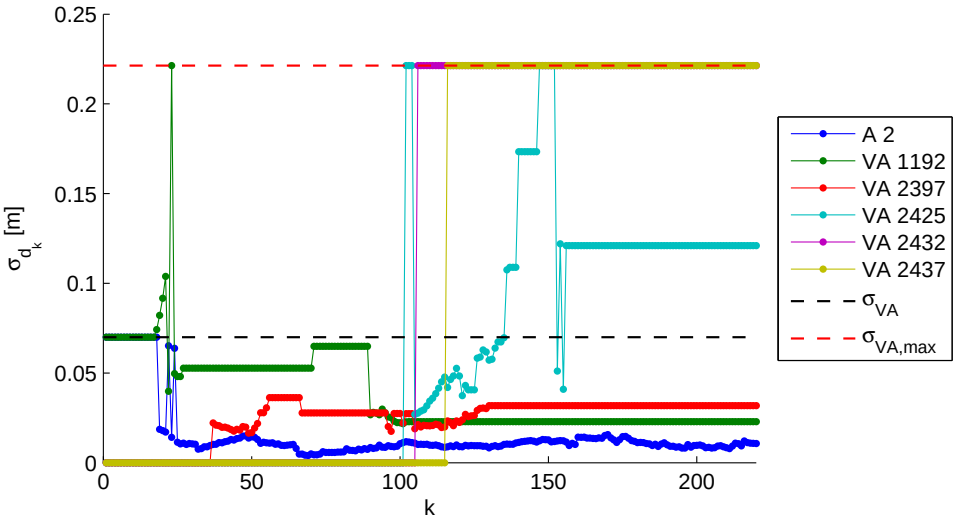

Figure 4.38: Evolution of the estimated standard deviation of the VA positions of anchor 2 for trajectory 1 (Fig. 4.35) over discrete time steps k. For comparison with the discovered VAs, the anchor A2 and the initially known VA 1192 are plotted as well. Default standard deviation $\sigma_{\mathrm{VA}} = 0.07\,m$, standard deviation if SINR is zero or complex is $\sigma_{\mathrm{VA,max}} = 0.22\,m$

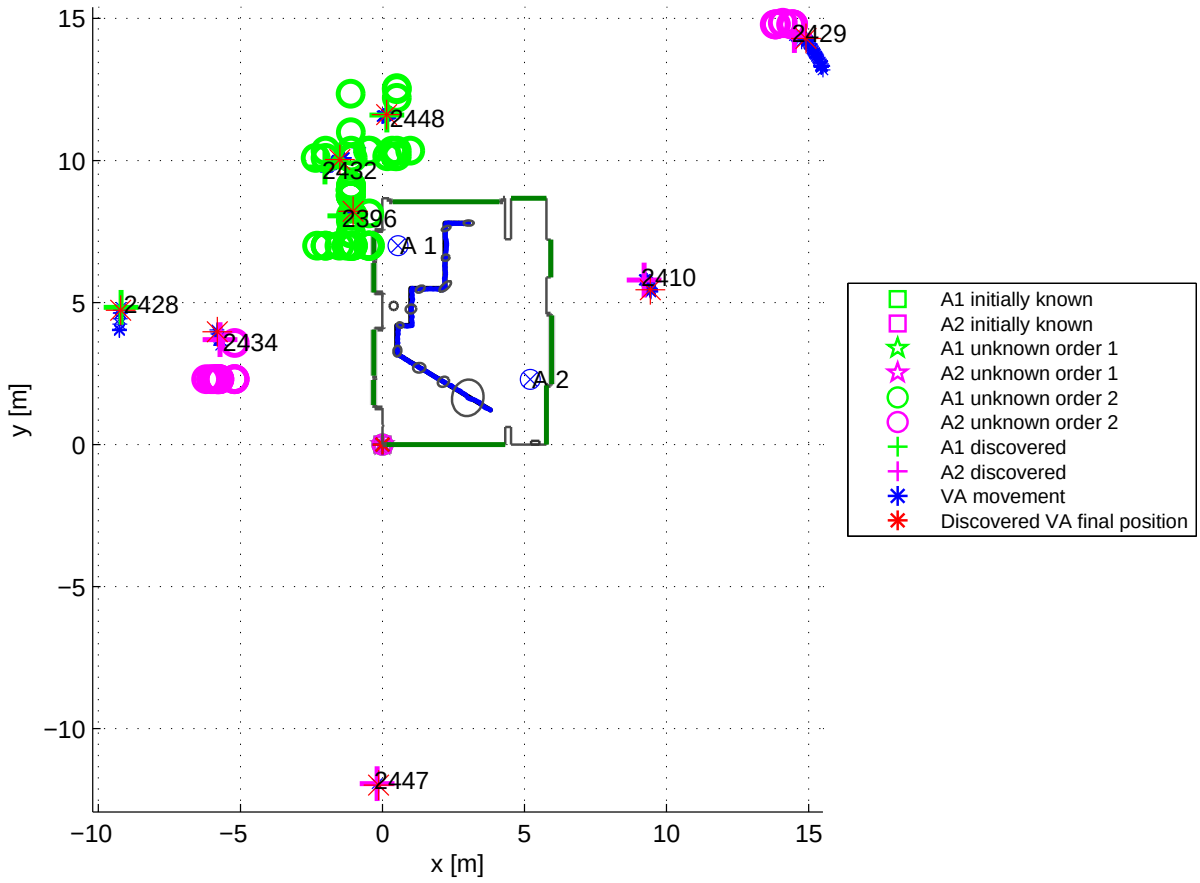

Figure 4.39: Tracking and VA discovery in seminar room using the second trajectory with measured signals, all first order VAs associated to the green walls (see Tab. 4.4) are initially known. The error ellipses are plotted for every 20-th time step and enlarged by a factor of 20. Pulse shaping parameters: $f_c = 7\,GHz$, $\beta_R = 0.5$ and $T_p = 0.5\,ns$

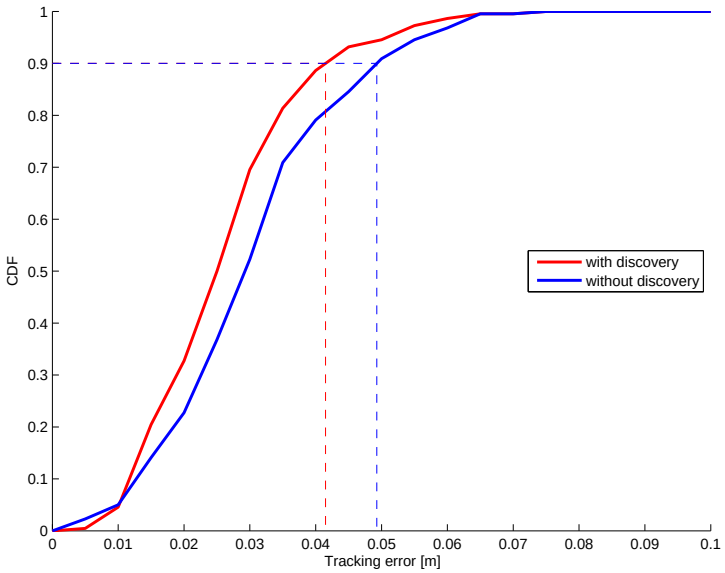

Figure 4.40: CDF of tracking without VA discovery and with VA discovery as shown in Fig. 4.39 averaged over 25 runs

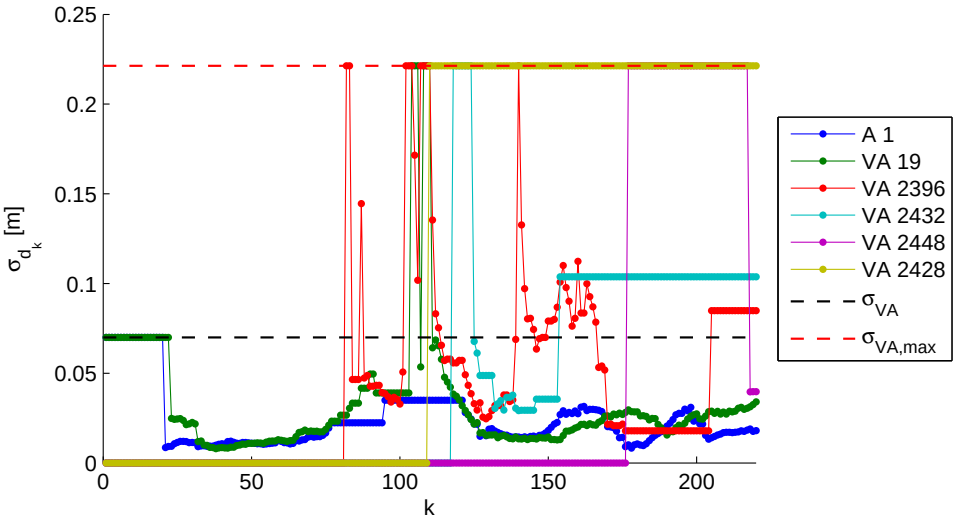

Figure 4.41: Evolution of the estimated standard deviation of the VA positions of anchor 1 for trajectory 2 (Fig. 4.39) over discrete time steps k. For comparison with the discovered VAs, the anchor A1 and the initially known VA 19 are plotted as well. Default standard deviation $\sigma_{\mathrm{VA}} = 0.07\,m$, standard deviation if SINR is zero or complex $\sigma_{\mathrm{VA,max}} = 0.22\,m$

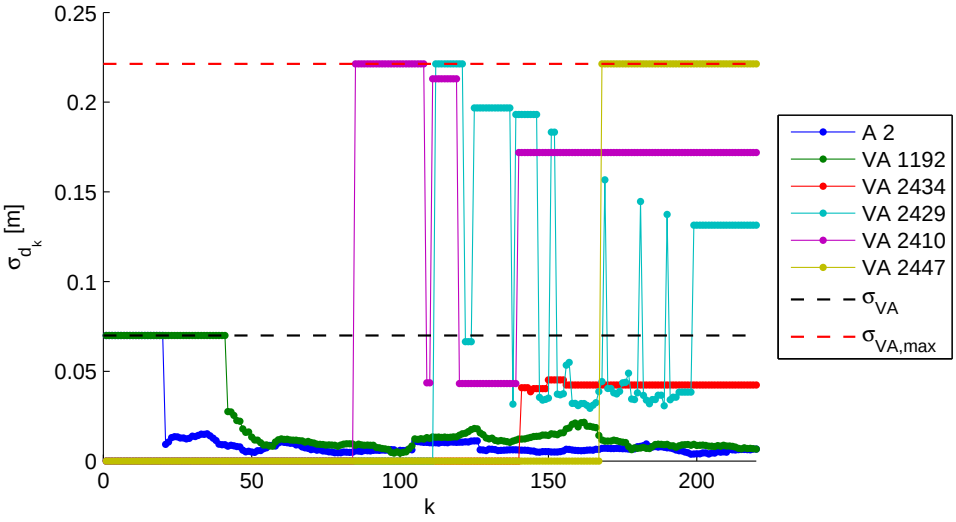

Figure 4.42: Evolution of the estimated standard deviation of the VA positions of anchor 2 for trajectory 2 (Fig. 4.39) over discrete time steps k. For comparison with the discovered VAs, the anchor A2 and the initially known VA 1192 are plotted as well. Default standard deviation $\sigma_{\mathrm{VA}} = 0.07\,m$*, standard deviation if SINR is zero or complex is* $\sigma_{\mathrm{VA,max}} = 0.22\,m$

5 Conclusion and Future Work

5.1 Conclusion

Based on the theoretical work and the off-line implementation of the MINT system using an EKF, the first part of this thesis has shown that a real-time implementation of the MINT system using a M-Sequence correlative channel sounder is feasible. The number of measurements per second was only limited by the channel sounder and not by the algorithms used. The robustness and accuracy of the system were increased by an online estimation of the position error of the associated VAs.

The MINT implementation was extended to also take the VAs into account in the tracking. This makes it possible to correct erroneous VA positions using the measurements (online re-localization). The evolution of the VA position error over time shows that the error converges. Comparisons were performed with the offline results, showing that in some cases the results are comparable.

A further extension of the system allowed to estimate the position of unknown VAs using only the measured ranges extracted from the signals. The error correction capability of the system (online re-localization) allows in many situations to reduce the error of discovered VAs and they converge towards their ideal positions. Diffuse multipath leads to erroneously estimated VAs which cannot be corrected. To mitigate the influence of those VAs, an online estimation method for the MPC reliability was implemented. As results using measured signals show, the VA discovery makes the tracking more accurate as more VAs providing ranging information are available and erroneously estimated VAs have no influence. The advantage of the VA discovery becomes more obvious the less VAs are initially known.

To summarize, it can be said that the real-time tracking results and the improvement using variance estimation are very promising. The VA discovery helps the MINT system to increase accuracy and robustness of the tracking even if only a small set of VAs is known.

5.2 Future Work

The next step to improve the VA discovery is to employ some MPC tracking technique, e.g. the KEST algorithm [37], which could reduce the number of falsely extracted delays due to diffuse

multipath. As the simulation results in Section 4.4 showed, diffuse multipath drastically reduces the VA estimation accuracy, even a single extracted delay which stems from diffuse multipath and not the VA can result in an erroneous VA position estimation.

Computing the visibilities of discovered VAs online could also increase the number of associations which bring information to the tracking system. A possible approach could try to compute the visibility only locally around the current position of the mobile and extending the covered visibility region as the mobile moves. However, this requires a mapping of the VA to the walls which is difficult. Furthermore, in scenarios where not all walls are known this is impossible.

To increase the accuracy of the tracking an inertial measurement unit (IMU) can be employed. It can be used to measure the acceleration of the mobile agent which allows to increase the accuracy of its estimated velocity and thus the prediction step in the tracking. As it has been shown, the better the tracking performance the more accurate is the estimated position of discovered VAs.

Future work might also concentrate on the improvement of the resolution of the VA ambiguity. Choosing the wrong VA candidate can drastically reduce the performance of the tracking if the VA is influential. If the tracker drifts off the true trajectory the VA discovery will results in more inaccurate VAs which will further reduce the tracking performance. Multiple Hypothesis Tracking (MHT) could be an interesting approach. For each discovered VA a copy of the tracker with the newly discovered VA added to the state vector is created. The new VA could be accepted as a valid VA if the two tracks to not diverge from each other. Of course, the complexity and the number of hypothesis increases with every discovered VA and the question is whether this approach is suitable for a real-time application.

A

Channel Sounding and the Channel Sounding Device

A.1 Channel Sounding

This overview over channel sounding is based on Chapter 8: Channel Sounding in Wireless Communications [38]. Basically, channel sounding is sending out a signal from a transmitter (TX) which penetrates the channel and is received at the receiver (RX). By comparing transmitted and received signal, the desired channel system function (e.g. the impulse response) can be obtained. The transmit signal $s(t)$ consists of pulses $p(t)$ which are periodically repeated with the repetition interval T_{rep}

$$s(t) = \sum_{i=0}^{N} p(t - iT_{rep}) \tag{A.1}$$

Fig. A.1 shows the block diagram of the channel sounder principle. The transmit pulse $p(t)$ is the convolution of the basis pulse $\tilde{s}(t)$ and the impulse response of the transmit filter $g(t)$

$$p(t) = \tilde{s}(t) * g(t) \tag{A.2}$$

AGC denotes automatic gain control and f_c is the clock frequency. GPS is one of the possible methods for synchronization between TX and RX. The repetition interval T_{rep} is important in time-variant systems, i.e. environments, in which the channel properties change over time, due to movement of TX, RX, interacting objects or any combination of those. As the channel impulse response for any pulse $p(t)$ can be considered a "snapshot" of the channel, T_{rep} must be smaller than the time over which the channel properties change in order to track those changes.

The sounding signal should fulfill some requirements to perform efficient measurements:

- *Large bandwidth*: the bandwidth determines the achievable delay resolution as it is inversely proportional to the shortest temporal change of the sounding signal.
- *Large time bandwidth product*: a time bandwidth product TW larger than unity allows the transmission of higher energy which results in a higher SNR at the receiver. To achieve a

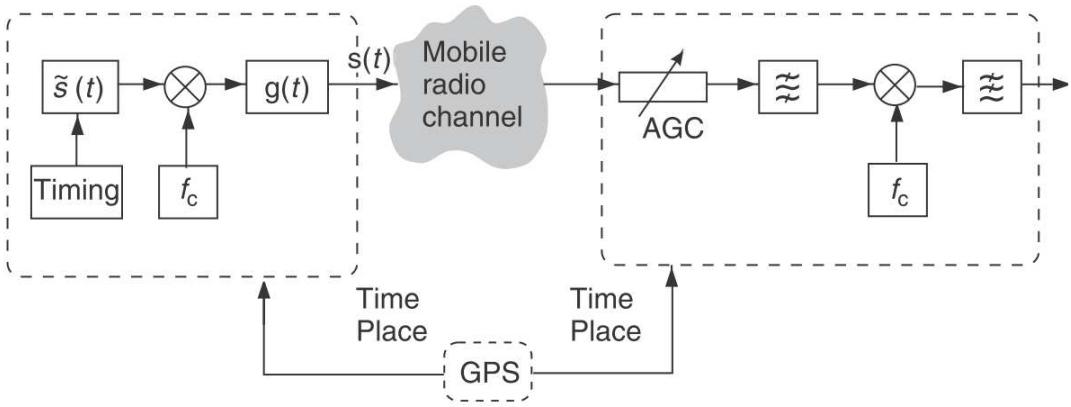

Figure A.1: Principle of the channel sounder [38]

TW greater than unity, the sounding signal has to have a duration longer than the inverse of the bandwidth.

- *Signal duration*: to fulfill the above mentioned TW requirement, the signal duration should be long, but on the other hand it is not allowed to be longer than the time in which the channel is considered approximately constant (coherence time). Therefore the pulse repetition time T_{rep} should be larger than the duration of the pulse $p(t)$ and the maximum excess delay of the channel but smaller than the coherence time.

- *Power-spectral density*: $|P_{TX}(j\omega)|^2$ should be uniform over the bandwidth of interest to ensure the same quality of channel estimation over this bandwidth. Outside the bandwidth of interest, there should be little signal energy for high efficiency.

- *Low crest factor*:

$$C_{crest} = \frac{\text{Peak amplitude}}{\text{rms amplitude}} = \frac{max\{s(t)\}}{\sqrt{\overline{s^2(t)}}} \tag{A.3}$$

  The transmit power amplifier is used efficiently if the signal has a low crest factor.

- *Good correlation properties*: for correlation based measurements, the Autocorrelation Function (ACF) should have a high Peak to Off Peak (POP) ratio and a zero mean (to allow unbiased estimates).

There are two different approaches for channel sounding, the time-domain and the frequency-domain measurement, which are described in the following sections.

A.1.1 Time-domain Measurements

In a time-domain measurement, the impulse response is measured directly by sending out a sequence of pulses. The channel is assumed to be slowly time variant, then the measured impulse response $h_{meas}(\boldsymbol{p}_l, \tau)$ at the position $\boldsymbol{p}_l$ is the convolution of the true channel impulse response $h(\boldsymbol{p}_l, \tau)$ with the impulse response of the sounder $\tilde{p}(\tau)$:

$$h_{meas}(\boldsymbol{p}_l, \tau) = \tilde{p}(\tau) * h(\boldsymbol{p}_l, \tau) \tag{A.4}$$

$\tilde{p}(\tau)$ is the convolution of the transmitted pulse shape $p_{TX}(\tau)$ and the RX filter impulse response $p_{RX}(\tau)$:

$$\tilde{p}(\tau) = p_{TX}(\tau) * p_{RX}(\tau) \tag{A.5}$$

if the channel and the transceiver are linear. To minimize the impact of the measurement system on the result, the sounder impulse response should be as close to a Dirac delta function as possible.

Impulse Sounder

This type of channel sounder sends out a sequence of short pulses $p_{TX}(\tau)$. With shorter pulses a better spatial resolution can be achieved. To get a good SNR the pulses should contain much energy. The receiver filter is a bandpass filter and ideally $p_{RX}(\tau)$ should not have any influence, so that the sounder impulse response becomes:

$$\tilde{p}(\tau) = p_{TX}(\tau) \tag{A.6}$$

As the pulses should contain much energy they have high peak powers. RF components with such requirements are either expensive or have other disadvantages, e.g. non-linearities. Furthermore, impulse sounders have a low resistance to interference, i.e. interfering signals might be interpreted as part of the CIR.

Correlative Sounder

The convolution of $p_{TX}(\tau)$ with $p_{RX}(\tau)$ determines the impact of the measurement system on the observed impulse response. A general relationship between $p_{TX}(\tau)$ and $p_{RX}(\tau)$, which is well known from digital communication theory, is that the SNR at the receiver filter output is maximized, if the receiver filter is matched to the transmit waveform. By concatenation of transmit and receive filter, the sounder impulse response becomes the autocorrelation function (ACF) of the transmit filter if $p_{TX}(\tau) = p_{RX}(\tau)$:

$$\tilde{p}(\tau) = p_{TX}(\tau) * p_{RX}(\tau) = R_{p_{TX}}(\tau) \tag{A.7}$$

Therefore, the sounding pulse should have a high autocorrelation peak $R_{p_{TX}}(0)$ and low ACF sidelobes, which means, it should be a good approximation of a delta function.

The most used sounding sequences in practice are Pseudo Noise (PN) sequences, especially popular are Maximum-length PN sequences (M-Sequences) which can be created by a shift register with feedback. The M-Sequence has an ACF with a periodicity of M_c, has only a single peak of height M_c and a POP ratio of M_c.

In case of time-varying channels, some extra care has to be taken. The basic principle requires, that the channel is the same at the beginning of the PN sequence and at the end of it. If that does not hold, correction procedures are needed.

Swept Time Delay Cross Correlator (STDCC)

The aim of this method is to reduce the sampling rate as a typical correlative sounder has to sample at Nyquist frequency. To reduce the sampling rate, the STDCC uses just one sample value for each m-sequence, taken at the maximum of the ACF. This allows sampling at rate T_{rep}. The time basis of the RX is shifted with respect to the TX for each repetition, so K_{scal}

transmissions of the m-sequence result for a single impulse response $h(\tau_i), i = 1, ..., K_{scal}$ are needed. The advantage of this method is a higher delay resolution and reduced sampling rate, but the time for each measurement is increased by the factor K_{scal}.

A.1.2 Frequency-domain Measurements: Vector Network Analyzer (VNA)

In frequency-domain measurements, the channel transfer function is directly estimated. It is important, that the transmit waveform $p(\tau)$ has a power spectrum $|P(jw)|^2$ that is approximately constant over the bandwidth of interest. One way to transmit the pulses is by sending one frequency at a time, increasing the frequency linearly over a range of frequencies, this is called a sweep. This type of measurement is very slow, therefore it is only usable in static environments as the channel is not allowed to change during one sweep.

A different approach is to send different frequencies at the same time by generating different sinusoidal sounding signals with different weights, phases and frequencies and transmit them simultaneously.

A VNA does a slow sweep over the frequency range of interest. It measures the S-parameters of the device under test (DUT), which can be the wireless channel. The parameter S_{21} is in that case the channel transfer function of the transmitted frequency. Doing a sweep over the whole bandwidth of interest, a sampled version of the transfer function $H(\tau, f)$ is obtained.

As for all kind of channel sounding, a calibration is needed. For VNAs the so called SOLT calibration (Short Open Loss Termination) is used. The frequency response of the VNA itself is measured and in subsequent measurements, the VNA compensates for this frequency response so that only the frequency response of the DUT is measured. Antennas are not taken into account in this type of calibration, but this is not a problem if they are considered to be part of the channel. If some antenna effects have to be taken into account, a separate calibration is needed.

Results of VNAs are usually accurate and straightforward, but there are some things to consider:

- The measurement is slow due to the sweep over the bandwidth of interest, repetition rates cannot exceed a few Hz, therefore the channel is not allowed to change drastically during measurement, which allows VNA measurements mainly in static environments.
- As TX and RX are often in one device, this does limit the distance between TX and RX antenna.

A.1.3 Implementation Issues

Inverse Filtering

It is possible to use a receive filter which is not optimized on the SNR but on the POP ratio. This results in a worse SNR, which is practically unproblematic, but in smaller sidelobes, which is advantageous as they can lead to additional errors.

The receiver filter transfer function for inverse filtering is chosen as $1/P_{TX}(f)$ in the bandwidth of interest, the total transfer function $P_{IF}(f)$ is:

$$P_{IF}(f) = P_{TX}(f) \cdot \frac{1}{P_{TX}(f)} \approx 1 \tag{A.8}$$

The inverse filter compensates for distortions by the transmit filter.

Averaging

Averaging increases the SNR by $10 \cdot log_{10} M$ dB, where M is the number of averaged impulse responses. It is assumed that the channel does not change during the M measurements and that noise is statistically independent.

Synchronization

Synchronization between TX and RX is important in order to establish a common frequency and time basis. This can be quite complicated in wireless channels due to multipath propagation and time variations in the channel. Different approaches are in use:

1. *Synchronization by cables* is possible in indoor environments. For distances of up to 10m, coaxial cables are used, for longer distances fiber-optic cables are needed. For both, the synchronization signal is sent over a known and well-defined medium.

2. The *Global Positioning System (GPS)* can be used in outdoor systems and helps to establish common time and frequency references. Additionally, also the measurement location can be recorded. A disadvantage is that both TX and RX need a line-of-sight connection to GPS satellites.

3. *Rubidium clocks* at TX and RX can be synchronized at the beginning of a measurement, they are extremely stable (typical relative drifts of 10^{-11}) allow synchronization for several hours.

4. *Measurement without synchronization* means doing the synchronization over the measured channel itself. The receiver triggers the recording if a certain threshold is exceeded. This approach is simple but noise and interferences can erroneously trigger the recording and it is not possible to determine absolute delays.

For further information on the measurement methods, synchronization and detailed descriptions see Chap. 8 Channel Sounding in [38].

A.2 Correlative Channel Sounding using Maximum- Length Sequences

A M-Sequence (or Maximum- Length Sequence MLS) is a periodic binary pseudo random sequence. It has a length of $2^N - 1$, where N is a positive integer. Such a periodic sequence can be generated using a digital shift register containing N bits. The M-Sequence is often chosen ahead of other alternatives for the pseudo-random sequence in correlative channel sounding. It has a very suitable auto-correlation function which has a single peak and is flat outside that peak (see Fig. A.2). The peak has a height of $2^N - 1$ and outside the peak the ACF has a value of -1. This results in a peak to off peak (POP) ratio of 2^N.

A block diagram of the specific M-Sequence based measurement system used in this work is shown in Fig. A.3. A RF-clock drives the shift register which generates the M- Sequence. The M-Sequence is used as stimulus signal and is sent via the transmit antenna. The signal is affected by the environment and will be deformed according to the objects in this environment. The receiver captures the signal using a Track&Hold (T&H) circuit and transforms the analog signal into the digital domain using an ADC. Multiple received signals are averaged to increase the SNR and the average signal is then processed. The received signal is cross-correlated with the original sequence which results in the channel impulse response (CIR). Fig. A.4 shows in the

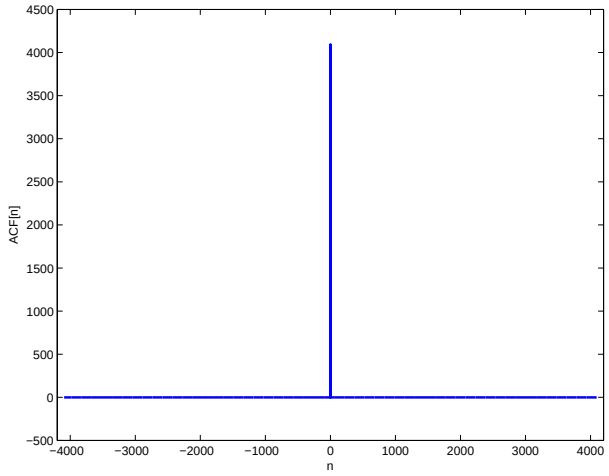

Figure A.2: Ideal Auto-correlation function of a 12 Bit M-Sequence

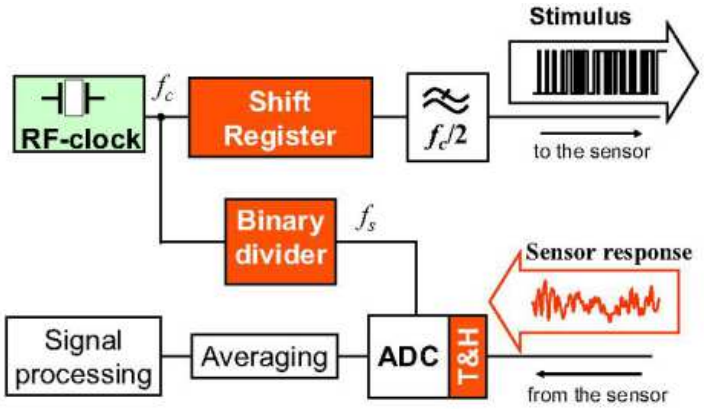

Figure A.3: Block diagram UWB M-Sequence device [39]

upper plot an ideal M-Sequence with $2^5 - 1 = 31$ chips, where N is the number of bits. The plot in the middle shows the delayed M-Sequence, affected by the environment and sampled at the receiver. The bottom plot shows the correlation of the received noisy signal with the originally sent M-Sequence. As it can be seen from this plot the delay equals 4 chips. It is easy to find the delay as there is a very high correlation gain of $2^N - 1$. A very precise and mathematical description of M-Sequences can be found in [40].

The clock frequency f_c determines the bandwidth of the signal. The stimulus will occupy a frequency spectrum from DC to $f_c/2$ if a suitable pseudorandom noise-code is chosen. In this frequency band the power is nearly constant and the energy will drop drastically beyond $f_c/2$.

As the signal takes a large bandwidth in the frequency domain, the pulse in the time domain is very short. It would therefore be necessary that the receiver electronics work at a very high sampling rate, but as the pseudorandom-noise is a periodic signal and therefore deterministic, sub-sampling for data capturing can be applied. This drastically reduces the sampling requirements for the receiver electronics. The timing of data capturing must be very exact as ultra-wideband signals change their amplitude rapidly. An example for sub-sampling can be seen in Fig. A.5 where capturing is distributed over two periods. In the figure, the first capturing period is shown. The sampling frequency is defined by the RF-clock and a binary divider.

As the M-Sequence is a cyclic code, the starting time (or delay) of the received signal is not determinable without any further information. One possibility to determine it, is to get the start sample of the M-Sequence generator from the transmitter. If this is not possible or

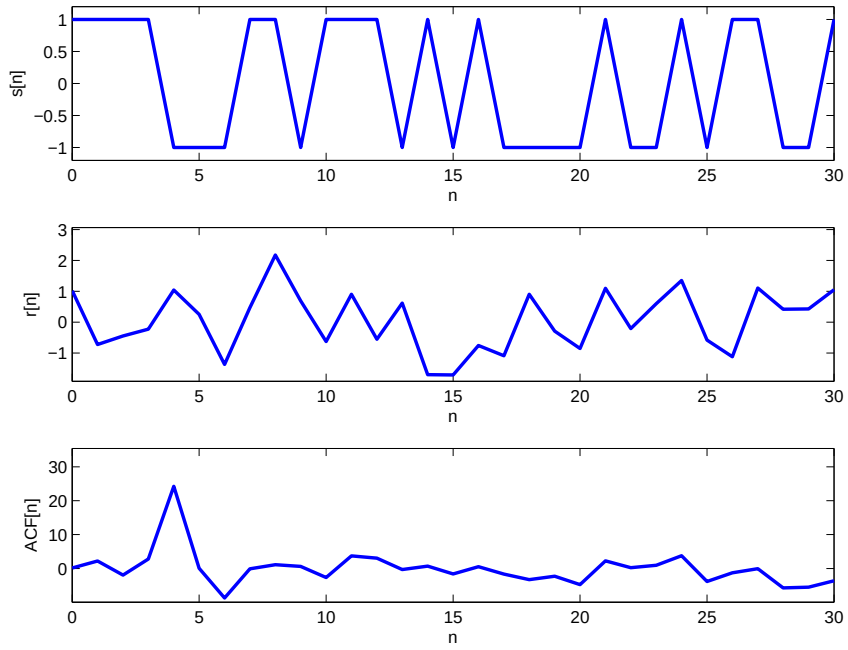

Figure A.4: Principle of M-Sequence, the binary pseudo random sequence $s[n]$ (upper plot), the received noisy and delayed signal $r[n]$ (middle plot) and the correlated signal $ACF[n]$ (lower plot) with the peak at a delay of 4

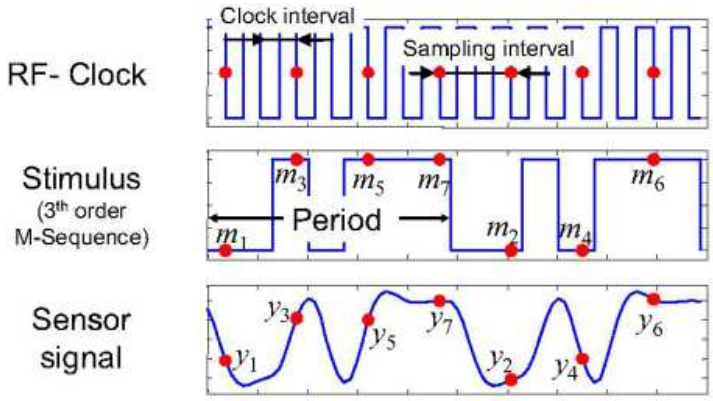

Figure A.5: Example of sub-sampling over two periods [39]

the transmitter does not allow that, some other mechanism is needed. In case of the used M-Sequence device (described in the next section), getting the start phase is not possible.

One way to determine the start of the received signal is to do a reference measurement at a known distance to determine the start of the impulse response. In this project the problem is solved by the device calibration as described in Section A.4.

A.3 ILMsens M-Sequence Device

The M-Sequence device is a sensor device manufactured by ILMsens (TU Ilmenau Service GmbH) which allows measuring the impulse response of UWB signals using a M-Sequence.

The M-Sequence device used in this project consists of two units, the RF electronics unit and the power supply unit (see Fig. A.6). The device includes a UWB signal generator for wideband

pseudorandom codes and two receivers which operate synchronously and support sub-sampling.

Figure A.6: RF electronics unit (left) and power supply unit (right) [41]

The device can be operated in baseband from 0.1 .. 3.2 GHz or in FCC passband from 3.8 .. 10.2 GHz using an I/Q up-down converter.

In order to use the device in baseband, connections are made directly to the connectors named Rx1, Rx2 and Tx, to use the FCC passband, SMA bridges must be installed according to Fig. A.7. The antennas are then connected via the RF1-In, RF2-In and RF-Out connectors.

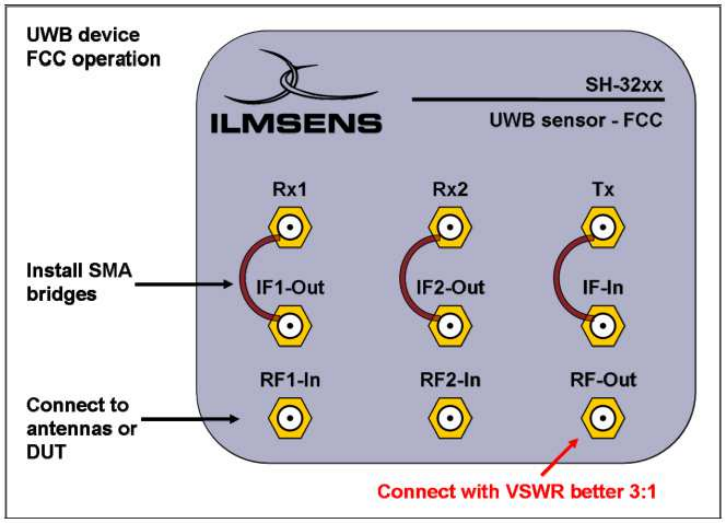

Figure A.7: Connectors of the M-Sequence device FCC configuration [41]

The device is connected to the computer via USB. For more details on the M-Sequence device see the hardware manual [41], information on the software can be obtained from the software manual [42].

A.4 Calibration

The block diagram in Fig. A.8 shows the influences of the channel sounder and the measurement setup. The internal crosstalk between the transmitter and the receivers is denoted as $H_{\text{cross},1}$

and $H_{\text{cross},2}$. The block $H_{\text{sys,TX}}$ models the part of the system response on the transmit side, $H_{\text{sys,RX1}}$ and $H_{\text{sys,RX2}}$ model the system response on the receiver sides one and two, respectively.

These responses have to be measured before the channel measurements. They are used to compute the actual channel impulse response.

The calibration is not only used to remove the system influences but it is also necessary to obtain a CIR with correct delay information. As described in Section A.2, the M-Sequence is a cyclic code and the code delay (delay of the received signal due to the cyclic code) is not determinable without any further information. One possibility to determine it is to get the start sample of the M-Sequence generator from the transmitter. If this is not possible or the transmitter does not allow that, some other mechanism is needed. In case of the used M-Sequence device, getting the start sample is not possible. Due to the calibration the code delay is canceled out and the correct delay information is in the received CIR. How this is done is shown in Section A.4.3.

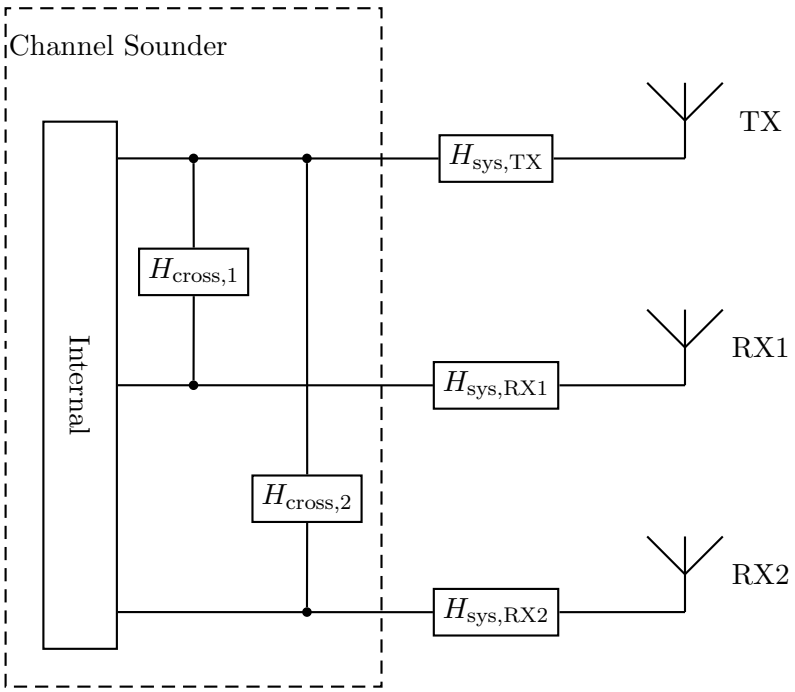

Figure A.8: Block diagram measurement influences

A.4.1 Measuring the Crosstalk

To measure the crosstalk, the transmitter cable is disconnected and a 50 Ω match is mounted on the transmit port. The receive antennas used for the actual measurements are connected to the respective receiver ports. This allows to measure only the influence on the receive ports inside the device as most of the transmit signal is attenuated and not received by the antennas. Fig. A.9 shows the setup of the crosstalk measurement.

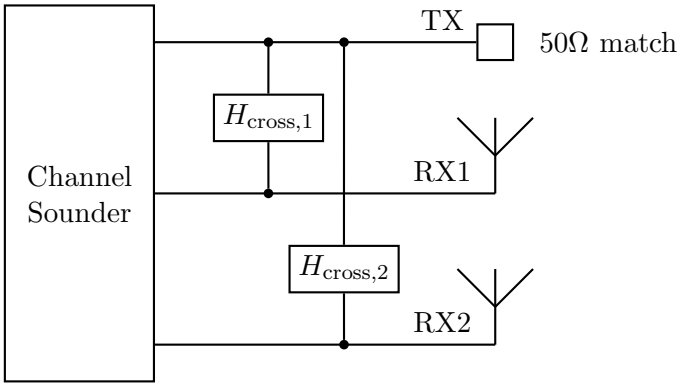

Figure A.9: Block diagram of the crosstalk measurement

A.4.2 Measuring the System Impulse Response

The system response has to be measured for each channel individually. To measure it, the cables of the transmitter and the receiver are disconnected from the antennas and the cables are connected directly using an appropriate connector.

As the measurement does not include the antennas, their additional delay has to be accounted for in the computations. Also, the used connector is considered part of the system response but is not used in the actual channel measurement. The block diagram of the system response measurement setup is shown in Fig. A.10.

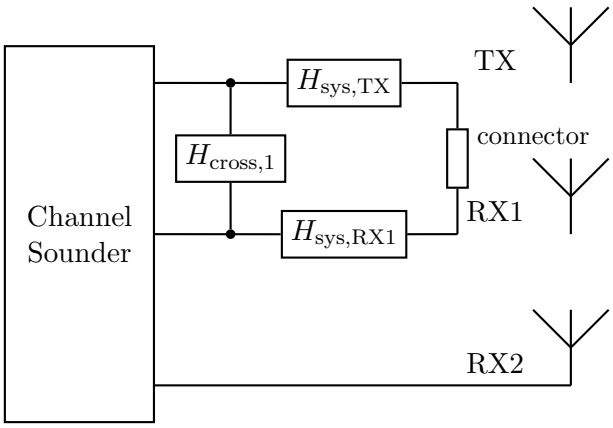

Figure A.10: Block diagram of the system response measurement of channel 1

A.4.3 Computing the Correct Impulse Response

Fig. A.11 shows the calibration process and how to obtain the actual channel impulse response (depicted as CIR). The channel sounder used in this project does not have the AGC gain & attenuation compensation functionality.

The CIR can be computed as follows (receive channel indices are dropped):

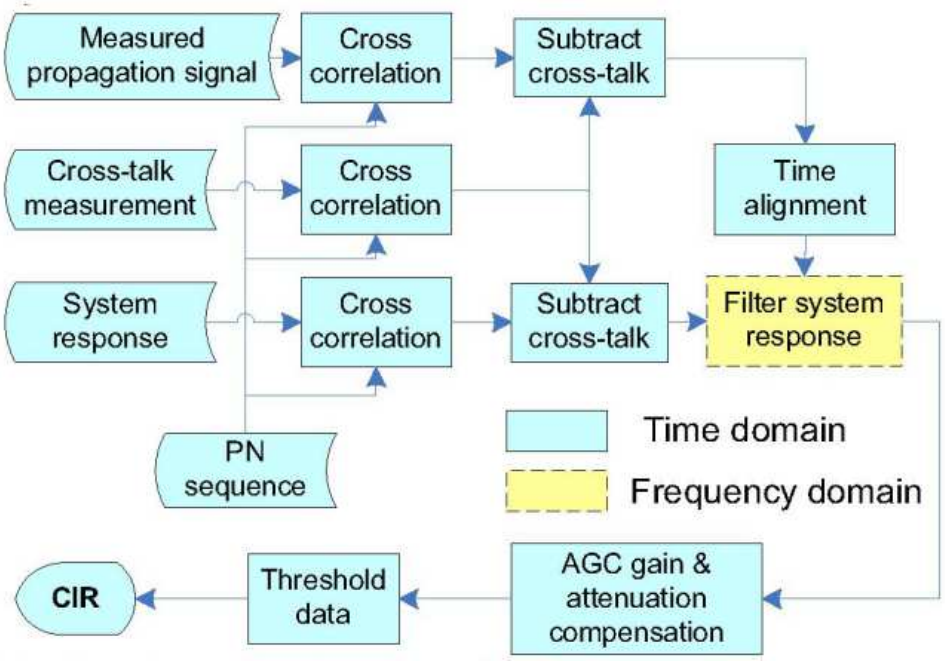

Figure A.11: Calibration block diagram [43]

- The system response measurement gives

$$H_{\mathrm{sys,meas}}(f) = H_{\mathrm{sys}}(f) \cdot 1 + H_{\mathrm{cross}}(f) \tag{A.9}$$

where the measured system response $H_{\mathrm{sys,meas}}$ consists of the actual system and the device internal crosstalk. The 1 depicts the channel for connected cables. The actual system response $H_{\mathrm{sys}} = H_{\mathrm{sys,TX}} \cdot H_{\mathrm{connector}} \cdot H_{\mathrm{sys,RX}}$ consists of the transmit part, the connector and receive part.

- Measuring the UWB channel using the measurement configuration results in:

$$H_{\mathrm{ch,meas}}(f) = H_{\mathrm{sys}}(f) \cdot H_{\mathrm{ch}}(f) + H_{\mathrm{cross}}(f) \tag{A.10}$$

where $H_{\mathrm{ch}}(f)$ is the actual channel impulse response.

- Inserting the system response $H_{\mathrm{sys}}(f)$ gives:

$$H_{\mathrm{ch,meas}}(f) = [H_{\mathrm{sys,meas}}(f) - H_{\mathrm{cross}}(f)] \cdot H_{\mathrm{ch}}(f) + H_{\mathrm{cross}}(f) \tag{A.11}$$

- To compute the actual channel, use:

$$H_{\mathrm{ch}}(f) = \frac{H_{\mathrm{ch,meas}} - H_{\mathrm{cross}}(f)}{H_{\mathrm{sys,meas}} - H_{\mathrm{cross}}(f)} \tag{A.12}$$

The division in frequency domain corresponds to a deconvolution in time domain. As the M-Sequence is a cyclic code and its generator does not necessarily start at the first sample, the

start of the impulse response usually is at some arbitrary delay, called code delay. In order to use the impulse response to get distance information the starting delay must be known. The M-Sequence device does not allow reading that start sample value of the generator from the register and also does not shift the measured impulse response automatically.

The system response and the measured channel impulse response both have this unknown shift due to the code delay. Due to the division, this delay cancels out and the only delay remaining in the result is caused by the antennas, which were not considered in the system response measurements, and the connector used in those measurements. This delay is denoted as τ_{add} in the CIR $h_{\text{ch}}(\tau + \tau_{\text{add}})$ in time domain and is obtained by

$$h_{\text{ch}}(\tau + \tau_{\text{add}}) = \text{IDFT}\left[H_{\text{ch}}(f)\right] \tag{A.13}$$

where IDFT[·] is the inverse Fourier Transform. The CIR still contains the antenna influences and the connector used during the system response measurements. To account for them, the CIR has to be shifted by an additional delay τ_{add}. The shift is done in the sample domain, so the antenna and the connector lengths have to be converted to number of samples and the additional delay in the sample domain is computed using

$$\tau_{\text{add,samples}} = \left\lfloor (len_{\text{tx}} + len_{\text{rx}} - len_{\text{conn}}) \cdot \frac{mClk}{c_{\text{prop}}} \right\rfloor \tag{A.14}$$

This assumes that antennas and connector have the same propagation speed c_{prop}. $mClk$ is the sampling frequency of the channel sounder and len_{tx}, len_{rx} and len_{conn} are the lengths of the transmit antenna, receive antenna and the connector, respectively. After this shift, the channel impulse response $h_{\text{ch}}(\tau)$ has the correct time delay and it is possible to use the delays starting at zero for distance measurements.

In Fig. A.12 a comparison between the raw measured CIR $r_h(\tau)$ and the calibrated CIR $h_{\text{ch}}(\tau)$ is shown. The raw measured CIR was aligned manually to the LOS component of the calibrated CIR to allow a comparison as it does not have the correct delay. In the raw CIR it can be seen that there is a smaller peak shortly after each signal component, e.g. after the line-of-sight peak at approximately 21 ns. This is because of the influence of the system response. Fig. A.13 shows an example of a measured system response. In the zoom of the main peak (lower plot) the second peak can be seen. The small peaks outside the main peak are due to the lack of an appropriate attenuator. Without the attenuator nonlinear distortions occur in the system and result in those peaks. The calibrated system response shows that the second peak is not present anymore.

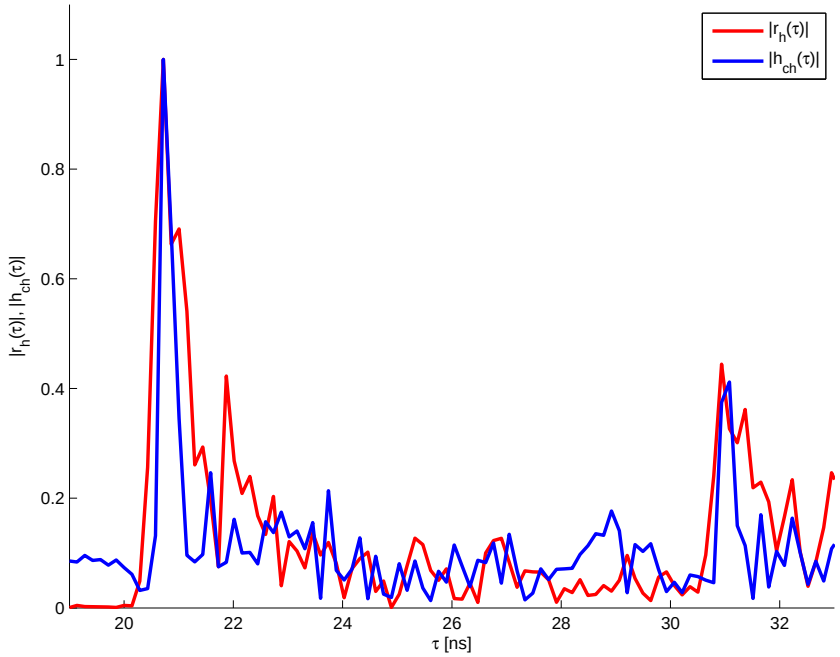

Figure A.12: Comparison of the raw measured CIR $r_h(\tau)$ and the calibrated CIR $h_{\mathrm{ch}}(\tau)$

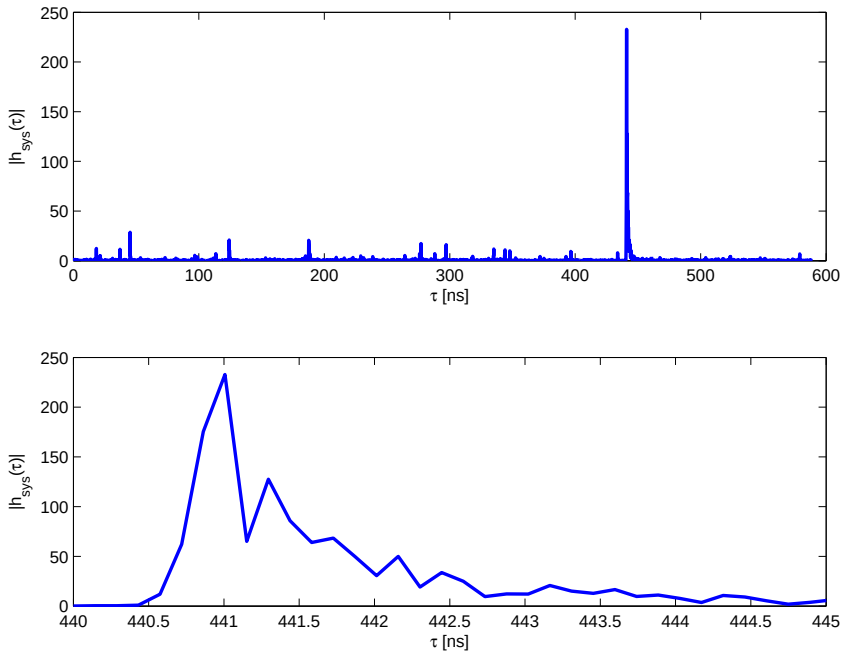

Figure A.13: Measured system response, the complete system response (upper plot) and a zoom to the main peak (lower plot)

A.5 Pulse Shaping

Pulse shaping is done to select a desired frequency range from the signal. The received signal is shaped using an appropriate pulse shape. The pulse shaping works in a manner similar to that described in [44] where a VNA was used for measuring the CIR. A difference is that the signal obtained using a VNA is in frequency domain whereas the M-Sequence device in this project delivers a time domain signal. The pulse shape and bandwidth are determined by TX and RX

filters and the selected frequency band.

For the pulse shaping, a suitable pulse form has to be defined first, here it is a raised cosine pulse. Typically, this is done in the frequency domain. The raised cosine pulse is defined by its center frequency f_c, the roll-off factor β_R and its bandwidth, which is typically defined as the inverse of the pulse duration T_p. This results in a 3-dB bandwidth $B_N = (1 + \beta_R)/T_p$. The calculated bandwidth B of the cosine pulse is then between f_{min} and f_{max} (Fig. A.14(a)):

$$f_{min} = f_c - \frac{\beta_R + 1}{2T_p} \tag{A.15}$$

$$f_{max} = f_c + \frac{\beta_R + 1}{2T_p} \tag{A.16}$$

The frequency domain signal is then transformed to time domain as described in [44]. To get the time domain raised cosine pulse $r(\tau)$, a transformation matrix $\boldsymbol{P}$ is multiplied with the frequency domain pulse in a vector, called $\mathbf{r}$, which consists of N_f frequency points.

$$r(\tau) = \boldsymbol{P}^T \boldsymbol{r} \tag{A.17}$$

The transformation matrix $\boldsymbol{P}$ holds the IDFT (inverse discrete Fourier transform) coefficients and is defined as

$$\boldsymbol{P} = \left[\mathrm{e}^{j2\pi f_0 \tau} \cdots \mathrm{e}^{j2\pi (f_0 + (N_f - 1)\Delta f)\tau} \right]^T \tag{A.18}$$

where Δf is the spacing of the frequency vector and f_0 is the lowest extracted frequency, i.e. $f_0 = f_c - (\beta_R + 1)/(2T_p)$. Alternatively, the raised cosine pulse could be defined directly in the

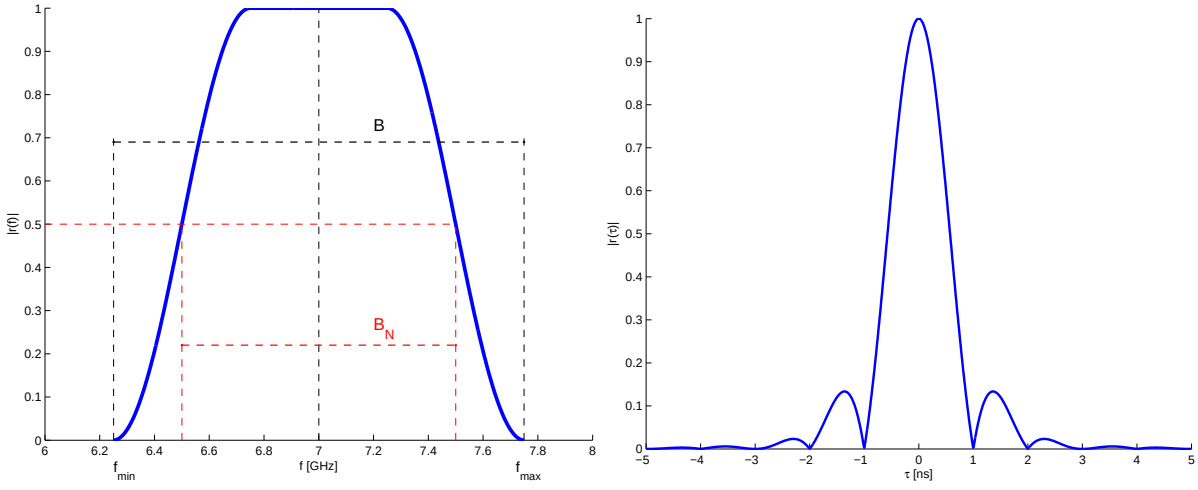

(a) Raised cosine in frequency domain

(b) Raised cosine in time domain

Figure A.14: Raised cosine in frequency and time domain with f_c =7 GHz, $\beta_R = 0.5$ and T_p =1 ns

time domain by

$$r(\tau) = \text{sinc}\left(\frac{\tau}{T}\right) \frac{\cos\frac{\pi\beta_R\tau}{T}}{1-\frac{4\beta_R^2\tau^2}{T^2}} \tag{A.19}$$

The raised cosine pulse $r(\tau)$ in time domain and the measured, calibrated impulse response $h_{\text{ch}}(\tau)$ are convolved to result in the shaped impulse response $h(\tau)$

$$h(\tau) = r(\tau)e^{+2\pi f_c\tau} * h_{\text{ch}}(\tau). \tag{A.20}$$

Fig. A.15 shows the originally measured, calibrated impulse response $h_{\text{ch}}(\tau)$ and the shaped impulse response $h(\tau)$.

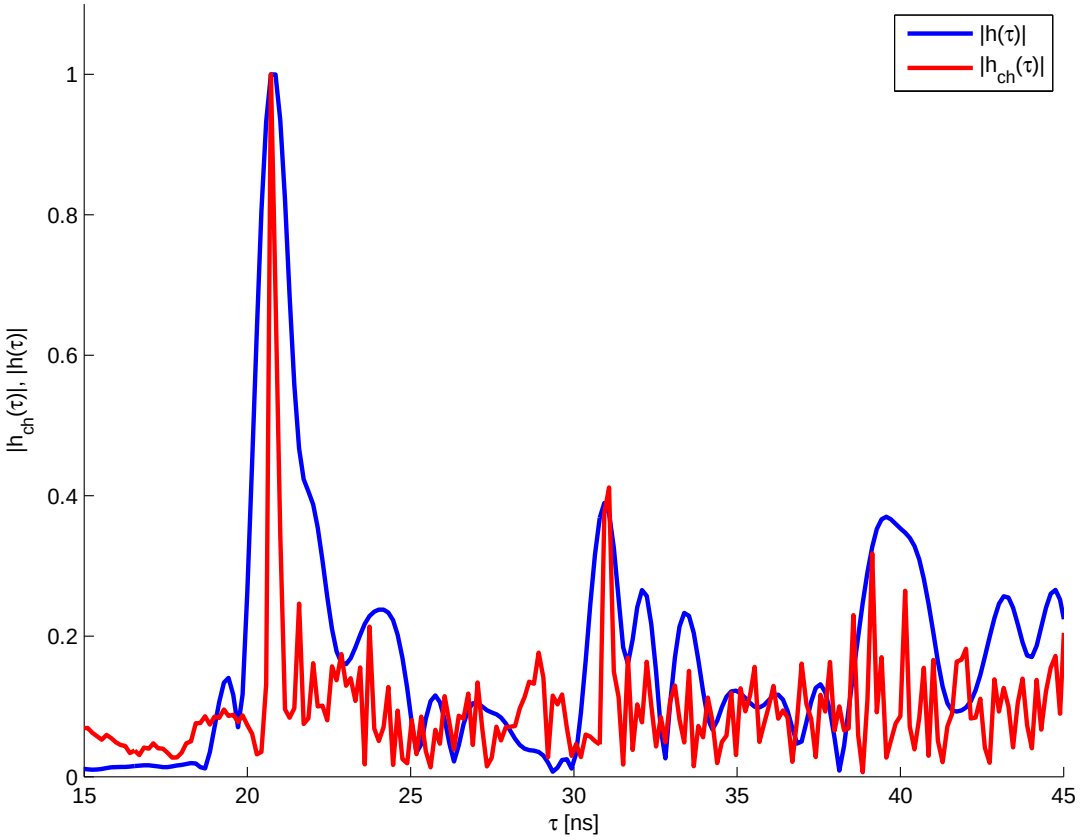

Figure A.15: Calibrated impulse response $h_{\text{ch}}(\tau)$ and shaped impulse response $h(\tau)$ in time domain. Pulse shaping parameters: $f_c = 7\,GHz$, $\beta_R = 0.5$ and $T_p = 1\,ns$

Bibliography

[1] D. Zhongliang, Y. Yanpei, Y. Xie, W. Neng, and Y. Lei, "Situation and development tendency of indoor positioning," *Communications, China*, vol. 10, no. 3, pp. 42–55, 2013.

[2] M. Jain, R. Rahul, and S. Tolety, "A study on indoor navigation techniques using smartphones," in *Advances in Computing, Communications and Informatics (ICACCI), 2013 International Conference on*, 2013, pp. 1113–1118.

[3] J. Choliz, A. Hernandez-Solana, and A. Valdovinos, "Evaluation of algorithms for uwb indoor tracking," in *Positioning Navigation and Communication (WPNC), 2011 8th Workshop on*, 2011, pp. 143–148.

[4] A. F. Molisch, "Ultra-wide-band propagation channels," *Proceedings of the IEEE*, vol. 97, no. 2, pp. 353 –371, 2 2009.

[5] R. Scholtz, R.-M. Cramer, and M. Win, "Evaluation of the propagation characteristics of ultra-wideband communication channels," in *Antennas and Propagation Society International Symposium, 1998. IEEE*, vol. 2, 1998, pp. 626–630 vol.2.

[6] P. Pagani and P. Pajusco, "Experimental analysis of the ultra wideband propagation channel over the 3.1 ghz - 10.6 ghz frequency band," in *Personal, Indoor and Mobile Radio Communications, 2006 IEEE 17th International Symposium on*, 2006, pp. 1–5.

[7] Z. Irahhauten, A. Yarovoy, G. Janssen, H. Nikookar, and L. Ligthart, "Ultra-wideband indoor propagation channel: Measurements, analysis and modeling," in *Antennas and Propagation, 2006. EuCAP 2006. First European Conference on*, 2006, pp. 1–6.

[8] R. Qiu, "A study of the ultra-wideband wireless propagation channel and optimum uwb receiver design," *Selected Areas in Communications, IEEE Journal on*, vol. 20, no. 9, pp. 1628–1637, 2002.

[9] M. Mahfouz, A. Fathy, M. Kuhn, and Y. Wang, "Recent trends and advances in uwb positioning," in *Wireless Sensing, Local Positioning, and RFID, 2009. IMWS 2009. IEEE MTT-S International Microwave Workshop on*, 2009, pp. 1–4.

[10] K. Witrisal and P. Meissner, "Performance bounds for multipath-assisted indoor navigation and tracking (mint)," in *Communications (ICC), 2012 IEEE International Conference on*, 2012, pp. 4321–4325.

[11] P. Meissner, T. Gigl, and K. Witrisal, "Uwb sequential monte carlo positioning using virtual anchors," in *Indoor Positioning and Indoor Navigation (IPIN), 2010 International Conference on*, 2010, pp. 1–10.

[12] P. Meissner and K. Witrisal, "Multipath-assisted single-anchor indoor localization in an office environment," in *Systems, Signals and Image Processing (IWSSIP), 2012 19th International Conference on*, 2012, pp. 22–25.

[13] H. Durrant-Whyte and T. Bailey, "Simultaneous localization and mapping: part i," *Robotics Automation Magazine, IEEE*, vol. 13, no. 2, pp. 99 –110, 6 2006.

[14] T. Bailey and H. Durrant-Whyte, "Simultaneous localization and mapping (slam): part ii," *Robotics Automation Magazine, IEEE*, vol. 13, no. 3, pp. 108–117, 2006.

[15] P. Newman, J. Leonard, J. Tardos, and J. Neira, "Explore and return: experimental validation of real-time concurrent mapping and localization," in *Robotics and Automation, 2002. Proceedings. ICRA '02. IEEE International Conference on*, vol. 2, 2002, pp. 1802–1809 vol.2.

[16] M. W. M. G. Dissanayake, P. Newman, S. Clark, H. Durrant-Whyte, and M. Csorba, "A solution to the simultaneous localization and map building (slam) problem," *Robotics and Automation, IEEE Transactions on*, vol. 17, no. 3, pp. 229–241, 2001.

[17] J. Salvi, Y. Petillot, S. Thomas, and J. Aulinas, "Visual slam for underwater vehicles using video velocity log and natural landmarks," in *OCEANS 2008*, 2008, pp. 1–6.

[18] T. Deisler, J. Thielecke, R. Salman, T. Schultze, and I. Willms, "Uwb radar object recognition for slam," in *Radar Symposium (IRS), 2010 11th International*, 2010, pp. 1–4.

[19] T. Deissler and J. Thielecke, "Uwb slam with rao-blackwellized monte carlo data association," in *Indoor Positioning and Indoor Navigation (IPIN), 2010 International Conference on*, 2010, pp. 1–5.

[20] A. Ahmad, S. Huang, J. Wang, and G. Dissanayake, "A new state vector for range-only slam," in *Control and Decision Conference (CCDC), 2011 Chinese*, 2011, pp. 3404–3409.

[21] ——, "A new state vector and a map joining algorithm for range-only slam," in *Control Automation Robotics Vision (ICARCV), 2012 12th International Conference on*, 2012, pp. 1024–1029.

[22] P. Newman and J. Leonard, "Pure range-only sub-sea slam," in *Robotics and Automation, 2003. Proceedings. ICRA '03. IEEE International Conference on*, vol. 2, 2003, pp. 1921–1926 vol.2.

[23] J.-L. Blanco, J. Fernandez-Madrigal, and J. Gonzalez, "Efficient probabilistic range-only slam," in *Intelligent Robots and Systems, 2008. IROS 2008. IEEE/RSJ International Conference on*, 2008, pp. 1017–1022.

[24] S. Gezici and H. Poor, "Position estimation via ultra-wide-band signals," *Proceedings of the IEEE*, vol. 97, no. 2, pp. 386–403, 2009.

[25] A. F. Molisch, "Ultrawideband propagation channels-theory, measurement, and modeling," *Vehicular Technology, IEEE Transactions on*, vol. 54, no. 5, pp. 1528 – 1545, 9 2005.

[26] P. Meissner, E. Leitinger, M. Froehle, and K. Witrisal, "Accurate and robust indoor localization systems using ultra-wideband signals," in *European Conference on Navigation (ENC)*, Vienna, 2013.

[27] T. Gigl, P. Meissner, J. Preishuber-Pfluegl, and K. Witrisal, "Ultra-wideband system-level simulator for positioning and tracking (u-spot)," in *Indoor Positioning and Indoor Navigation (IPIN), 2010 International Conference on*, 2010, pp. 1–9.

[28] P. Meissner, D. Arnitz, T. Gigl, and K. Witrisal, "Analysis of an indoor uwb channel for multipath-aided localization," in *Ultra-Wideband (ICUWB), 2011 IEEE International Conference on*, 2011, pp. 565–569.

[29] P. Meissner and K. Witrisal, "Analysis of position-related information in measured uwb indoor channels," in *Antennas and Propagation (EUCAP), 2012 6th European Conference on*, 2012, pp. 6–10.

[30] Y. Shen and M. Win, "Fundamental limits of wideband localization part i: A general framework," *Information Theory, IEEE Transactions on*, vol. 56, no. 10, pp. 4956–4980, 2010.

[31] P. Meissner, E. Leitinger, M. Lafer, and K. Witrisal, "A Real-Time Demonstration System for Multipath-Assisted Indoor Navigation nd Tracking (MINT)," in *IEEE ICC 2014 Workshop on Advances in Network Localization and Navigation (ANLN)*, 2014, submitted.

[32] J. Leonard and R. Rikoski, "Incorporation of delayed decision making into stochastic mapping," in *Experimental Robotics VII*, ser. Lecture Notes in Control and Information Sciences, D. Rus and S. Singh, Eds. Springer Berlin Heidelberg, 2001, vol. 271, pp. 533–542. [Online]. Available: http://dx.doi.org/10.1007/3-540-45118-8_53

[33] J. J. Leonard, R. J. Rikoski, P. M. Newman, and M. Bosse, "Mapping partially observable features from multiple uncertain vantage points," *International Journal of Robotics Research*, vol. 21, pp. 943–975, 2002.

[34] N. Sirola, "Closed-form algorithms in mobile positioning: Myths and misconceptions," in *Positioning Navigation and Communication (WPNC), 2010 7th Workshop on*, 2010, pp. 38–44.

[35] D. Simon, *Optimal State Estimation: Kalman, H Infinity, and Nonlinear Approaches*. Wiley-Interscience, 2006.

[36] G. H. Golub and V. Pereyra, "The differentiation of pseudoinverses and nonlinear least squares problems whose variables separate," *SIAM Journal on Numerical Analysis*, vol. 10, no. 2, pp. 413–432, Apr 1973.

[37] T. Jost, W. Wang, U. Fiebig, and F. Perez-Fontan, "Detection and tracking of mobile propagation channel paths," *Antennas and Propagation, IEEE Transactions on*, vol. 60, no. 10, pp. 4875–4883, 2012.

[38] A. F. Molisch, *Wireless Communications*, 2nd ed. John Wiley & Sons Ltd., 2011.

[39] J. Sachs, R. Herrmann, M. Kmec, M. Helbig, and K. Schilling, "Recent advances and applications of m-sequence based ultra-wideband sensors," in *Ultra-Wideband, 2007. ICUWB 2007. IEEE International Conference on*, 9 2007, pp. 50 –55.

[40] D. D. Rife and J. Vanderkooy, "Transfer-function measurement with maximum- length sequences," in *Journal Of The Audio Engineering Sociery Audio/Acoustics/Applications*, vol. 37, no. 6, 6 1989, pp. 419–444.

[41] TU Ilmenau Service GmbH, *Hardware Manual - Ultra Wideband M-Sequence Device*, 8 2012.

[42] ——, *Manual MatLab Software for Ultra Wideband M-Sequence Devices*, 8 2012.

[43] R. Cepeda, S. C. J. Parker, and M. Beach, "The measurement of frequency dependent path loss in residential los environments using time domain uwb channel sounding," in *Ultra-Wideband, 2007. ICUWB 2007. IEEE International Conference on*, 2007, pp. 328–333.

[44] P. Meissner, *UWB Channel Measurement Campaigns*, 9 2012. [Online]. Available: www.spsc.tugraz.at/tools/UWBmeasurements